2001

Atomic and Electronic Structure of Ultra-Thin Metal Epitaxy on Metal and Semiconductor Surfaces.

Dustin Alexander Hite
Louisiana State University and Agricultural & Mechanical College

INFORMATION TO USERS

This manuscript has been reproduced from the microfilm master. UMI films the text directly from the original or copy submitted. Thus, some thesis and dissertation copies are in typewriter face, while others may be from any type of computer printer.

The quality of this reproduction is dependent upon the quality of the copy submitted. Broken or indistinct print, colored or poor quality illustrations and photographs, print bleedthrough, substandard margins, and improper alignment can adversely affect reproduction.

In the unlikely event that the author did not send UMI a complete manuscript and there are missing pages, these will be noted. Also, if unauthorized copyright material had to be removed, a note will indicate the deletion.

Oversize materials (e.g., maps, drawings, charts) are reproduced by sectioning the original, beginning at the upper left-hand corner and continuing from left to right in equal sections with small overlaps.

Photographs included in the original manuscript have been reproduced xerographically in this copy. Higher quality 6" x 9" black and white photographic prints are available for any photographs or illustrations appearing in this copy for an additional charge. Contact UMI directly to order.

ProQuest Information and Learning
300 North Zeeb Road, Ann Arbor, MI 48106-1346 USA
800-521-0600

ATOMIC AND ELECTRONIC STRUCTURE OF ULTRA-THIN METAL EPITAXY ON METAL AND SEMICONDUCTOR SURFACES

A Dissertation
Submitted to the Graduate Faculty of the
Louisiana State University and
Agricultural and Mechanical College
in partial fulfillment of the requirements for
the degree of
Doctor of Philosophy
in
The Department of Physics and Astronomy

by
Dustin Hite
B.S., Louisiana State University, 1993
M.S., Louisiana State University, 2000
August 2001

Acknowledgements

There are many people to whom I am wholeheartedly indebted regarding this work. From day one, I have been pursuing a goal that could not have been possible to achieve if it was not for the help of others.

First and foremost, I would like to acknowledge the support of my research advisor, Dr. Phillip Sprunger. Not only did he teach me virtually everything there is to know about experimental surface science, but he also taught me to have the courage required to move ahead into the unknown realms of the laboratory. If it was not for his support in presenting papers at conferences and meetings, I would not have been able to succeed as I have.

I need to acknowledge the entire staff of CAMD, both past and present. They have supported me in many ways, administratively and technically. The faculty and staff of the Physics Department cannot go without recognition either, in particular the staff of the Physics Machine Shop.

I would like to thank David Zehner, John Wendelken, and Gary Ownby of Oak Ridge National Laboratory for providing their top-notch lab to a pair of inexperienced graduate students from Louisiana. The knowledge and expertise of Erik Lægsgaard from the University of Aarhus proved to be invaluable despite the fact that we have never actually met in person.

I wish to acknowledge the help and hard work of my closest collaborators. Useful discussions with the following people have proved to be indispensable. They are Orhan Kizilkaya, Rich Kurtz, Jaewu Choi, Shu-Jung Tang, Kevin Koch, Carl Ventrice, Heike Geisler, and W. and E. L. D. Hebenstreit.

There are two additional people that I would like to acknowledge, because without there love and unlimited support, I could not have done this work. To my wife, Bel, and my daughter, Juniper, thank you.

Table of Contents

List of Tables

List of Figures

Abstract

The fundamental study of heteroepitaxy has proved to have profound influences on technological applications of thin films, particularly due to the reduced dimensionality and quantum mechanical effects found in these unique nanostructured systems. In this study, particular attention is given to the correlations between atomic-scale morphology and the consequential electronic structure of heteroepitaxial systems that exhibit deviations from traditional growth modes in the initial stages of growth. Surface-confined systems are especially interesting because they exhibit properties that are fundamentally different from the bulk and often have no bulk analogs existing in nature.

The surface-sensitive techniques of variable-temperature scanning tunneling microscopy and synchrotron-based angle-resolved photoelectron spectroscopy have been used to investigate the atomic and electronic structures of Ag/Cu(110), Ag/Ni(110), Ni/Ag(100) and Be/Si(111)-(7 × 7). Particular attention is given to the initial stages of growth (submonolayer coverages), where each metal on metal system exhibits a bulk-immiscible, surface-confined alloy formation and Be/Si(111) undergoes reactive epitaxy.

The metal on metal systems studied in this work exhibit a trend in *sp-d* electronic hybridization due to the negligible *d*-band overlap between the adatoms and the substrate and their increased coordination through surface alloy formation (Ag/Cu(110) and Ag/Ni(110)) and subsurface clustered growth (Ni/Ag(100)). As a result, each system displays quasi-three-dimensional electronic structures.

Beryllium deposition on the (7 × 7) reconstructed surface of Si(111) results in an amorphous clustered silicide compound at temperatures as low as 120 K. High temperature annealing of the Be/Si(111) surface results in a universal ring cluster structure commonly seen in epitaxial transition metal silicide surfaces. Because it has been previously determined that ring clusters occur only for systems with a metal-silicon bond length less than 2.5 Å, it is thus concluded that the Be-Si bond length is less than 2.5 Å, a value consistent with theoretical predictions.

Chapter One

Introduction

Metal films grown on metal and semiconductor substrates have been studied for decades mainly due to a wide variety of resulting technological applications, including semiconductor heterostructure devices, magnetic spin valves, and heterogeneous catalysis. In order to fully take advantage of the applicability and full functionality of these heteroepitaxial systems, a fundamental understanding of the atomic-scale processes and resultant electronic structures is warranted. In particular, as structures and devices are fabricated with ever-decreasing scales, quantum mechanical effects play an ever-increasing role. In fact, many of these widely used technological applications of thin films remain poorly understood on a fundamental level. Motivated by the desire to understand these heteroepitaxial systems on a fundamental level, the investigations detailed in this work are aimed at correlating the surface morphology and resultant electronic structure of a unique class of heteroepitaxial systems in the initial stages of growth. Particularly, the focus is on systems that deviate from the traditional growth modes of epitaxy, exhibiting surface

confined alloy formation (Ag/Cu(110), Ag/Ni(110)), subsurface growth (Ni/Ag(100)) and reactive epitaxy (Be/Si(111)).

Investigations of heteroepitaxy are often hindered by difficulties in distinguishing the competing influences between the thermodynamics of the formation of a new solid phase and the kinetics involved in growth. As thermodynamics tend to drive the system to a minimum free energy configuration, kinetic limitations can dominate and therefore dictate the resultant growth morphology. Such kinetic effects are processes that depend on temperature and time, for example, flux rates, surface diffusivity, and condensation and evaporation from step boundaries.

Traditionally, epitaxial growth has been characterized by the three growth modes based on simple thermodynamic equilibrium arguments. Bauer suggested that the quantity that determines a given growth mode is dictated by Young's equation [1,2],

$$\Delta\gamma = \gamma_a + \gamma_i - \gamma_s. \qquad \text{(Eq. 1)}$$

Here, γ_a and γ_s are the surface free energies of the adlayer and substrate, respectively, whereas γ_i is the interfacial free energy, an unknown and often neglected quantity that has substantial impact on resultant growth morphologies. Depending on the relative values of the interfacial and surface free energies, these growth modes are divided into three categories, historically named after their original investigators:

1) Layer-by-layer or Frank van der Merwe (FM) growth [3]. In this case, the adlayer favors wetting the substrate, and one overlayer is fully completed before the next layer starts to form, i.e. the condition $\Delta\gamma \leq 0$ is fulfilled for every successive adlayer. This strict two-dimensional growth mode is generally only possible for homoepitaxial growth where $\Delta\gamma = 0$.

2) Three-dimensional or Volmer Weber (VM) growth $(\Delta\gamma > 0)$ [4]. In this case, the metal adlayer does not favor wetting the substrate, and small three-dimensional clusters will nucleate. Subsequently, a rough three dimensional island growth mode will result.

3) Layer-by-layer growth followed by island formation or Stranski Krastranov (KS) growth [5] ($\Delta\gamma < 0$ for n adlayers). This mode is an intermediate between FM and VW growth. The adlayer wets the substrate in the beginning, but as the interface energy increases with increasing layer thickness, a transition from layer-by-layer to island growth is observed at a critical layer thickness *n*.

These descriptions are valid only in the limit that thermodynamic equilibrium is established. When heteroepitaxy proceeds under conditions far from equilibrium, deviations from these aforementioned growth modes exist.

In addition to deviations from the traditional growth modes resulting from kinetic influences, other growth modes can occur under conditions of thermodynamic equilibrium in the initial stages of heteroepitaxial growth. As expected for bulk miscible combinations of adatoms and substrates, intermixing at the surface and into the bulk may occur. Moreover, it has become apparent recently

that the intermixing, or surface alloying, of bulk-immiscible systems is much more important than previously believed. Bulk immiscible systems are characterized by a large and positive enthalpy of mixing, a macroscopic quantity typically driven by excess strain energies resulting from large lattice mismatch [6]. For these systems it is often the case, in the initial stages of growth, that substitutional alloy formation is a substantially lower energy configuration than that forming a highly strained pseudomorphic overlayer. These bulk-immiscible surface alloys are exclusively confined to the outer most surface layer, thus giving rise to two-dimensional alloy phases for which there is no three-dimensional analog. As a result, new and technologically advantageous properties emerge, e.g. enhancement of catalytic reactivity and selectivity [7].

Two of the metal-on-metal systems investigated in this study, namely Ag/Cu(110) and Ag/Ni(110), exhibit bulk-immiscible surface-confined alloy formation. The alloy formation is an activated substitutional process that occurs at the surface due to the characteristic undercoordination of the atoms at the surface. In the initial stages of growth, atomic exchange of adatoms with substrate atoms in the surface layer results in a lower energy configuration than overlayer formation, provided that the activation barrier of exchange energy is overcome (Fig. 1). Often it is the case that room temperature provides enough thermal energy to overcome this activation, particularly on the open (110) face of the face-centered cubic (fcc) crystals of Cu and Ni. As the coordination number is increased from 7 for the (110) surface, to 8 for the (100), and 9 for the (111), this activation energy is likewise increased [8]. This exchange process results in a locally compressive strain due to atomic size mismatch, which can be accommodated by a local relaxation of the

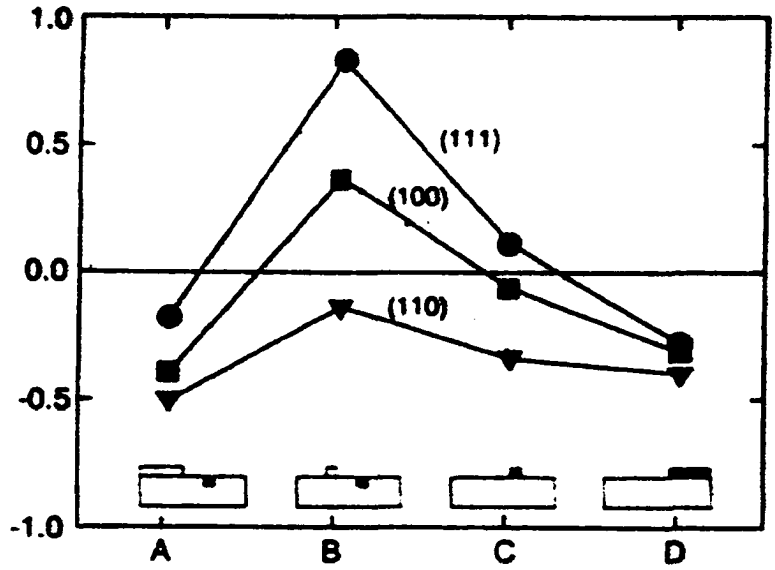

Figure 1. Different energies for a Ag atom on a Ni surface. From right to left, are depicted Ag atoms in a large Ag island, an isolated Ag adatom, a Ni adatom and a Ag atom alloyed into the first Ni layer, and finally a Ag atom in the Ni layer and Ni atoms in a large Ni island. (from Ref. [8]).

surface atoms, a characteristic attribute of the under-coordinated nature of the surface. As a result, expelled substrate atoms diffuse on the surface promoting step edge growth or terrace nucleated islands.

A well-accepted definition of coverage is the ratio of surface density of adatoms to the surface density of substrate atoms. As an example, a coverage of 0.5 monolayers (ML) of Ag, pseudomorphically alloyed into the Ni(110) surface, implies a 50% concentration of Ag atoms in the Ni surface layer. As a trend in surface alloys, when the coverage increases and alloy formation proceeds, compressive strain energies increase to the point where the substitutional alloy is no longer energetically favored. At this point de-alloying occurs forming various unique morphologies. Typically when the adlayer coverage approaches 1 ML, a two-dimensional close packed overlayer results. For the example of Ag/Ni(110), this hexagonal overlayer corresponds to a coverage of 1.2 ML, where the Ag hexagonal structure is more dense than the rectangular Ni(110) surface net. In this treatment of the atomic and electronic structures in heteroepitaxy, consideration is restricted to coverages in the initial phases of growth. Therefore, structures resulting from coverages greater that 1 ML are beyond the scope of this work.

The complementary system of Ni/Ag(100) was also studied. At room temperature Ni deposition leads to a Volmer-Weber growth mode. This is a nice example of how Young's equation predicts the resultant growth mode. Since the surface free energy of Ni (γ_{Ni} = 1.9 J/m^2) is greater than that of Ag (γ_{Ag} = 1.3 J/m^2), $\Delta\gamma$ is assured to be positive. However, as this system is annealed to temperatures as low as 420 K, the nano-clusters of Ni "sink" down into the substrate and are

subsequently capped by at least one layer of Ag (Fig. 2). This novel surfactant-like morphology has been observed in other metal-on-metal systems (Rh/Ag [9], Cu/Pb [10], Ni/Cu [11]), and has been studied extensively for the Ni/Ag(100) system using theoretical methods [12-16]. In this case, the resultant subsurface morphology is a consequence of the high kinetic mobility of Ag atoms at the surface, but, more importantly, the minimization of the total energy through the formation of a thermodynamically stable morphology occurs. This surface enrichment of substrate atoms leads to a greater interfacial coordination, which serves to lower the total energy of the system [15].

Finally, the last of the unusual growth mechanisms to be described in this work is one in which a chemical reaction occurs between the substrate and the impinging atoms, known as reactive epitaxy. Reactive epitaxy is often employed in the formation of transition metal silicides, whereby metal atoms are deposited onto a silicon substrate while the substrate is held at elevated temperatures. Here, the deposition of Be on Si(111) – (7 × 7) was investigated, which results in the formation of a surface confined silicide occurring at temperatures as low as 120 K. This system is particularly intriguing, in addition to the low temperature solid phase chemical reaction, because the formation of beryllium silicide has never before been realized experimentally neither in the bulk nor at the surface.

In this dissertation, the main focus is on correlating the atomic structure with the resultant electronic structure of various unique heteroepitaxial systems such as those described above. The main tool used to investigate the morphological structures is scanning tunneling microscopy (STM), while the electronic structures have been characterized using synchrotron-based, angle-resolved photoemission

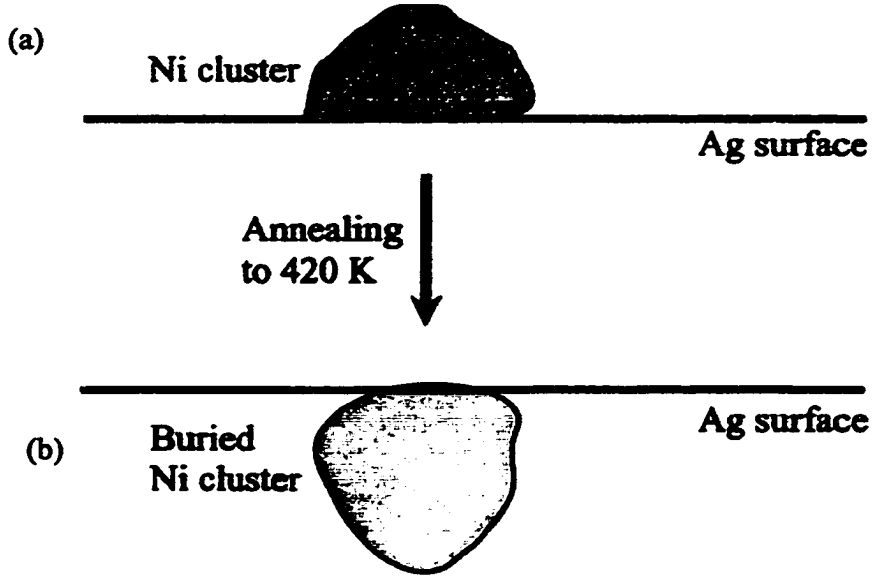

Figure 2. Schematic depiction of the "sinking" Ni nanoclusters. (a) Volmer Weber growth mode results from deposition of Ni on Ag(100) at room temperature. (b) Annealing the Ni/Ag(100) system to 420 K leads to a subsurface "surfactant-like" growth morphology.

spectroscopy (SR-ARPES). Using these two extremely powerful techniques, a wealth of information has been assimilated regarding the highly hybridized metallic bonding and electronic dimensionality associated with the increased coordination in surface alloy formation. It is the hope of the author that this work helps to further understand the complex nature of ultra-thin metal epitaxy on metal and semiconductor surfaces.

Chapter Two

Experimental Methods

2.1 Scanning Tunneling Microscopy (STM)

The principle and operation of the STM is conceptually rather simple. A sharp metal tip, usually made from W or Pt/Ir wire, is brought to within such close proximity to the sample surface that an overlap occurs between the wave functions of the tip and atoms at the surface (Fig. 3). With a bias applied between the tip and the sample, electrons can tunnel across the junction from the tip to the sample or vice versa, depending on the polarity of the bias, V_t. This gives rise to a measurable tunnel current, I_t, typically on the order of 1 – 10 nA. Because the tunnel current depends exponentially on the distance between the tip and the surface, individual atoms in the surface give rise to current variations as the tip is raster scanned across the surface. This scanning of the tip is facilitated by the use of piezoelectric transducers, which allow for manipulation of the tip on a sub-nanometer scale. By convention, x and y coordinates are considered to be in the plane of the surface, where z is a measure of the perpendicular distance between the surface and the tip.

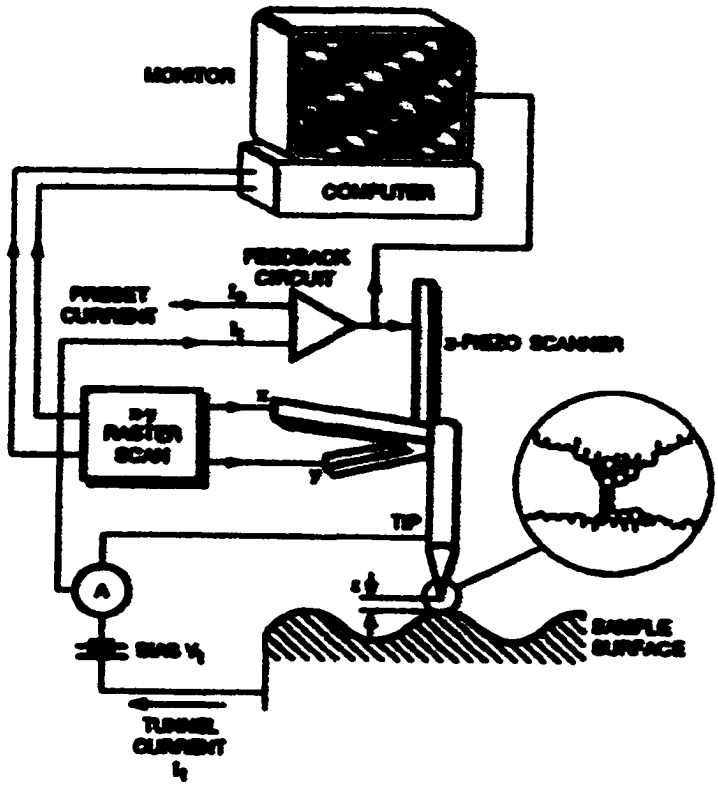

Figure 3. Schematic illustration of the basic principles and operation of the STM. The tip can be moved in three orthogonal dimensions. The *z*-transducer varies the tip-surface distance while the *x,y* transducers raster scan the tip laterally across the surface (from Ref. [18]).

Normally, the STM is operated in constant-current mode whereby the tunnel current is compared to a preset value by the use of feedback circuitry. The difference between the preset current and the actual current allows for a correction voltage to be applied to the *z*-transducer, causing the distance between the tip and sample to vary when a protrusion or depression is traversed. Recording the *z*-voltage as a function of the tip's lateral position during raster scanning provides a map of the surface topography.

Various STM theories have been developed, however due to formidable complexities in characterizing the possible wavefunctions associated with the tip, and strong interactions between the tip and the sample, the theoretical effort in STM has been relatively rare. Most of the tunneling theories are based on the "perturbative-transfer Hamiltonian", a formalism introduced by Bardeen in 1961 [17]. First, it is assumed that the interaction between the tip and sample is sufficiently weak so that it may be neglected. Second the tunnel current can be obtained from the wavefunctions of the separate tip and sample potentials. The tunnel current is then calculated from the overlap of the respective tip and sample wavefunctions, Ψ_μ and Ψ_ν, in the region of the tunnel barrier, and results in the following:

$$I_t = \frac{2\pi e}{\hbar}\sum_{\nu,\mu} f(E_\nu)\left[1 - f(E_\nu + eV_t)\right]\left|M_{\mu,\nu}\right|^2 \delta(E_\mu - E_\nu), \qquad \text{(Eq. 2)}$$

where the tunneling matrix element is given by:

$$M_{\mu\nu} = \frac{\hbar^2}{2m} \int_{S_0} d\bar{S} \cdot \left(\Psi_\mu^* \nabla \Psi_\nu - \Psi_\nu^* \nabla \Psi_\mu \right). \qquad \text{(Eq. 3)}$$

Here, the integral is over any surface S_0 that lies entirely within the barrier region, and E_μ, E_ν are the eigenenergies of the tip and sample, respectively. The delta function implies elastic tunneling and the Fermi-Dirac function, $f(E)$, reflects the fact that tunneling must occur from a filled state into an empty state [18].

In the Tersoff-Hamann formalism, the transfer Hamiltonian approach is applied with the following approximations: the tunnel voltage is considered to be small, and the tip is assumed to be spherical so that spherically symmetric *s*-wave functions only need to be considered [19]. Under these assumptions, the following expression for the tunneling conductance is obtained:

$$G_t \equiv \frac{I_t}{V_t} \cong 0.1 R^2 e^{2\kappa R} \rho_s(r_t, E_F), \qquad \text{(Eq. 4)}$$

$$\rho_s(r_t, E_F) \equiv \sum_\nu |\Psi_\nu(r_t)|^2 \delta(E_\nu - E_F), \qquad \text{(Eq. 5)}$$

where $\rho_s(r_t, E_F)$ is the local density of states of the sample surface at the Fermi level evaluated at the center position of the tip, r_t. R is the radius of curvature of the spherical tip, $\kappa = \hbar^{-1}(2m\phi)^{1/2}$ is the decay length for the wavefunction in vacuum and ϕ is the tunnel barrier height relative to the Fermi level. Although this result

reflects only the LDOS of the surface and not the combined tip-sample system, it is possible to get simple approximate estimates of dimensions. With $|\Psi_v(r_t)|^2 \propto e^{-2\kappa z(R+z)}$, we have

$$G_t = \frac{I_t}{V_t} \propto e^{-2\kappa z} = \exp\left(-1.025\sqrt{\phi}z\right), \quad (\phi \text{ in eV}, z \text{ in Å}), \quad \text{(Eq. 6)}$$

where it is seen that the tunnel conductance consequently decays with increasing distance, z. For typical values of ϕ, a change of z by 1 Å will result in variations of a factor of ten in I_t. As a result, the apex of the tip dominates in the signal, which makes atomic resolution achievable.

2.2 Angle-Resolved Photoelectron Spectroscopy (ARPES)

2.2.1 Theory

Photoemission spectroscopy provides a great wealth of information about the electronic band structure of a given sample. The independent experimental parameters are numerous and the measured energy distribution curves often change drastically as a result of variations in these parameters. These include photon energy and polarization, incidence angle, crystal face and surface structure, emission angle and spin polarization of the photoelectrons. Essentially, the electronic bands of a crystal can be examined throughout the Brillouin zone using this technique.

Although photoemission spectroscopy is a widely used experimental tool, the theoretical formalism is far from complete. This is due to the fact that the photoemission process involves a many-body problem requiring a quantum

mechanical description. Despite this formidable situation, a surprisingly successful three-step model is often used to interpret photoemission spectra, and is outlined below.

The three-step model, developed originally by Berghund and Spicer [20], involves three independent steps in the following sequence: (1) the optical excitation of the electron from its initial state in the crystal, (2) the transport of that electron to the surface, and (3) the emission of the electron through the surface into the vacuum (Fig. 4). In step one, the optical excitation involves an interband transition between states of the same wave vector *k*. The internal energy distribution of photoexcited electrons is then given by

$$N_{int}(E,\hbar\omega) \propto \sum_{f,i} d^3\vec{k} \left|M_{fi}\right|^2 \delta\left(E_f(\vec{k}) - E_i(\vec{k}) - \hbar\omega\right)\delta\left(E - E_f(\vec{k})\right), \quad \text{(Eq. 7)}$$

where E is the final energy of the electron, $\hbar\omega$ is the photon energy, and $E_f(\vec{k})$ and $E_i(\vec{k})$ denote the energies of the final band state $|f,\vec{k}\rangle$ and the initial band state $|i,\vec{k}\rangle$, respectively. $|M_{fi}|^2$ is the square of the matrix element of the interaction Hamiltonian, $H^{int} \propto (\vec{A}\cdot\vec{p} + \vec{p}\cdot\vec{A})$, where $\vec{A}$ is the vector potential of the exciting electromagnetic field. The first delta function insures energy and momentum (*k*) conservation, while the second delta function specifies transitions to a given final state in the band structure.

In the second step, scattering dominated by the electron-electron interaction tends to reduce the number of unscattered photoexcited electrons reaching the

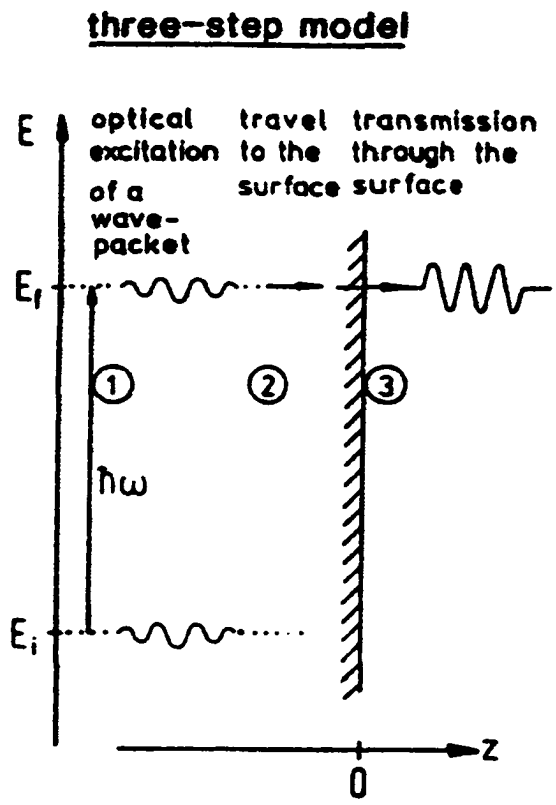

Figure 4. Schematic depiction of the three-step model for the photoemission process. Step one is an optical excitation from an initial state to a final state in the band structure. Step two addresses the transport of the electron to the surface, and step three is emission of the electron through the surface and into the vacuum (from Ref. [21]).

surface. For this reason, photoemission spectroscopy is truly a surface-sensitive experimental tool. For typical energies involved, the mean free path for inelastic scattering is on the order of 10-20 Å, allowing for surface emission to be comparable to that of emission from the bulk.

In step three, escape into the vacuum, electrons, whose component of kinetic energy normal to the surface is sufficient to overcome the surface potential barrier, proceed into the vacuum, whereas others are totally reflected back into the crystal. For the case of free electrons in a potential well of depth $E_{vac} - E_0$, electrons escaping to the vacuum must have

$$\left(\frac{\hbar^2}{2m}\right)\bar{K}_{\perp}^2 \geq E_{vac} - E_0, \qquad \text{(Eq. 8)}$$

where $\bar{K}_{\perp}$ is the component of the wave vector of the excited electrons perpendicular to the surface. Due to the translational invariance of the crystal potential parallel to the surface, $\bar{K}_{\parallel}$ is a conserved quantity, implying

$$\bar{p}_{\parallel} = \bar{K}_{\parallel} = \bar{k}_{\parallel} + \bar{G}_{\parallel}, \qquad \text{(Eq. 9)}$$

where $\bar{p}$ is the wave vector of the photoelectron in vacuum, $\bar{k}_{\parallel}$ is the parallel component of the reduced wave vector $\bar{k}$, and $\bar{G}_{\parallel}$ is the parallel component of any

reciprocal lattice vector $\bar{G}$. Finally the photoemitted electron emerges from the crystal characterized with a kinetic energy of

$$E_{kin} = \left(\frac{\hbar^2}{2m}\right)\left(\bar{p}_{\perp}^2 + \bar{K}_{\parallel}^2\right). \qquad \text{(Eq. 10)}$$

Based on the three-step model, the final expression for an angle-resolved photoelectron energy spectrum at a photon energy $\hbar\omega$ is given by

$$N\left(E, K_{\parallel}, \hbar\omega\right) \propto \sum_{fi} \int^{d^3k} \left|M_{fi}\right| D\left(E_f, \bar{k}\right) T\left(E_f, K_{\parallel}\right) \qquad \text{(Eq. 11)}$$
$$\times \delta\left(E_f\left(\bar{k}\right) - E_i\left(\bar{k}\right) - \hbar\omega\right) \delta\left(E - E_f\left(\bar{k}\right)\right) \delta\left(k_{\parallel} + G_{\parallel} - K_{\parallel}\right),$$

where $D\left(E_f, \bar{k}\right)$ is a coefficient detailing step two, transport to the surface, and $T\left(E_f, K_{\parallel}\right)$ is the transmission factor treating coherent emission of electrons with the same value of $k_{\parallel} + G_{\parallel}$ [21].

Other theoretical treatments have been developed, however it is believed that the three step model provides a reasonable description of the photoemission process. Needless to say, simplifications are also employed, one of which being the free electron final state approximation. Although seemingly unrealistic, the free electron final state approximation actually gives reasonable and simple estimations to describe the crystal band structures under certain conditions.

2.2.2 Dipole Selection Rules for Optical Direct Transitions

Since the bands in the solid and the electric dipole operator have definite symmetry, dipole selection rules must be taken into consideration, particularly when polarized radiation is used. The selection rules can be used to determine the symmetry of states involved in direct transitions in the photoemission process and often make the task of interpretating spectra easier by reducing the number of possible transitions. Non-relativistic dipole selection rules have been published for direct transitions in the fcc crystal structure for the special cases of normal emission [22] and for emission in the mirror planes [23]. For the relativistic case where spin-orbit coupling is taken into account, selection rules have been published for the normal emission case only [24].

In this treatment consideration is only given to emission from an fcc (110) surface for simplicity and necessity. In the discussion of the photoemission data in the later chapters, selection rules will be used only for the systems studied with the (110) surfaces. For this reason, only interpretation of the selection rules described herein are considered in the context of normal emission along the Σ-line or in the (001) and $(1\,\bar{1}\,0)$ mirror planes of the (001) surface (Fig. 5).

When comparing photoemission spectra, consideration of which final state contributes in the process must be given. In normal emission along the Σ-line, the final state must be totally symmetric. Otherwise, a node would exist at the detector and the electron would not be counted. This requires that the excitation take place into a Σ_1 final state, where Σ_1 denotes the group theoretical character of the totally

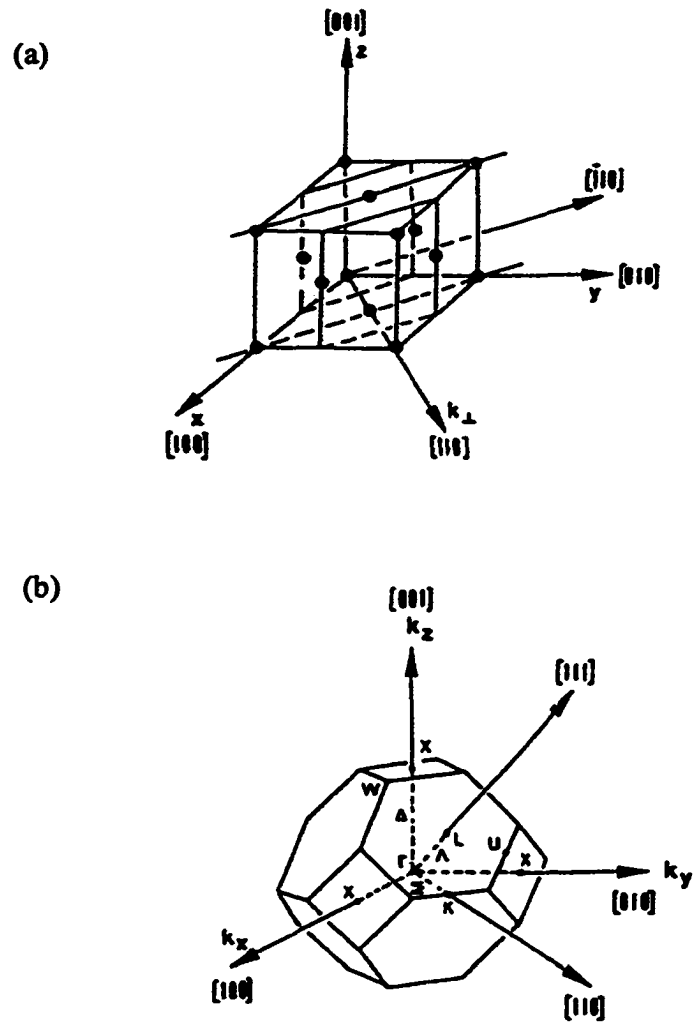

Figure 5. Real space lattice and reciprocal space Brillouin zone for the fcc crystal structure. (a) The mirror planes of the (110) surface are defined by their surface normal vectors, $[\bar{1}10]$ and $[001]$. (b) The high symmetry lines and points are shown for the fcc Brillouin zone, designated by the convention in Ref. 25. The Σ-line is along the surface normal of the (110) plane (from Ref. [21]).

symmetric element in the C_{2v} representation. For the case of emission in a mirror plane, the final states must be even with respect to that mirror plane.

In the electric dipole approximation, selection rules are established from the fact that a non-vanishing transition matrix element of the form $\langle f|\bar{A}\cdot\bar{p}|i\rangle$ must have an initial state with the same symmetry as the dipole operator $\bar{A}\cdot\bar{p}$. In the case of mirror planes in the crystal, if $\bar{A}$ lies in the mirror plane, then the initial state, $|i\rangle$, must be symmetric or even. Likewise, for $\bar{A}$ perpendicular to a given mirror plane, the initial states must be anti-symmetric or odd with respect to that mirror plane. Although non-relativistic selection rules will never be obeyed completely, they will give the dominant contribution to the photoemission spectra, especially for a metal like Cu where relativistic effects are small. Thus, the non-relativistic dipole selection rules serve as a useful guide for interpretation of photoemission spectra collected in the mirror planes and at normal emission.

Table 1 displays the character table for the C_{2v} point-symmetry group. The character representations, Σ_1-Σ_4 are labeled according to the notion set forth by Bouckaert, Smoluchowski, and Wigner [25]. The table displays the parity of each element under the given operations [26]. In this notation, E is the identity operation, J is an inversion, and C_2 is the two-fold rotation about the $[110]$-axis. This then implies that JC_4^2 corresponds to a mirror reflection with respect to the (001) mirror plane, and JC_2 is a mirror reflection with respect to the $(1\bar{1}0)$ mirror plane. From this table, one can see that, for photoelectrons collected in the normal emission geometry, initial states of Σ_1 character are always observed, whereas initial states of

Σ_2 character are never observed. States of Σ_3 and Σ_4 character are observed exclusive of each other, provided the vector potential of the exciting radiation lie in one of the two mirror planes of the crystal.

Table 1. Character table for the C_{2v} point-symmetry group. The table displays the parity of a given representation, Σ_i, under the four symmetry operations of the C_{2v} group.

	E	C_2	JC_4^2	JC_2
Σ_1	1	1	1	1
Σ_2	1	1	-1	-1
Σ_3	1	-1	-1	1
Σ_4	1	-1	1	-1

2.2.3 Photoemission as a Spectroscopy

In practice, photoemission spectra are interpreted as a direct transition between an initial state of energy E_i and a final state E_f, where both energies are measure with respect to the Fermi energy, an experimentally convenient reference. The measured quantity in photoemission is the kinetic energy of an electron, E_{kin}, emitted from the solid and detected at an angle θ relative to the surface normal. If the work function is known, then energies of the initial and final states are obtained by

$$E_f = E_{kin} + \phi, \text{ and } E_f = E_i + \hbar\omega. \qquad \text{(Eq. 12)}$$

In order to get information concerning the band structure of a given material surface, that is $E_i(\bar{k})$, determination of the wave vector must also be made. The determination of the final state wave vector is a more involved process. The momentum parallel to the surface is conserved so that it may immediately be computed using

$$p_{\parallel} = K_{\parallel} = \left[\left(2m/\hbar^2\right)E_{kin}\right]^{1/2}\sin\theta. \qquad \text{(Eq. 13)}$$

The situation with finding $K_{\perp}$ is another matter, because there is no direct relation between the measured quantities $p_{\parallel}$ and $p_{\perp}$ and the quantity $K_{\perp}$. The simplest assumption, that of the free-electron final state model, is widely used and has proved to be extremely successful [21]. In this model the dispersion relation for the final state is assumed to be of the form:

$$E_f = \left(\hbar^2/2m\right)\left(\bar{k}+\bar{G}\right)^2 + E_0, \qquad \text{(Eq. 14)}$$

where these energies are, again, measured with respect to the Fermi energy. Here, the only undetermined parameter is the crystal potential, $V_0 = |E_0| + \phi$. The effective mass of the electron could also be used as a fitting parameter, but for this model it is assumed that $m^*/m = 1$, to a first approximation. For the determination of V_0, one either fits the experimental band structure with a theoretical band structure, or the theoretical muffin-tin zero is used. Both methods are common. This approximation

technique will be demonstrated for the case of normal emission $(k_{\parallel} = 0)$ in later chapters concerning the modified bands of Cu and Ni as seen in the data acquired in this study. In short, the free electron parabola given by Eq. 14, intersects with the bands of the sample giving rise to a peak in intensity in the photoemission spectra, using $E_f = E_i + \hbar\omega$. As the photon energy is varied, the free electron parabola sweeps through the Brillouin zone along the Σ-line, providing a technique to map the bands of the sample under consideration. As will be seen in later chapters, comparing the experimental band structure of the clean substrate with that revealed after heteroepitaxy, gives insight into the hybridization and metallic bonding associated with metals of different elements in highly interacting structures such as surface alloy formation.

The electronic dimensionality of these surface structures plays an extremely important role. Typically, a system is referred to as having a three-dimensional, or bulk-like, electronic structure provided that the energy dispersion of the bands depends on the perpendicular component of the wave vector, as well as being dependent on the components of the wave vector parallel to the surface. Often it is the case that bands are confined to the surface layer where the dependence of the energy on the perpendicular component is negligible due to an exponential decay of the bands into the bulk. These surface states are said to have a two-dimensional electronic structure. As will become evident in the following chapters, the surface structures discussed in this work behave quite differently as compared to bulk-bands or surface states. Often there is a strong coupling to the bulk bands of the substrate, exhibiting a strong dependence on the perpendicular component of the wavevector.

In the plane of the surface, the resultant morphologies are highly anisotropic. As a result, the electronic states may show dispersion along one direction in the plane while none in the other direction of the plane. Therefore, the discussions of dimensionality that follow often have different semantic meanings from the tradition discussions of two- and three-dimensional electronic structure. In this sense, one-, two-, and three-dimensional electronic structures are discussed.

2.3 Instrumentation

2.3.1 UHV STM Chamber

The STM chamber was designed with the premise that it be used both as a stand-alone surface characterization chamber, as well as a sample preparation chamber, to be mounted onto the various photoemission chambers available at the CAMD. These two ideas form a particularly opposing juxtaposition in the concepts of design. On one hand, all of the necessary experimental tools required for a full surface characterization must be available, while on the other hand, the chamber should be made as small as possible so that 1) it mounts conveniently to other endstations and 2) the length of the bellows facilitating sample transfer be as short as possible for cost consideration. The design of this chamber was an exercise in minimization with constraints that tended to drive the size larger. Eventually, the design was optimized and what follows is a brief description of its design and implementation. Details of design and modification can be found in the Appendix.

Figures 6(a-c) show design drawings of the chamber where, even though there are a total of six focal points, the chamber is truly comprised of three cross sectional levels each with a specific functionality. Level one at focal point A is

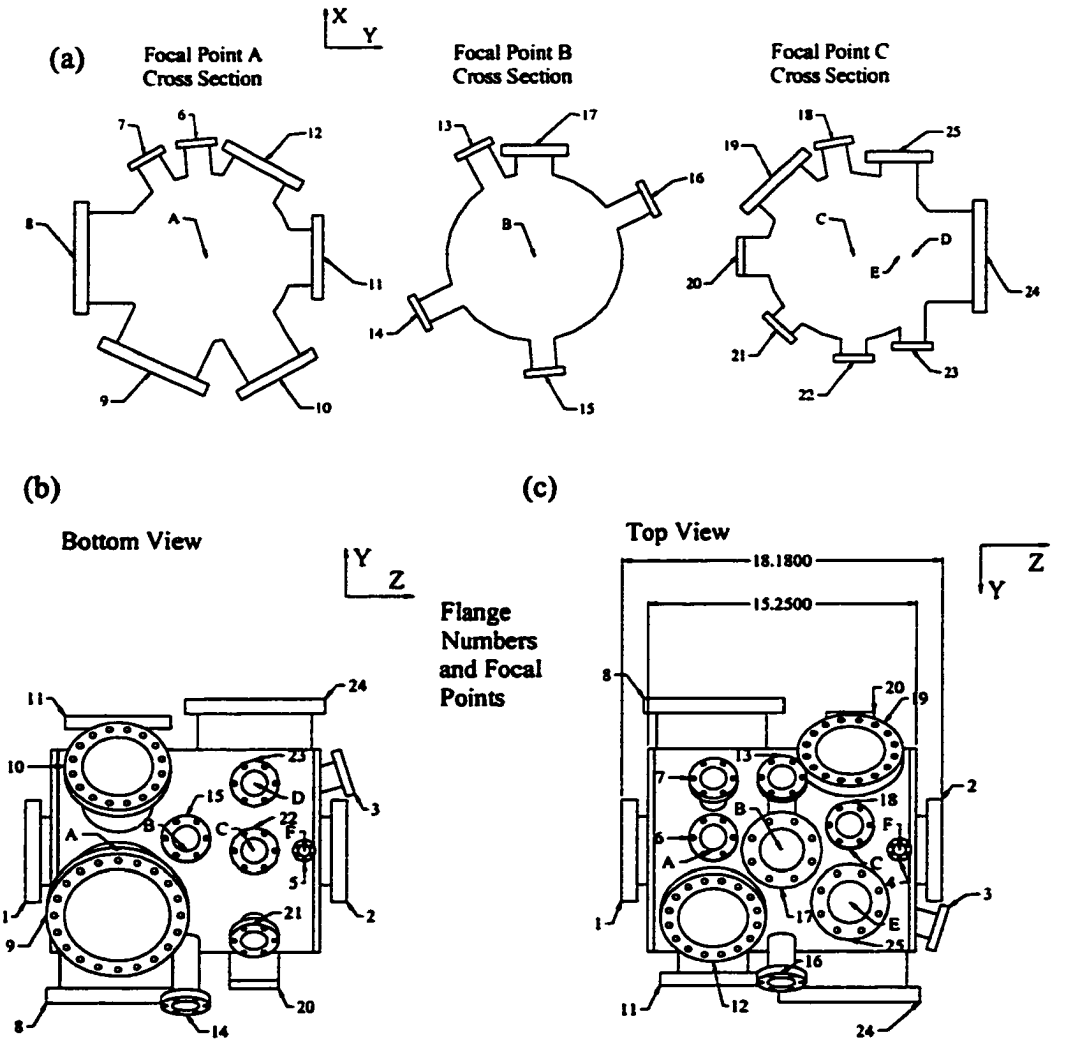

Figure 6. Design drawings of selected views of the UHV STM vacuum chamber. (a) Cross sectional views of the three main levels in the vacuum chamber. (b) Bottom view detailing flange numbers and focal point positions. (c) Top view detailing overall length, flange numbers and focal point positions.

designed for substrate cleaning and preparation. This level is equipped with a sputtering ion gun for cleaning the substrate and Low Energy Electron Diffraction (LEED) optics to determine surface crystalline order as well as a Cylindrical Mirror Analyzer (CMA) for Auger Electron Spectroscopy (AES) to determine cleanliness. This level is also equipped with three viewports and the main pumping port for the chamber. Level two at focal point B is designed for surface modification. There are two ports 180° apart from each other dedicated for two metal evaporators. Ideally, a dual-source resistive–type bead-on-a-filament evaporator mounts into one of the ports while a single source *e*-beam evaporator will bolt to the other. Perpendicular to both of these evaporation ports is a flange-mounted quartz crystal oscillator microbalance thin film thickness monitor. Level two is also equipped with a 4.5-inch viewport and an arbitrary flange used for the quadrapole mass spectrometer. The third level at focal point C is designed for sample manipulation outside of the XYZΘ sample manipulator and holder, and STM characterization. By way of a wobble stick pinscher mechanism, the sample can be removed from the sample holder. From there, the sample can be moved to one of three positions, (1) the STM, (2) the sample storage garage, or (3) the magnetic transfer load-lock system whereby samples may be transferred from atmospheric pressures to ultra-high vacuum conditions within the period of a few hours. Flanges are mounted on either end of the chamber. The first is for mounting the commercially made XYZΘ sample manipulator, and the other has a vacuum gate valve to facilitate mounting of the STM chamber to one of the photoemission endstations available at CAMD. Figure 7 is a photograph of the STM chamber.

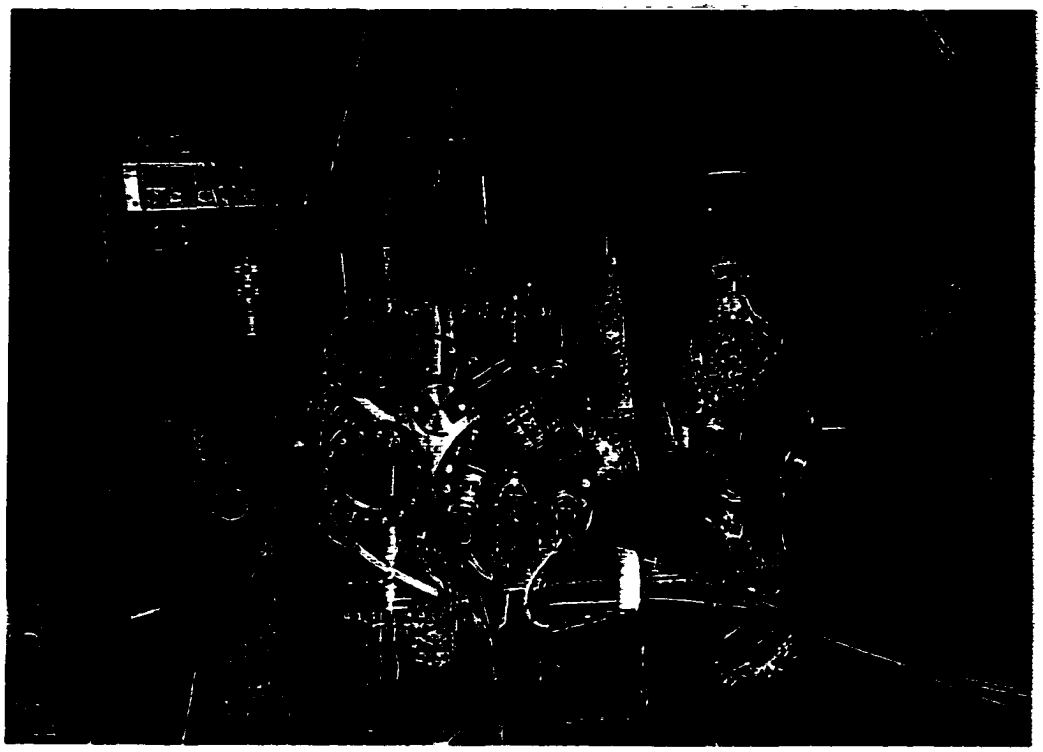

Figure 7. Photograph of the UHV STM vacuum chamber in operation. An auxiliary evaporation chamber was mounted on the far right.

2.3.2 The Aarhus STM

The STM incorporated in the chamber described above is informally known as the Aarhus STM, designed and fabricated by colleagues at the University of Aarhus in Denmark. This STM is the result of many evolutions in design and is thus a highly compact instrument, with high resonance frequencies and extremely fast scanning speeds. In fact, this type of STM is frequently used to make movies of diffusing species on solid surfaces because the scanning speeds are comparable to typical diffusion times on the atomic scale. A schematic of the Aarhus STM design is shown in Fig. 8. What is shown in this figure is housed in a ~ 1 kg Al block, which, due to its characteristically large heat capacity, is used in the variable temperature aspect of the STM's implementation. This design is based on a scanner tube with an outer/inner diameter of 3.18/2.67 mm and a length of 4.0 mm. The material is EBL#2 (Staveley), a hard piezoelectric material with a low Q (80) and a high Curie temperature of 350 °C. Opposite electrodes on the tube are driven asymmetrically for the X and Y deflections and the Z motion is controlled by applying a voltage to the inside electrode. The coarse approach of the tip is facilitated by an inchworm motor consisting of a 3 mm diameter SiC rod fitted into two bearings in a piezotube. The SiC rod is lubricated using MoS_2 powder.

All electrodes are driven by high voltage, low noise amplifiers with a range of ± 200 V. These voltages are driven by 16-bit Digital to Analog converters (DAC) working in the range of ± 5 V. Similar DACs are used for the tunnel voltage, and the set point for the tunnel current. The feed back circuit for constant-current operation consists of a tunnel current preamplifier and a main amplifier. The preamplifier has

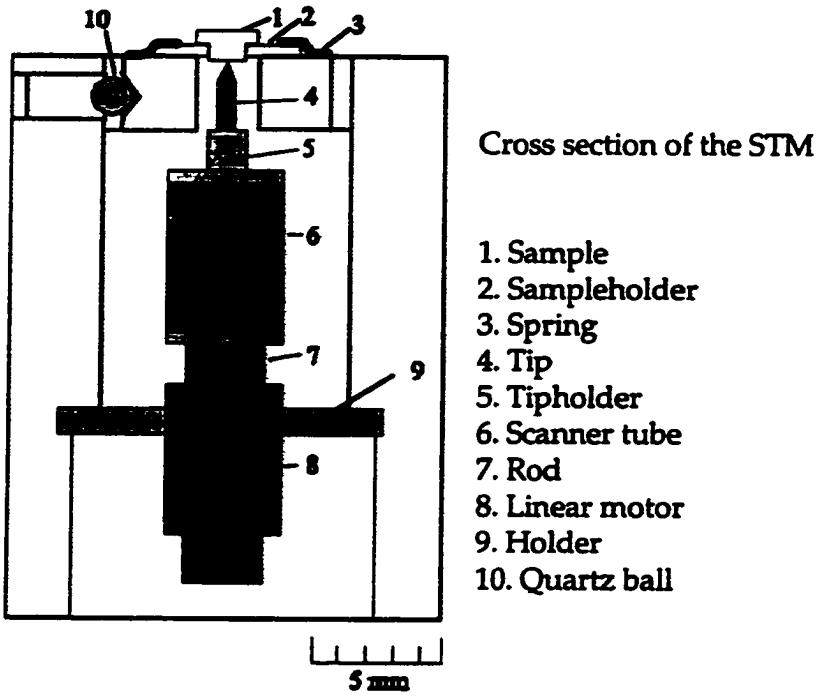

Figure 8. Schematic view of the Aarhus STM. A single crystal (1) is mounted in a Ta holder (2) which is spring-loaded (3) to the top of the STM. The W tip (4) is mounted in a Macor® cap (5), glued onto the scanner tube (6), which again is glued onto the rod (7). The scanner is coarsely approached with the linear motor (8) held by a Macor® ring (9). Everything is built into an Invar® house and, furthermore, the head of the STM is thermally isolated from the rest through three quartz balls (10).

a gain of 1 V/nA. The main amplifier has an adjustable gain of ±110 with 12-bit resolution. A schematic of the STM and electronics is shown in Fig. 9.

The STM top may be cooled by passing liquid nitrogen (LN_2) through a tube in the Al-cradle locking mechanism. Typically, the temperature falls exponentially and it is possible to reach 120 K within a few hours. When cooling the STM, it is necessary to keep the STM scanner tube itself at or near room temperature. This is facilitated though the use of a 75 V Zener diode mounted directly on the bottom of the STM scanner tube. Because the STM scanner is thermally isolated from the cooled Al cradle with Quartz balls, the STM Zener diode only requires about 3-4 mA to keep the STM at room temperature, even with the sample and Al-cradle maintained at 120 K. To take full advantage of the variable temperature aspect of the STM, once the cradle has been cooled below a desired temperature, it may be heated using a well isolated power supply with two 500 Ω, 5 W resistors in series plugged into two Zener diodes built into the Al-cradle. With the total power limited to ~ 16 V, and because the heat capacity of the Al-cradle is ~ 1 kWs/°C, the maximum temperature rise is on the order of 1°C per minute.

2.3.3 CAMD Analyzer

All photoemission data collected in the experiments described herein used a separate vacuum system, from the one described above. This system incorporates a hemispherical energy electron analyzer capable of measuring the energy of charged particles emitted from a sample at any angle relative to the surface or the incident beam of exciting particles [27]. This hemispherical analyzer is operated with a constant pass energy and uses a series of electrostatic lenses. This system is properly

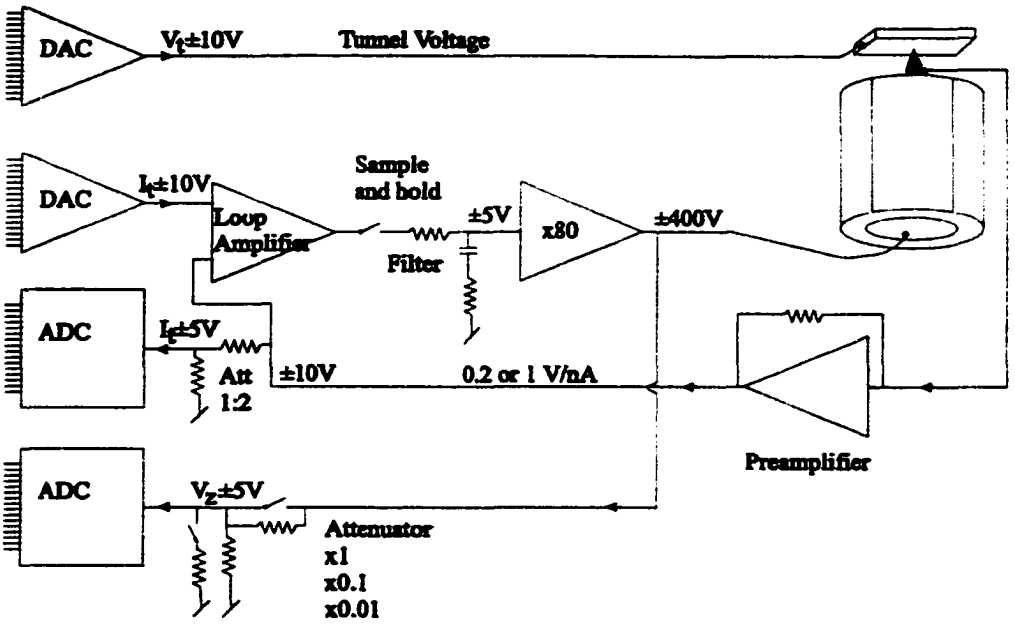

Figure 9. Schematic view of the electronics for the Aarhus STM. Although the voltage amplifiers are label with ±400 V, the unit obtained uses ±200 V amplifiers. In constant current mode, the *z* voltage is controlled by a feedback loop consisting of the tunnel junction, the preamplifier, the loop amplifier, a high voltage amplifier and finally the piezo tube which converts voltage into displacement (13 Å/V).

apertured to accept incoming particles from a spot size of 1.5 mm diameter with an acceptance cone of 2.5° half-angle. A schematic of the lens system is shown in Fig. 10. The electronics used for this system include a set of lens power supplies floating on top of the sweeping voltage used to energetically select the kinetic energy of the photoemitted electrons. The lens curves used for this system are linear and their slopes and intercepts are shown in Table 2.

The angular motion of the analyzer is accomplished through drive mechanisms using two rotary motion feedthroughs. The analyzer can be positioned with any set of polar and azimuthal angles, however these two motions are not uncoupled. Since the azimuthal drive is located on the polar drive mechanism, this results in a coupling of the two motions making the selection of a given angle slightly less trivial. For example, a rotation in polar angle of 1° requires an additional rotation in the azimuth by 1°, in order to remain in the same polar plane.

2.3.4 PGM Beamline

The plane grating monochromator (PGM) beamline was used in all photoemission experiments to focus the incident radiation onto the samples. This beamline is well-described elsewhere [28], and will be briefly outline here. The PGM at CAMD was designed to adequately cover an energy range from about 20 eV to 2000 eV using two plane gratings, a high energy grating with 1220 grooves per mm and a low energy grating with 360 grooves per mm. The beamline contains five mirrors and employs an entrance and an exit slit. The entrance slit is incorporated in the design of the beamline in order to keep energy resolution and calibration of the monochromator independent of source size and stability. Decreasing the size of the

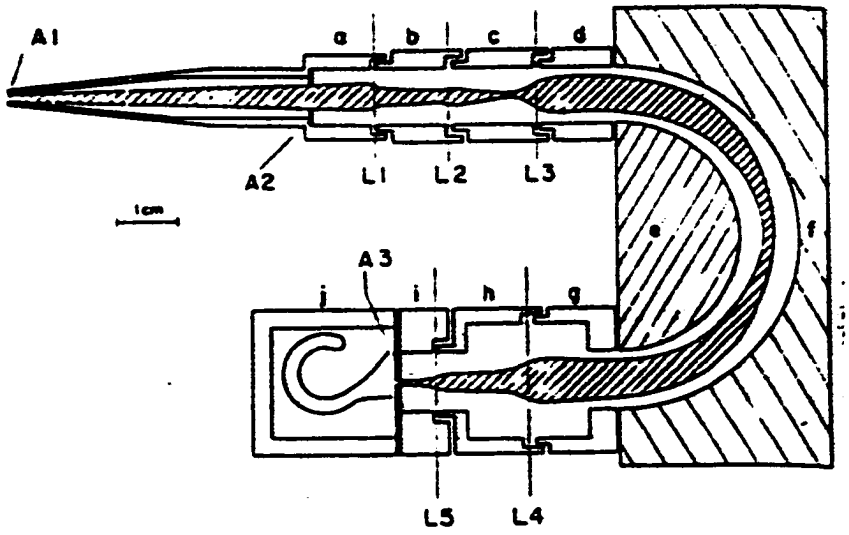

Figure 10. Schematic layout of the CAMD hemispherical electron energy analyzer (from Ref. [27]).

Table 2. Slopes and intercepts of the lens curves for the CAMD analyzer. The format of the table is slope/intercept for lens voltage versus sweep voltage.

	1 eV Pass Energy	2 eV Pass Energy	4 eV Pass Energy
Lens 1	0.609/2.103	0.809/0.988	0.843/0.993
Lens 2	0.933/4.321	0.926/6.967	1.00/10.07
Herzog	1.00/1.012	1.00/2.005	1.00/4.009
Inner Hemisphere	1.00/1.505	1.00/2.995	1.00/5.957
Outer Hemisphere	1.00/0.682	1.00/1.346	1.00/2.689
Lens 5	1.00/24.89	1.00/24.89	1.00/24.89
Lens 6	1.00/175.55	1.00/175.55	1.00/175.55

exit slit increases the energy resolution of the beamline, while, at the same time, decreasing the intensity. The parameters of the optical components in the beamline are summarized in Table 3, with a schematic layout given in Fig. 11. Typically the spot size for this beamline is ~ 1 mm^2 and the combined resolution of the beamline/analyzer system is on the order of 0.3 eV.

2.3.5 CAMD Synchrotron

The final element involved in the photoemission experiments to be described is actually where the whole process begins: the synchrotron radiation source. CAMD is a 1.3 (1.5) GeV electron storage ring with the capability of providing bending magnet radiation from eight dipole bending magnets as well as having a 7.0 T superconducting Wiggler insertion device. Electrons are injected into the synchrotron using a 200 MeV linear accelerator, and consequently ramped up to 1.5 GeV. Typically injected currents at 1.3 GeV are around 200 mA while at 1.5 GeV currents are injected on the order of 150 mA. In contrast to other synchrotron radiation facilities around the world, CAMD is designed to be optimized for developing X-ray lithography based techniques for manufacturing microcircuits and devices. Therefore, CAMD is not a brilliant source although it is reliable and is in operation ~ 16 hours per day, on average. Characteristic intensity versus photon energy plots are shown in Fig. 12.

There are many advantages to synchrotron radiation, mainly because of the relativistic energies to which the electrons are accelerated. As the electron beam passes through a dipole-bending magnet, a very intense radiation emerges in a continuous spectrum approximately 10^6 times brighter than conventional sources.

Table 3. Parameters for the optical components in the PGM beamline (from Ref. [28]).

	Figure	Size (mm)	Radius (mm)
M1	Cylinder	330×30	193
M2	Cylinder	330×30	103125
M3	Plane	120×30	∞
PG	Plane	110×30	∞
M4	Sphere	250×30	288120
M5	Toroid	100×30	4000052.3

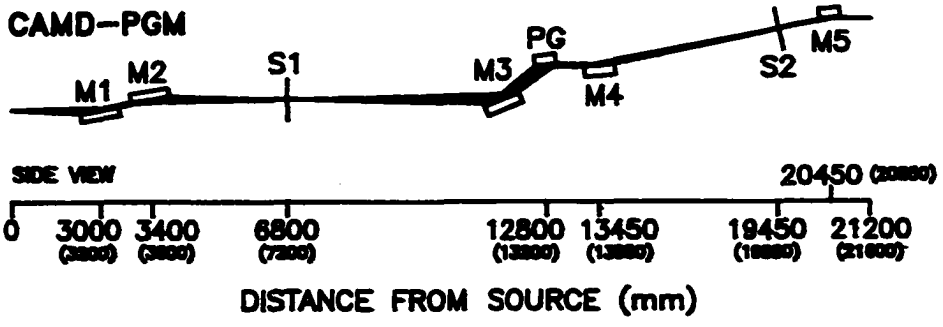

Figure 11. Schematic layout for the PGM beamline (from Ref. [28]).

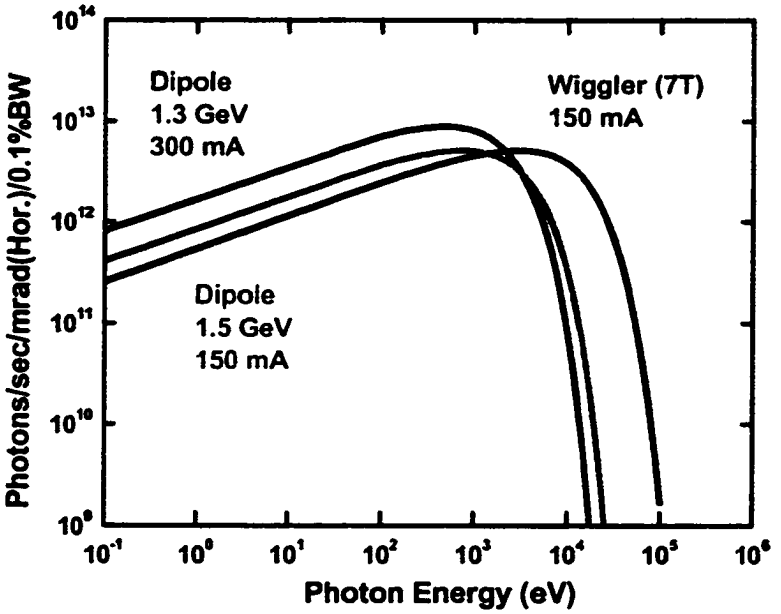

Figure 12. Characteristic intensity versus photon energy curves for CAMD.

The radiation is very strongly linearly polarized with a very small emission angle, which scales as

$$\theta \sim \gamma^{-1} = \left(\frac{E}{mc^2}\right)^{-1}, \qquad \text{(Eq. 15)}$$

where E is the energy of the operating ring. With the synchrotron operating at 1.3 GeV, $\theta \sim 0.3$ mrad. The power dissipated in synchrotron radiation varies as the energy to the fourth power and scales linearly with the electron beam current. With typical values characteristic of the CAMD facility, the radiation emerging from the accelerator is on the order of 10 – 15 kW.

In the chapters that follow, descriptions and discussions of the individual experiments are expounded. Because the experimental details of each experiment are somewhat different, short descriptions detailing these differences are outlined. For this reason, the present chapter contains experimental details virtually common to all. The following chapters basically follow the same format. First a background is given, and then specific experimental details are outlined. The results for the atomic structure followed by the electronic structure are given. Finally, each chapter is wrapped up with a discussion of the correlations observed between the atomic and electronic structures as well as common aspects similar to them all.

Chapter Three

Ag/Cu(110)

3.1 Introduction/Background

This chapter is concerned with the unique surface morphology and electronic structure of sub-monolayer deposition of Ag on the Cu(110) surface. STM reveals the growth of Ag on this surface, in the low coverage regime ($0 < \theta_{Ag} < 0.4$ ML), as the formation of a surface-confined, substitutional alloy phase. Driven by the compressive strain in this phase (13 % lattice mismatch), further deposition leads to the formation of de-alloyed zigzag chains of Ag dimers and trimers ($0.4 < \theta_{Ag} < 0.6$ ML), where the Ag/Cu surface alloy remains between the chain structure. As the Ag coverage is increased ($0.6 < \theta_{Ag} < 0.9$ ML), the chains coalesce to form a broad, striped morphology [29]. It is this coverage regime in which the electronic structure data were collected. As detailed below, this resultant surface morphology is quite unique, and results in a surface with reduced symmetry from the native C_{2v} symmetry of the Cu(110) crystal face. This reduction in symmetry becomes apparent in the photoemission data, the discussion of which forms the bulk of this

chapter. A discussion of electronic dimensionality then follows. First, a brief history of previous work regarding silver deposition on copper is given with special attention to the photoemission investigations.

Very little experimental work has been performed on Ag heteroepitaxy on the (110) surface of copper [30]. There have been numerous investigations for both atomic and electronic structures of clean Cu(110) (all low index faces for that matter), and monolayer coverages of Ag on Cu(100) and Cu(111) have been studied using angle-resolved photoelectron spectroscopy. Originally Ag overlayers on Cu(100) were studied using LEED and AES [31]. These studies were performed in order to determine the depth of the surface region, which contributes to Auger peaks. In these studies, a hexagonal Ag monolayer was observed to from a c(10 × 2) surface structure in which the overlayer conformed to the substrate rather than assuming its own lattice constant. With respect to the bulk lattice constant of Ag, conformity of the Ag overlayer to the Cu substrate with this c(10 × 2) unit mesh requires a 1.7% compression along the Cu [110] and a 2% expansion in the Cu $[\bar{1}10]$ direction [32]. Taylor *et al.* investigated the deposition of Ag on Cu(110) using LEED and AES, however as will be shown below, their results for the initial phase of epitaxy may have been interpreted incorrectly [30].

The electronic structure of the c(10 × 2) Ag/Cu(100) system was investigated by Tobin *et al.* [33]. In their photoemission studies, the development of the electronic dimensionality from a two- to three-dimensional structure was observed. At coverages of 1-2 monolayers, the *d*-bands of the Ag adlayer exhibit a

characteristic two-dimensional dispersion, whereas increased coverages, 3-5 ML, result in a bulk-like three-dimensional electronic structure.

In a somewhat similar study of Ag overlayers on the Cu(111) surface, it was determined that a layer-by-layer growth mode occurs despite the large lattice mismatch between Ag and Cu [34]. Very similar to the dimensional evolution observed by Tobin, Shapiro *et al.* observed the Cu(111) surface state at $\overline{\Gamma}$ evolve to the Ag(111) surface state at $\overline{\Gamma}$ as a function of Ag coverage. This is the result of a very well ordered growth process occurring on this close-packed surface.

Not only are these previous studies different from the one presented here due to the fact that a different crystal surface was used, but the other fundamental difference lies in the coverage regimes investigated. While it is true that monolayer deposition of Ag on Cu(110) results in a two-dimensional hexagonal overlayer, virtually identical to the systems studied by Tobin and Shapiro, and observed by Taylor, emphasis in this study is placed on the initial states of growth, i.e. in the submonolayer coverages of Ag on Cu, the electronic structure of which has never been previously reported.

3.2 Surface Morphology of Ag/Cu(110)

The atomic structure, or surface morphology, of Ag/Cu(110) has been previously investigated as a function of coverage by Sprunger *et al.* [29]. The STM results for this system closely resemble those found for the Au/Ni(110) system detailed by Nielsen *et al.* [35], and despite previous studies by Taylor *et al.* describing Ag/Cu(110) as a simple non-alloyed Ag overlayer, Sprunger's low

temperature STM data rebut the results of Taylor, showing that Ag atoms in fact do alloy into the open Cu(110) surface.

At very low coverages (~ 0.25 ML) of Ag, this surface alloying is observed to occur at 150 K, whereby Cu atoms are exchanged out of the surface layer, resulting in small Cu islands nucleating and growing on the terraces of the surface. When this system is annealed to 350 K and subsequently imaged at low temperature, the Cu islands are observed to have disappeared as a result of step flow, and atomically resolved STM images reveal substituted Ag atoms preferentially aligned along the [001]-direction. This is a result of the excess strain energies involved. Because of the anisotropic Cu(110) surface, the Cu-Cu distance along the [001] is 3.61 Å, whereas along the $[1\bar{1}0]$, this near-neighbor distance is 2.56 Å. With a Ag bulk near-neighbor distance of 2.89 Å, the alloyed Ag atoms are subjected to a compressive strain along the $[1\bar{1}0]$, and in order to minimize energy, the Ag atoms thus preferentially align along the [001] [29].

As the coverage is further increased, a de-alloying process occurs as a result of increasing strain energies associated with the substitutional Ag atoms. Figure 13 shows an STM image collected at 150 K after deposition of ~ 0.4 ML of Ag at 400 K. The emergence of the characteristic zigzag dimer-trimer chains is noticed immediately. Between the chains small protrusions corresponding to the alloyed Ag atoms remain within the Cu surface. As mentioned above, the driving force for this chain formation is the reduction in surface strain caused by an increased concentration of substituted Ag atoms. Cu vacancies play an integral part in stabilizing these chains. The Cu vacancies are a result of relieving increased

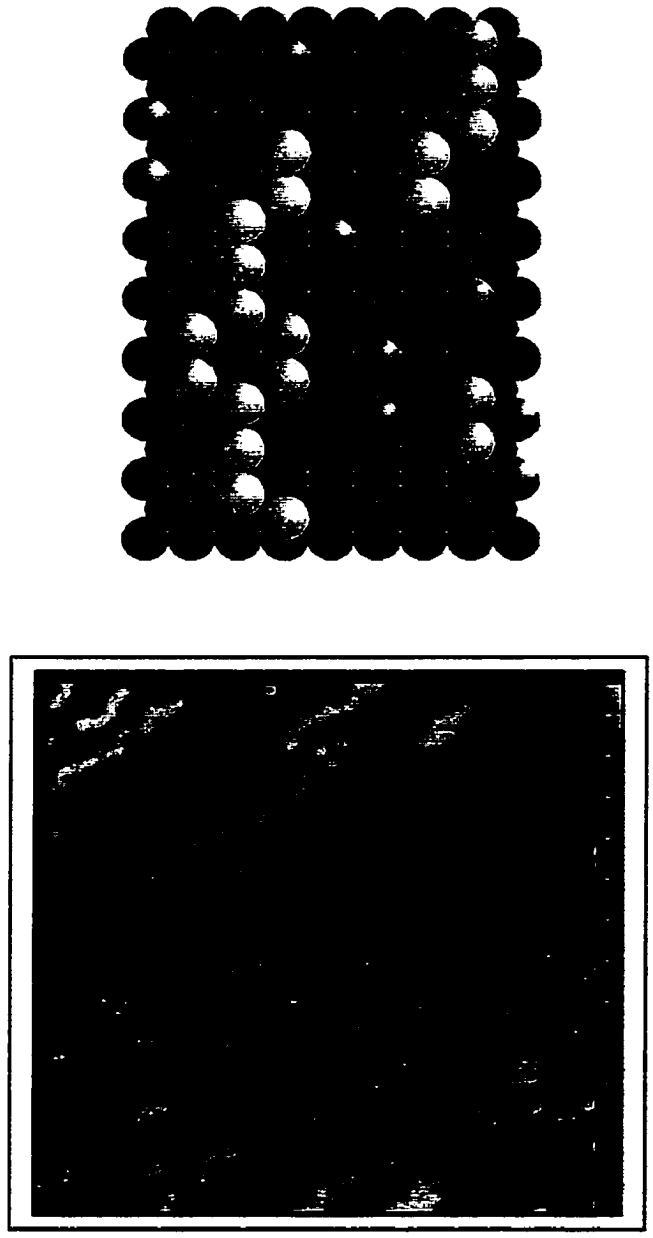

Figure 13. Surface morphology of 0.4 ML of Ag on Cu(110). (a) Ball model depicting the alloyed Ag atoms (red) and the vacancy stabilized dimer-trimer chains (yellow). (b) STM image (200 Å × 200 Å) showing zigzag chain morphology. [001]-direction along chains from bottom-left to top-right (from Ref. [29]).

compressive stress induced by the substitution of the larger Ag atoms into the Cu surface. The formation of vacancies costs energy by decreasing the coordination number of surrounding atoms, however, by adsorbing Ag atoms on top of the vacancies, this energy cost is then compensated. Although this dimer-trimer vacancy-stabilized chain structure is very similar to that seen for Au/Ni(110) [35], it is extremely unique in that it provides for a surface with a highly modified crystal potential, which will be shown to have a substantial impact on the electronic structure of the system. At higher coverages (0.6-0.9 ML) the chains begin to coalesce (Fig. 14), forming a well-ordered precursor to a simple hexagonal Ag(111) overlayer (~ 1.3 ML) resting on top of a non-alloyed substrate analogous to the Ag/Cu(100) and Ag/Cu(111) systems. In addition to the existence to Cu vacancies, this striped hexagonal precursor phase is slightly incommensurate to the substrate, with Ag atoms not resting in the anticipated two-fold hollow sites. This is the origin for the reduced symmetry at the interface observed in the photoemission data.

3.3 Electronic Structure of Ag/Cu(110): Results and Discussion

The angle-resolved photoemission spectroscopy experiments were performed in the spring of 2000 at CAMD. The copper crystal, purchased from Monocrystals Co., was designed to have a top-hat shape (Fig. 15), cut and polished with a maximum 0.5° miscut angle with respect to the (110) crystallographic plane. After performing Laue X-ray diffraction with the help of Gary Ownby at Oak Ridge National Laboratory (ORNL), it was determined that the surface was actually miscut with an angle of ~ 1°, and was not electropolished. Therefore alignment to within ¼° and subsequent crystal polishing was performed. The Cu polishing was done

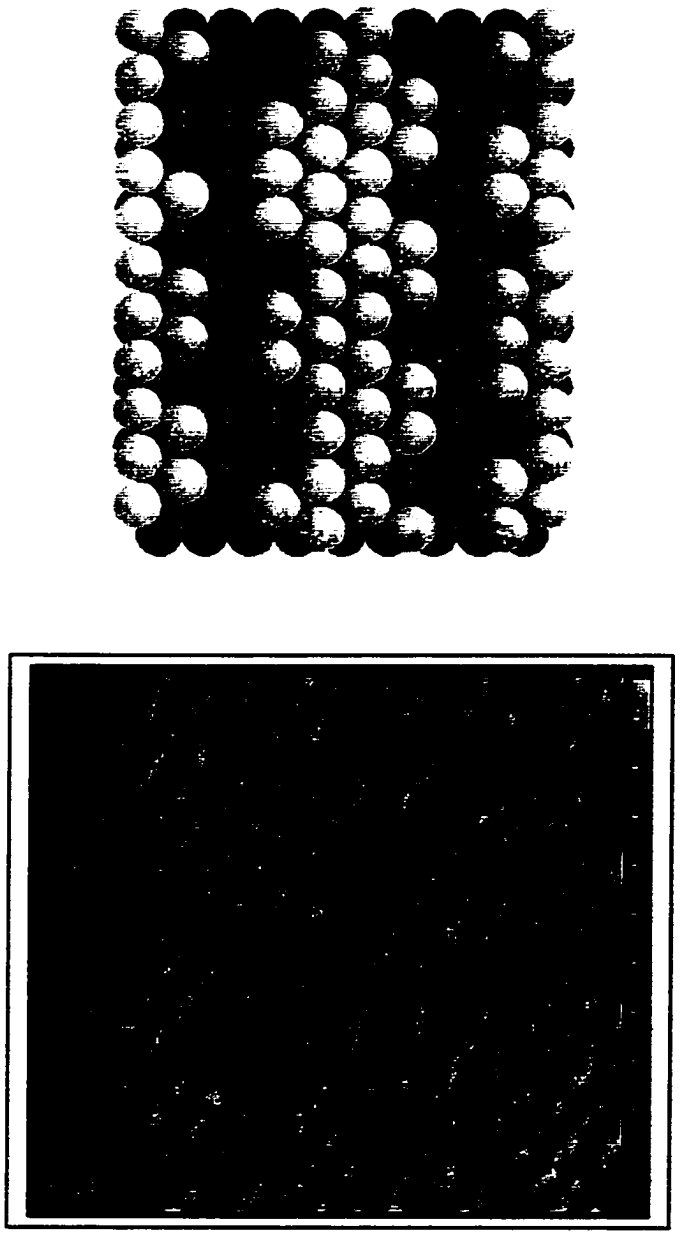

Figure 14. Surface morphology of 0.65 ML of Ag on Cu(110). (a) Ball model of the Ag/Cu(110) coalesced chains. (b) STM image (300 Å × 300 Å) showing the coalescence of the chains, a precursor to the hexagonal overlayer phase (from Ref. [29]).

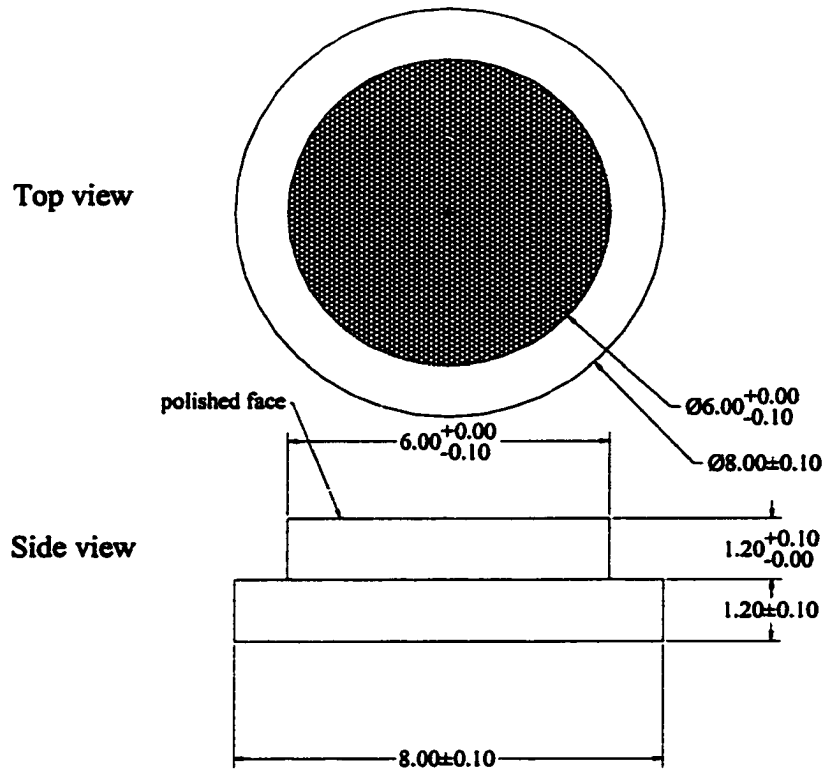

Figure 15. Design drawing of the Cu(110) crystal.

using decreasing grit sizes of solutions of Alumina, followed by a Cu electrochemical polish. Once the crystal was introduced into the vacuum chamber, it was further cleaned by repeated cycles of ion sputtering, using Ne^+ at 1 keV and 15 mA emission current, followed by annealing to 825 K. Typical ion sputtering conditions are at pressures of 5×10^{-5} Torr with ~ 10 $\mu A/cm^2$. Annealing was facilitated by resistive heating using an AC current source (Varian TSP controller). Once the crystal is deemed clean by UPS and of good order as determined by LEED, the crystal was rotated on the sample holder in order to align the crystallographic mirror planes with the polarization of the synchrotron radiation. As mentioned in section 2.2.2, alignment of the [001]-direction perpendicular to the vector potential, $\bar{A}$, of the incident radiation allows for transitions from initial states of Σ_1 and Σ_4 character, while alignment of the $[1\bar{1}0]$-direction perpendicular to $\bar{A}$ allow transitions from initial states of Σ_1 and Σ_3 character. For all spectra collected in this Ag/Cu(110) study, the incident light was *p*-polarized with a 45° angle of incidence. The Ag was vapor deposited from a resistively heated W-crucible characterized with a deposition rate of 0.001 ML/sec using currents of ~5 A.

Starting from the clean Cu(110) crystal and using various photon energies in the normal emission geometry, bulk band structure, along the Σ high symmetry line, was determined. These results agree well with previous experimental [36] and theoretical studies [37]. It is necessary to emphasize that on the clean Cu(110) surface the non-relativistic selection rules pertaining to the allowed transitions are strongly obeyed. That is, upon rotating the crystal about the surface normal, the appropriate states of a given symmetry representation are observed. EDCs for the

clean Cu(110) for various photon energies and photoemission geometries are shown in Fig. 16, depicted as solid lines without symbols. The Cu *d*-bands are seen to be from ~ 2 to 4.5 eV, and the Cu *sp*-band (Σ_1) is visible in Fig. 16 (b) at ~ 1 eV. Fig. 16 (a) and (b) corresponds to the photoemission geometry with $A \perp [001]$ and $A \perp [1\bar{1}0]$, respectively. Fig. 17 also shows data from the clean Cu(110), depicted as solid squares without lines, mapped onto the theoretical band structure of Burdick [37], using the free electron final state approximation.

Following deposition of ~ 0.65 ML of Ag, the EDCs in Fig. 16, depicted with symbols, were obtained. The Ag *d*-states can be seen with energies between 4.5 to 7 eV. Of particular interest is the emergence of new states, denoted as *A* and *B* in Fig. 16 (a) and (b), respectively. Although these new states appear after deposition of Ag and thus may be attributed to those of Ag, an examination of the band structure of Ag reveals no bands remotely close to these energies. Even though Ag and Cu are noble metals both with their filled *d*-bands substantially removed from the Fermi edge, the amount of energetic overlap between the *d*-bands is negligible.

Assuming that these newly appearing states are derived from Cu bands, a comparison of the spectra of the clean Cu(110) and that of Ag/Cu(110) reveal that each state, *A* and *B*, are nearly energetically equivalent to the bulk Cu states of Σ_3 and Σ_4 character, respectively. Because of this, it is asserted that these newly observed states, *A* and *B*, are surface resonances, or modified bulk states, of the Cu atoms in the interfacial region, i.e. between the coalesced Ag dimer-trimer chains and the Cu bulk. There are some notable aspects of these observed states that will be addressed in what follows. These include: the energy shifts from the bulk states

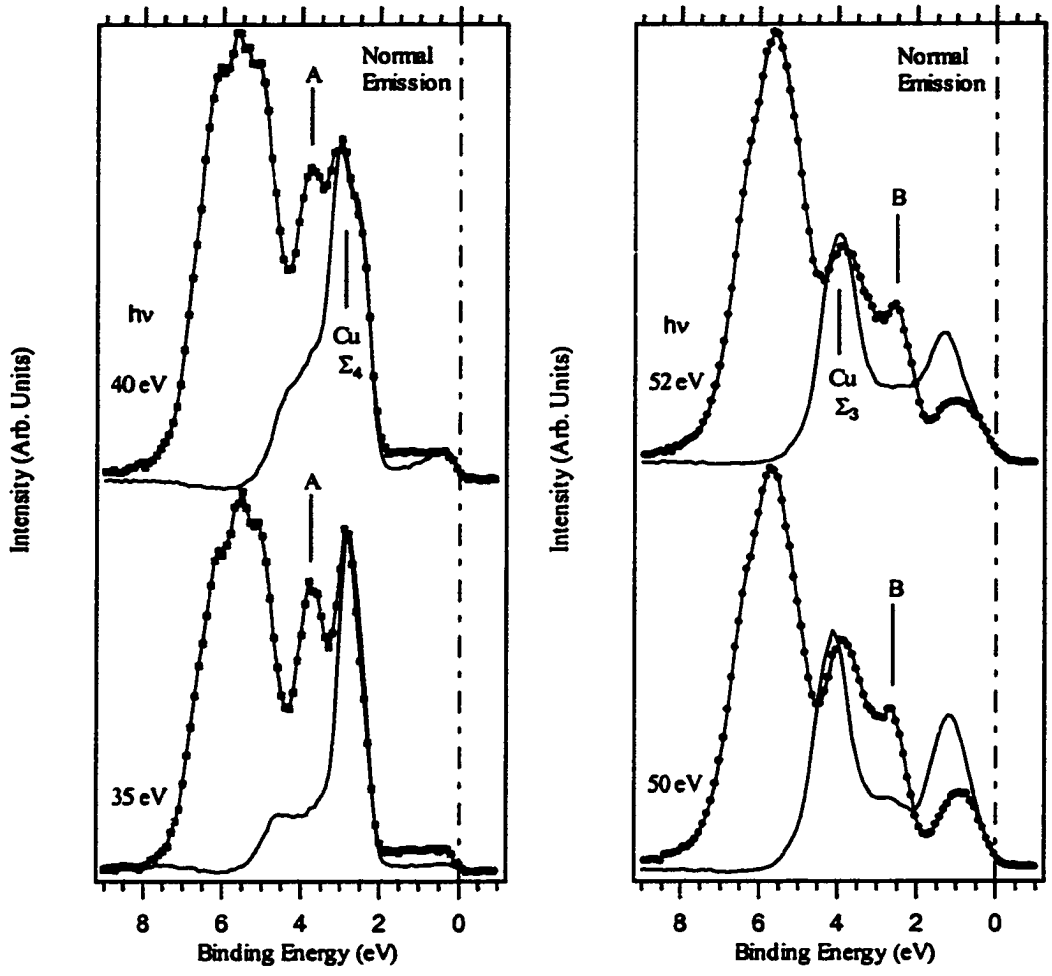

Figure 16. EDCs of clean Cu(110) (curves without symbols) and Ag/Cu(110) with a coverage of 0.6 ML (curves with symbols). (a) $\vec{A} \perp [001]$. (b) $\vec{A} \perp [1\bar{1}0]$. Different photon energy spectra are shown that exhibit clearer resolution of resonances, labeled as A and B. State A (B) is derived from the Cu $\Sigma_{3(4)}$ band, however it is observed in a "forbidden" photoemission geometry because of the reduced symmetry of the surface.

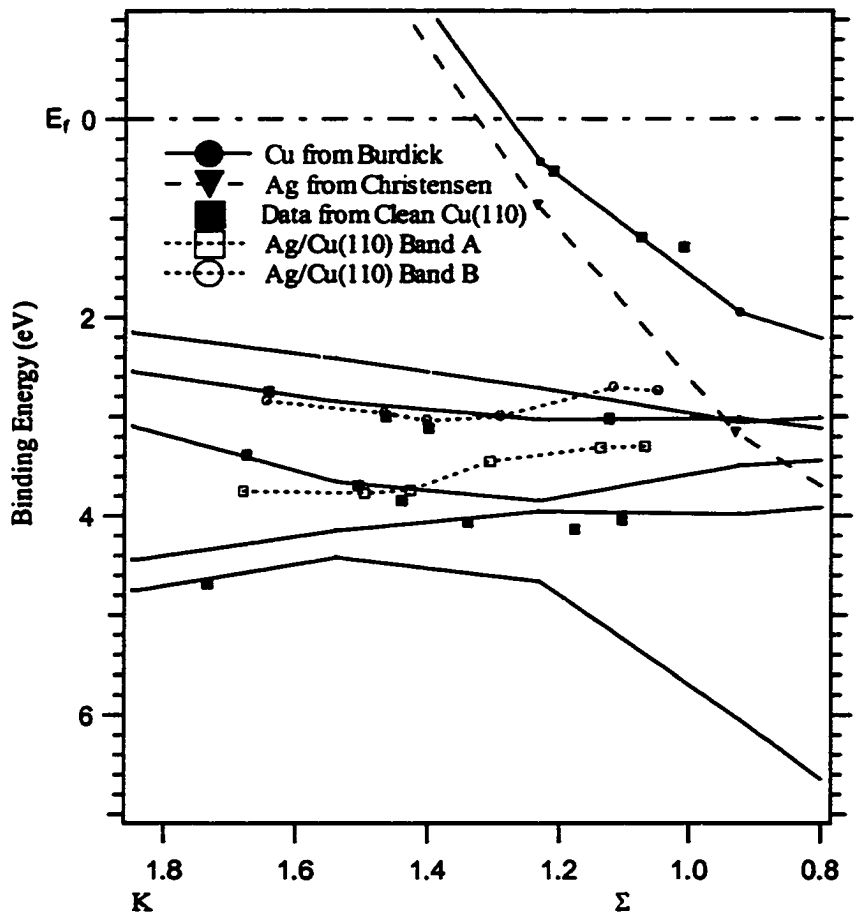

Figure 17. Experimental bands mapped onto theoretical band structure of Burdick [37]. Open symbols connected with dotted lines show dispersion of resonances labeled A and B from Fig. 16. Solid squares are data from clean Cu(110). Ag *sp*-band from Christensen [38] is for qualitative purposes. Bands A and B disperse away from the states from which they were derived as they approach the apparent crossing of the Ag *sp* and Cu *d*-bands.

from which they are derived; the dispersion of these states through the Brillouin zone along the Σ-line; and the symmetry of these states. Finally, the mechanism responsible for this surface resonance phenomenon is proposed.

As mentioned above, states labeled with *A* and *B* in Fig. 16 are nearly energetically equivalent to two Cu bulk states. As seen in Fig. 17, these new states, depicted with open symbols and connected with dotted lines, map very closely with the bands of clean Cu when the wave vector is closer to the Brillouin zone edge. As the dispersion of the states along the Σ-line approach the zone center, these resonances begin to disperse quite differently from the measured bulk dispersion of the substrate. For qualitative purposes the Ag *sp*-band (dotted line) as calculated by Christensen has been displayed, although it is acknowledged that the precise alignment is not absolute because the real crystal potential in this case is not known [38]. As the measured dispersion of the Cu resonances approaches the crossing of the apparent Ag *sp*-band with the Cu *d*-bands, the energy splitting from the bulk states from which they were derived increases, dispersing to lower binding energy. This suggests that the mechanism for the modification of the Cu bands near the surface is induced through hybridization between the Ag *sp*- and Cu *d*-bands.

In the case where the symmetry of the surface is strictly maintained, hybridization between states of different symmetries may not be allowed. Specifically, if the Cu *d*-bands under consideration are of symmetry character Σ_3 and Σ_4 and the Ag *sp*-band has character Σ_1, then hybridization may be symmetry forbidden. However, it is important to distinguish here that this hybridization concerns mixing of states between different atoms, not hybridization between states

in a given atom. The hybridization referred to here is much less restrictive because as a new material is made through epitaxy, a renormalization occurs thereby allowing states of originally different symmetry character to have a non-zero overlap integral. Moreover, the symmetry in this surface is not maintained as can be seen from the photoemission and STM data. It has been shown that state *A* is derived from the Cu bulk band of Σ_3 symmetry. In the photoemission geometry corresponding to Fig. 16 (a), only states of Σ_1 and Σ_4 are allowed transitions, assuming that the C_{2v} symmetry group is maintained in the Ag/Cu(110) system. Similarly, state B is derived from the Cu bulk band of Σ_4 character and should not be observed with the photoemission geometry of Fig. 16 (b). This, together with the known modifications of the atomic geometric structure, suggests that the symmetry of the surface has been reduced. This reduction of symmetry enhances hybridization between the Ag *sp*- and Cu *d*-bands and provides the mechanism for the modification of the Cu bands near the surface. Because of the disorder in the Ag structure (see Fig. 14), it may be more fitting to discuss this hybridization in terms of Ag atomic orbitals, rather than "bands", perturbing the Cu *d*-bands. However, in either case, the consequent structure of this submonolayer phase provides the necessary reduction in symmetry in the Cu bands to allow for this *sp* - *d* hybridization to occur.

When considering the Ag *d*-bands in this system, two sets of data are analyzed to elucidate the nature of the dimensionality. First, consideration is given to normal emission data where the dispersion of the Ag *d*-bands is dependent only on the perpendicular component of the wave vector ($k_{\parallel} = 0$ for normal emission) by varying the photon energy. Depending on the crystal orientation with respect to the

polarization of the exciting radiation, the dimensional nature of the Ag *d*-bands is seen to reflect the anisotropic morphology of the de-alloyed phase in Ag/Cu(110). The second set of data necessary to determine two- or three-dimensional behavior is comprised of off-angle data where the projection of the bands onto the surface Brillouin zone can be mapped. If a system has a two-dimensional electronic structure then 1) bands will not disperse with the perpendicular component of the wave vector, i.e. as a function of photon energy, and 2) bands mapped in the surface Brillouin zone will disperse in the same manner for data collected with different values of $k_{\perp}$, (different photon energies).

In the case of Ag/Cu(110) at around 0.6 ML, the highly anisotropic morphology of the zigzag chains is exhibited in the dimensionality of the Ag *d*-bands. Figure 18 shows EDCs of 0.6 ML of Ag/Cu(110) collected at normal emission for various photon energies with the vector potential perpendicular to the $[1\bar{1}0]$-direction. This geometric set up provides information concerning the nature of the states related to the direction along the chains. As can be seen from Fig. 18, the Ag *d*-bands in this case show very little dependence on the perpendicular component of the wave vector. In contrast, with the crystal rotated by 90° from the geometry of Fig. 18, it is seen that there is a stronger dependence on the perpendicular component, indicating as stronger interaction between the Ag and the bulk-like Cu (Fig. 19).

Figure 20 is a band map of the Ag *d*-bands throughout the surface Brillouin zone, along the high symmetry directions. This plot is a compilation of data from many different EDCs collected at various off-angles for two different photon

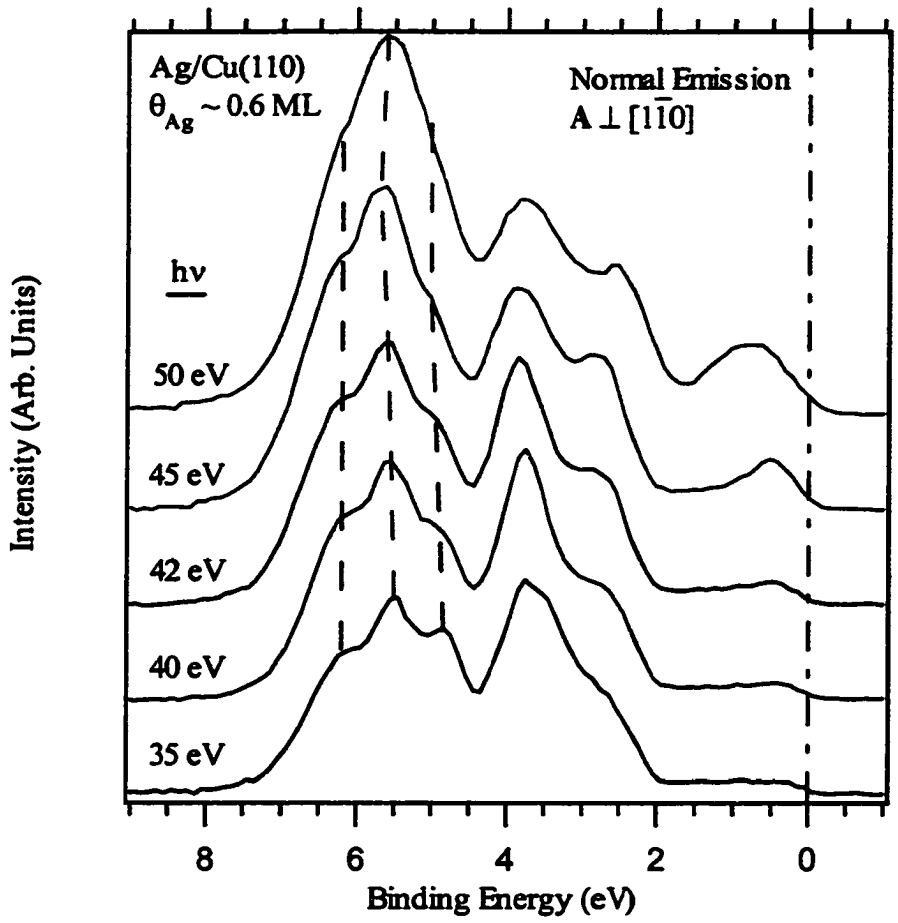

Figure 18. EDCs of 0.6 ML of Ag/Cu(110) collected at normal emission for various photon energies with $\bar{A} \perp [1\bar{1}0]$. The negligible dispersion for this geometry indicates a one-dimensional electronic structure along the Ag chains.

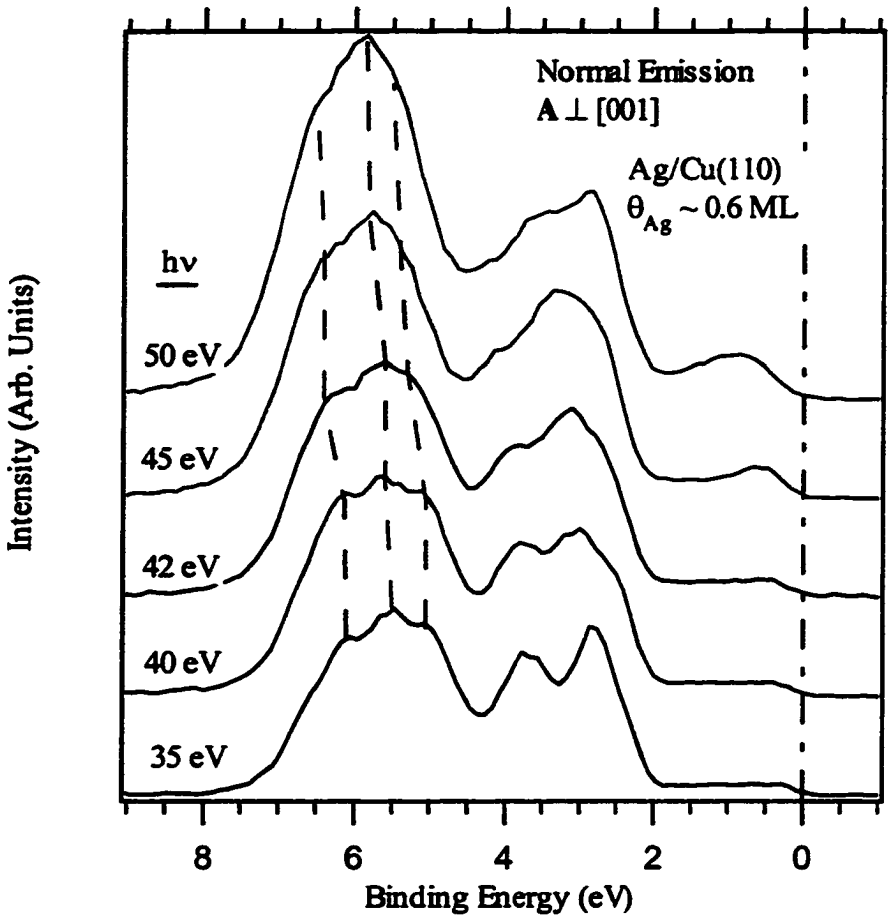

Figure 19. EDCs of 0.6 ML of Ag/Cu(110) collected at normal emission for various photon energies with $\bar{A} \perp [001]$. Substantial dispersion indicates a strong coupling of the Ag chains to the Cu bands perpendicular to the chains.

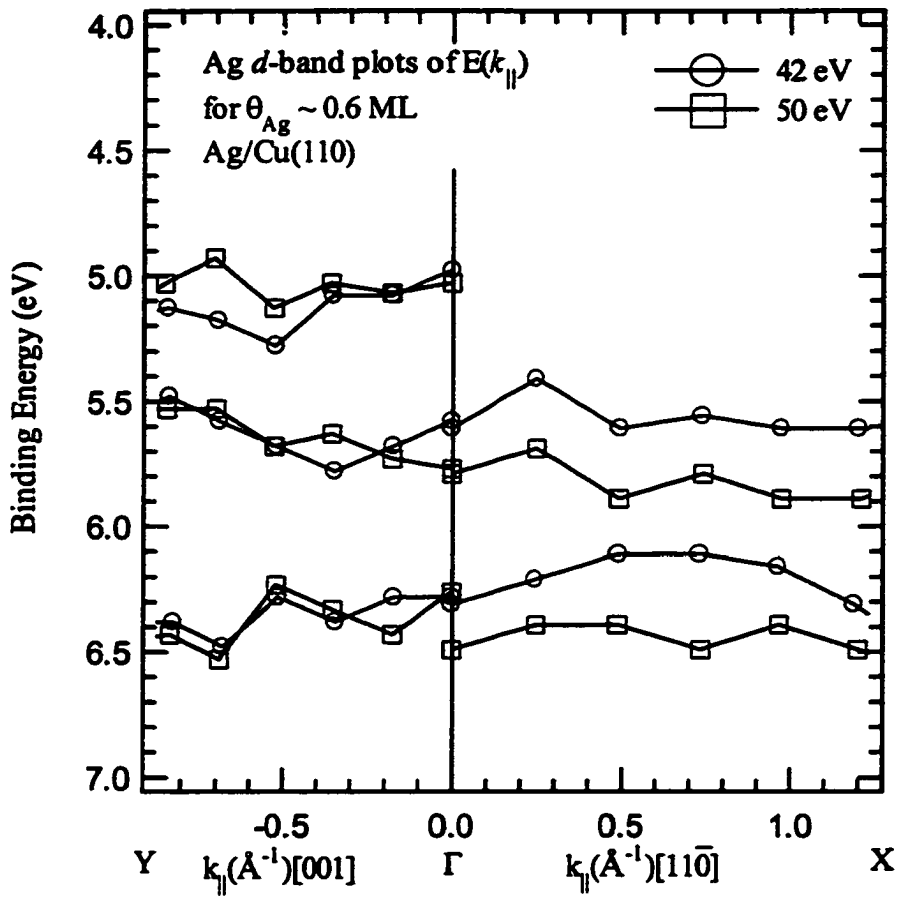

Figure 20. Band map of the Ag *d*-bands for 0.6 ML of Ag/Cu(110) along the high symmetry directions in the surface Brillouin zone.

energies (42 eV and 50 eV). It can be seen from this plot that the Ag *d*-bands behave quite differently along the chains as opposed to perpendicular to the chains. For these data, it is determined that these chains have a one-dimensional behavior along the chain, whereas a two-dimensional electronic structure is observed perpendicular to the chains. This displays the dominant Ag-Ag interaction along the chain and a Ag-Cu interaction perpendicular to the chain due to hybridization with the bulk-like Bloch waves of the substrate.

In the following chapter, the description and analysis of the surface morphology and electronic structure of Ag/Ni(110) is detailed where the similarities to the Ag/Cu(110) system will be pointed out. One of the crucial differences between Ag/Cu(110) and Ag/Ni(110) is that in the case of Ag/Ni(110) the symmetry of the substrate is retained. The similarities are *sp-d* hybridization and three-dimensional electronic structure, a trend common to all metal-on-metal systems discussed in this dissertation. This is due to negligible *d*-band overlap and increased coordination from being incorporated into the substrate in surface alloy formation and, in the case of Ni/Ag(100), subsurface growth.

Chapter Four

Ag/Ni(110)

4.1 Introduction/Background

The heteroepitaxy of Ag on Ni(110) is another example of a bulk-immiscible system that exhibits surface alloy formation for coverages less that one monolayer. The Ag-Ni system is characterized by a large miscibility gap in the bulk phase diagram as well as a large lattice mismatch (16%). Based on the simple thermodynamics arguments outlined in Chapter One, one would expect the first monolayer of Ag to completely "wet" the Ni substrate, because the surface free energy of Ag (γ_{Ag} = 1.3 J/m^2) is significantly lower than that of Ni (γ_{Ni} = 1.9 J/m^2). This does seem to be the case for Ag deposition on the (100) and (111) faces of Ni, however for the open (110) surface, a well-ordered surface alloy is formed [29].

Room temperature deposition of Ag on Ni(110) forms a (10 × 1) string structure for coverages between 0.5-0.8 ML. In this high Ag-concentration, alloyed phase, the Ag atoms are locally clustered along the [001]-direction, very similar to the Ag/Cu(110) system previously described. In contrast to the Ag/Cu(110) system,

however, in this case, the Ag atoms are held pseudomorphically to the Ni lattice. The excess strain resulting from this lattice registry is accommodated through an outward buckling, giving rise to this (10 × 1) string structure. Electronically, this gives rise to a three-dimensional structure.

In contrast to the surface alloy phase, the morphology and electronic structure resulting from additional deposition (θ_{Ag} ~ 1 ML) is fundamentally different. Atomically, this structure is that of a two dimensional, hexagonal overlayer. With respect to the underlying lattice, this overlayer has a c(2 × 4) superstructure. For this overlayer phase, the resultant electronic structure exhibits a truly two-dimensional nature, behaving like a two-dimensional analog of Ag(111). This hexagonal overlayer phase is very similar to the overlayer films of Ag on Ni(100) and Ni(111), investigated by Shapiro *et al.* [39].

Many different systems that exhibit Ag(111) monolayer growth have been studied by Shapiro *et al.* [40]. In general, their studies were focused on the effects of the various substrates on the electronic structure of virtually identical hexagonal monolayers of Ag. The substrates used in their studies were Ni(111), Ni(100), Cu(111) and Cu(100), among others. Their findings show that the overlayer electronic properties are very similar despite the large differences in the electronic and atomic structures of the substrates. Apparently, the differences in the substrate crystal potential as seen by the overlayer are essentially averaged out, except for an overall shift in energy. For example, between the Ni and Cu substrate, there is a 0.32 eV rigid offset. Although Shapiro *et al.* find this result surprising because "the overlayer-substrate bonding is strong" [39], this result seems quite reasonable

because the two-dimensional nature of the overlayer, both atomically and electronically, implies a relatively *weak* bonding between the overlayer and substrate, especially when compared to the highly coordinated nature of the surface alloy phase, where the bonding must be much stronger. With that point aside, Shapiro *et al.* liken the invariant electronic structure of Ag monolayers to the relationship between crystalline and amorphous materials, where the densities of states are similar despite the large differences in symmetry [41]. In their discussion they raise the question of the role and relative importance of *s*, *p*, and *d* electrons in the bonding and coupling between the overlayer and the substrate. This is precisely the question that is attempted to be answered in this study of Ag/Ni(110).

4.2 Surface Morphology of Ag/Ni(110)

The only work conducted on Ag/Ni(110) in the literature is that performed by Sprunger *et al.*, which is described in detail here. In the initial stages of growth (~ 0.2 ML), the resultant morphology is that of monatomic height Ni islands on the terraces, with a one-to-one density equal to the Ag coverage, as determined by Rutherford backscattering (RBS). These islands are formed by the Ni atoms expelled during the substitutional alloy mechanism. Their atomically resolved STM images reveal a pseudomorphic surface-alloyed structure between the islands, which have heights characteristic of the Ni monatomic step [29].

At slightly higher coverages (~0.3 ML), a different structural phase begins to develop. As in the case of Ag/Cu(110), due to the anisotropic nature of the (110) surface, alloyed Ag atoms tend to locally cluster along the [001]-direction of the Ag-Ni surface, due to the increased local compressive strain introduced by incorporation

of the larger Ag atoms in the substrate. This effect is identified more easily as the coverage is increased even higher (0.5-0.8 ML). In this coverage regime, the strain-relieving buckling locks into a superperiodicity giving rise to the characteristic (10 × 1) LEED pattern. As can be seen from Fig. 21, this buckling forms a periodic arrangement with a separation of ten Ni $[1\bar{1}0]$ units and an oscillatory amplitude of ~ 0.4 Å. Atomically resolved images of this anisotropically buckled structure (Fig. 22) indicate that the Ag atoms are held pseudomorphically in registry to the underlying substrate. Although similar in some respects, this structure is fundamentally different from that seen in the Ag/Cu(110) system, which becomes apparent in the electronic structure studies outlined below.

As mentioned above, monolayer deposition of Ag on Ni(110) results in hexagonal overlayer formation on an un-alloyed Ni substrate, virtually identical to those formed on numerous other substrates including Ni(100), Ni(111), Cu(100), Cu(110), and Cu(111) [30-33, 40]. With respect to the underlying (110) substrate, this formation gives rise to a c(2 × 4) superstructure, where the hexagonal overlayer is commensurate to the Ni near neighbor distance along the $[1\bar{1}0]$-direction and incommensurate along the [001]-direction (Fig. 23). The Ag hexagonal overlayer is subjected to a 0.6% contraction along the $[1\bar{1}0]$-direction and a corresponding 0.6% dilation along the [001]-direction, whereby the areal density of the Ag(111) surface net is conserved. Therefore, this requires not exactly 1 ML of Ag to cover the surface, but ~ 1.2 - 1.3 ML, a coverage consistent with those measured by RBS [42]. An STM image of this overlayer is shown in Fig. 24, where the superstructure is seen to exhibit the c(2 × 4) pattern. Ag atoms are seen to alternate from bridge sites

Figure 21. STM image of 0.8 ML of Ag/Ni(110). Large scale morphology of (10 × 1) superperiodicity (1000 Å × 1000 Å) (from Ref. [29]).

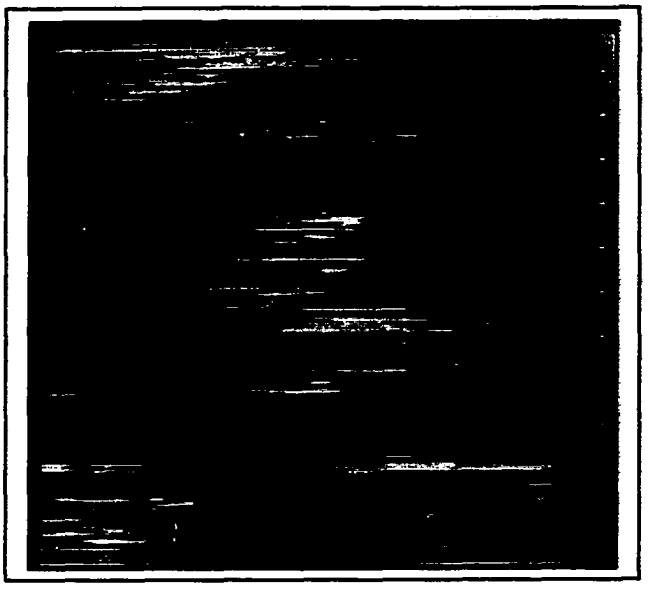

Figure 22. Atomically resolved image of Ag/Ni(110) showing the pseudomorphic registry to the underlying lattice. Image size is 50 Å × 50 Å (from Ref. [29]).

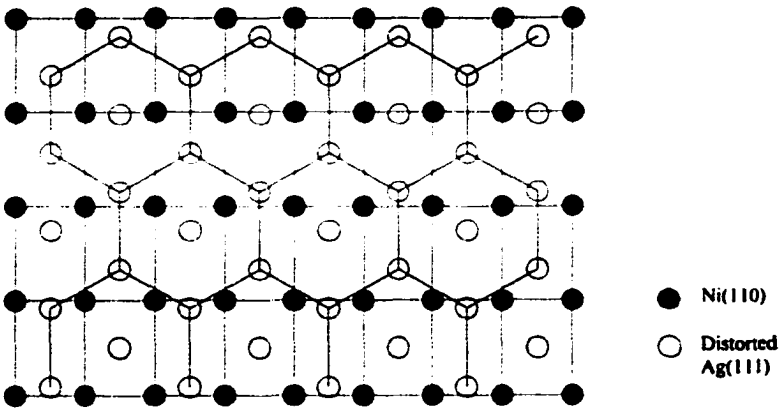

Figure 23. Ball and stick model showing the distorted hexagonal Ag overlayer on top of the Ni(110) surface net.

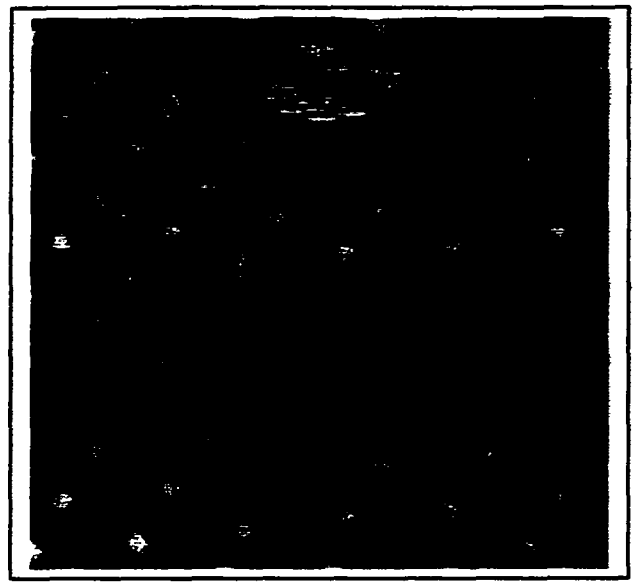

Figure 24. STM image of the c(2 × 4) hexagonal overlayer of 1.3 ML of Ag/Ni(110). Image size is 50 Å × 50 Å (from Ref. [42]).

(brighter) to hollow sites (darker) in the incommensurate superstructure. As will be shown below, these two strikingly different morphologies of the surface alloy and the hexagonal overlayer result in correspondingly different electronic structures, which provide for useful insight into the various bonding for different atomic structures.

4.3 Electronic Structure of Ag/Ni(110): Results and Discussion

The angle-resolved photoemission spectroscopy experiments were performed in the winter of 1999 at CAMD. The Ni(110) crystal was mechanically polished using successively smaller grade diamond paste and subsequently etched in an acid solution comprised of 65 mL of Acetic acid (CH_3COOH, 100%), 0.1-0.3 mL of Hydrochloric acid (HCl, 37%) and 35 mL of Nitric acid (HNO_3, 65%). This solution removes approximately 1 μm per minute at 21 °C. This polish is repeated until scratches and other observable blemishes are gone. The polishing effect of this mixture decreases after ~ 5-10 minutes, therefore it should only be used to polish one crystal per mixture. As is typical for metal substrates, after being introduced into the vacuum chamber, the Ni crystal was cleaned by repeated cycles of ion sputtering using Ne^+ at 1 keV and 15 mA emission current, followed by annealing to 925 K. In these experiments annealing was facilitated by resistive heating using an AC current source (Varian TSP controller) and monitored by a type-K thermocouple mounted directly to the side of the crystal. The crystal was then rotated to align the crystallographic mirror planes with the polarization of the incident radiation, using LEED.

Measurements were made using *p*-polarized light with three different angles of incidence, α = 25°, 45°, and 60°. In order to distinguish between Σ_1 and Σ_4 (Σ_3) bands, the angle of incidence is increased, thereby identifying the states of Σ_1 symmetry with increasing intensity [43]. Varying the angle of incidence not only identifies the symmetry character of given states through enhanced intensity, but also allows for a higher sense of resolution in determining the energies of highly convoluted peaks in the photoemission spectra. Photoelectrons were collected from the two mirror planes of the Ni(110) crystal, i.e. the (001) and the $(1\bar{1}0)$ mirror planes. Due to the growth structure of the hexagonal overlayer phase, these crystallographic mirror planes of the Ni(110) are also mirror planes of the Ag(111) monolayer. In other words, the Ag(111) monolayer growth is such that $\bar{\Gamma}\bar{X}_{Ni} \parallel \bar{\Gamma}\bar{M}_{Ag}$ and $\bar{\Gamma}\bar{Y}_{Ni} \parallel \bar{\Gamma}\bar{K}_{Ag}$.

In this experiment, Ag deposition was achieved by resistive evaporation using a Ta filament. The deposition rate was typically around 0.01 ML/sec as determined by a quartz crystal microbalance. This evaporation rate was also cross calibrated using the development of LEED patterns as a function of coverage as determined in the atomic structure STM studies.

As in the case of Ag/Cu(110), where the bands of the substrate are shown to disperse differently from those of the clean substrate due to Ag *sp* - Cu *d* hybridization, the Ni *d*-bands likewise exhibit a similar redistribution of charge upon deposition of Ag, however unlike Ag/Cu(110), here the symmetry is retained due to the pseudomorphic growth. Figures 25 (a) and (b) show the shifting of the Σ_3 and Σ_4 Ni *d*-bands, respectively. Here the Ni *d*-bands are seen with binding energies

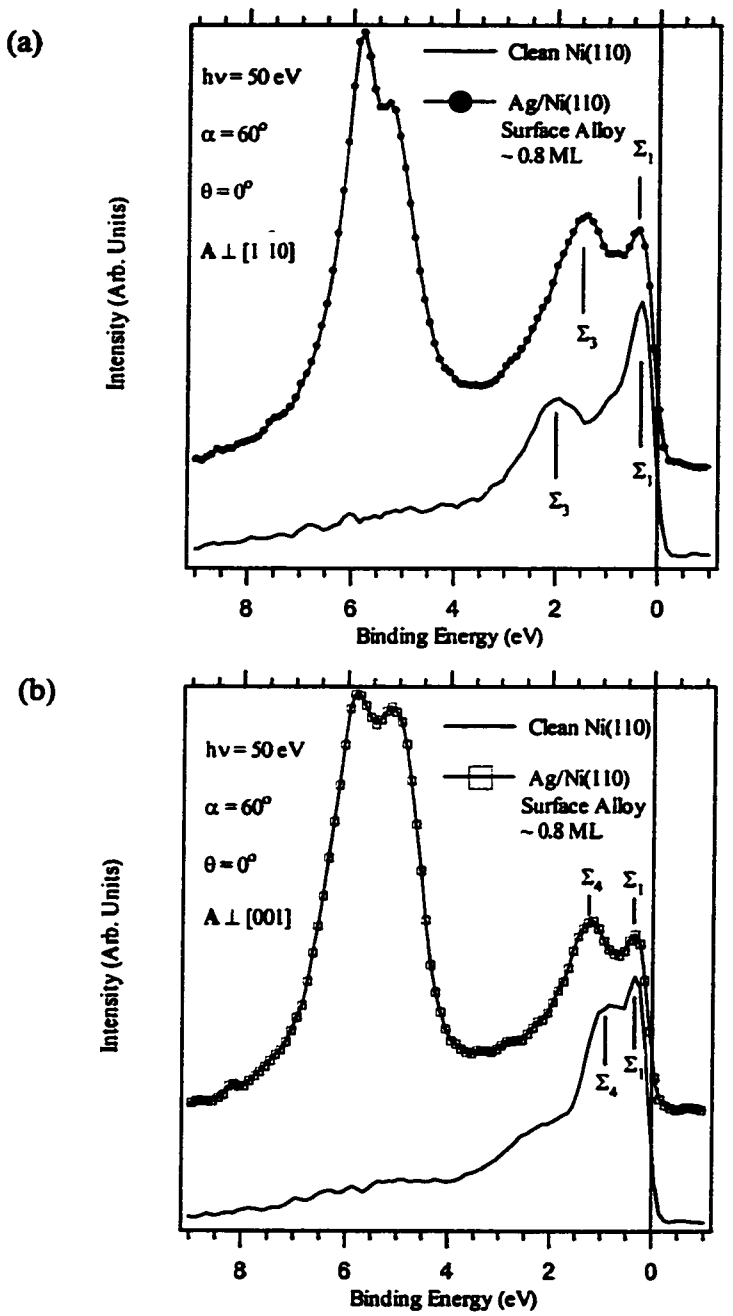

Figure 25. EDCs of clean Ni(110) (curves without symbols) and Ag/Ni(110) with a coverage of 0.8 ML. (a) Ni Σ_3 band is shifted to lower binding energy by 0.5 eV (b) Ni Σ_4 band is shifted to higher binding energy by 0.25 eV.

between ~ 0-3 eV, while the Ag *d*-bands are seen between ~ 4-7 eV. In these figures, EDCs of both the clean Ni(110) and the surface alloy phase of Ag/Ni(110) are displayed for the two geometries so that the different symmetry representations are shown. For this particular slice through the Brillouin zone, the Σ_3 band of Ni is shifted to lower binding energy by ~ 0.5 eV, whereas the Σ_4 band is shifted to higher binding energy by ~ 0.25 eV. According to band structure calculations of bulk Ni and bulk Ag, this region in the Brillouin zone, which these spectra represent, is precisely the region in which the Ag *sp*-band intersects with the Ni *d*-bands, suggestive of the dominant bonding mechanism for this case.

The dimensionality of this Ag/Ni(110) system is analyzed in the same way as that of the Ag/Cu(110) detailed in Chapter 3. The highly coordinated nature of the Ag atoms in the surface alloy phase results in a quasi-three-dimensional electronic structure displayed in the Ag *d*-band. Figure 26 shows a representative set of EDCs, where it can be immediately seen how the Ag *d*-bands disperse strongly as a function of photon energy. The other, necessary condition for three-dimensionality is that these bands disperse in the plane of the surface (as a function of $k_{||}$), albeit differently for different photon energies, i.e. for different values of $k_{\perp}$.

Figure 27 is a band map of the Ag *d*-band throughout the surface Brillouin zone, along the high symmetry directions. Along both directions, $\overline{\Gamma}-\overline{X}$ and $\overline{\Gamma}-\overline{Y}$, the Ag *d*-bands are shown to disperse in the (110) plane. Moreover, this dispersion is different for various photon energies. This quasi-three-dimensional electronic structure exhibited by the *d*-bands of Ag is the result of hybridization between the Ni *sp*- and Ag *d*-bands due to a large overlap in wave functions. This is consequently a

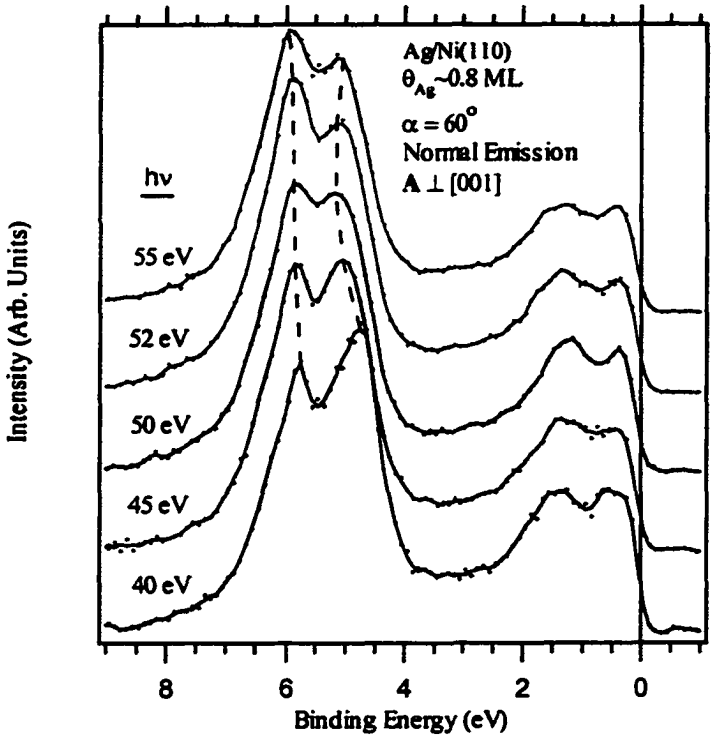

Figure 26. EDCs of 0.8 ML of Ag/Ni(110) collected at normal emission for various photon energies.

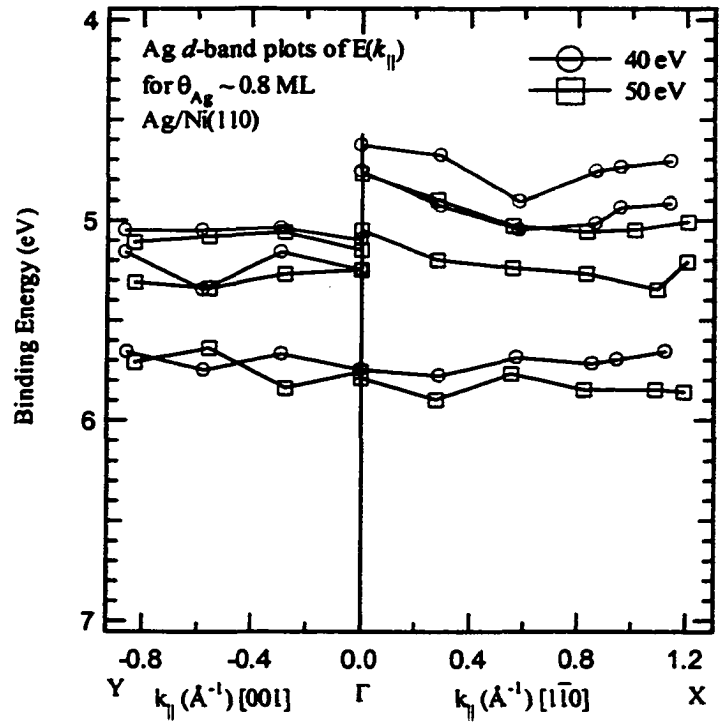

Figure 27. Band map of the Ag *d*-bands for 0.8 ML of Ag/Ni(110) along the high symmetry directions in the surface Brillouin zone.

result of the increased coordination of the alloyed Ag atoms, thereby allowing for a strong coupling to the Bloch waves perpendicular to the surface. This may seem to be a rather unique phenomenon, since the Ag atoms are strictly confined to the two-dimensions of the surface layer, but as more and more systems are studied that exhibit intermixing in the surface, it is believed that the bulk-like electronic structure of surface-confined systems is more the trend than the exception.

In contrast to the surface alloy phase, the Ag *d*-bands in the hexagonal overlayer phase exhibit a characteristic two-dimensional electronic structure. As the Ag atoms have become completely de-alloyed from the surface, due to excess strain energy in the alloy, they have essentially become electronically decoupled from the bulk. There must be some weak coupling to the substrate, but the dominant interaction involving the Ag *d*-bands must be the in-plane Ag-Ag interaction. EDCs for the overlayer phase are shown in Fig.28, where the conditions are identical to that in Fig. 26, the analogous photoemission conditions for the surface alloy phase. From Fig. 28, it is obvious that the Ag *d*-bands are negligibly dependent on the perpendicular component of the wave vector. As mentioned above, this is not enough to show two-dimensionality. Again, it is necessary to show dispersion in the plane. Fig. 29 is a band plot mapping the binding energy versus the perpendicular component of the wave vector along two of the high symmetry lines of the surface Brillouin zone, this time now for the hexagonal monolayer, i.e. along $\overline{\Gamma K}$ and $\overline{\Gamma M}$. The point here is that even though the Ag *d*-bands show dispersion as a function of $k_{\parallel}$, they do so virtually independent of $k_{\perp}$. Therefore, not only do these data imply conclusions regarding the dimensionality of the hexagonal overlayer, but it can also

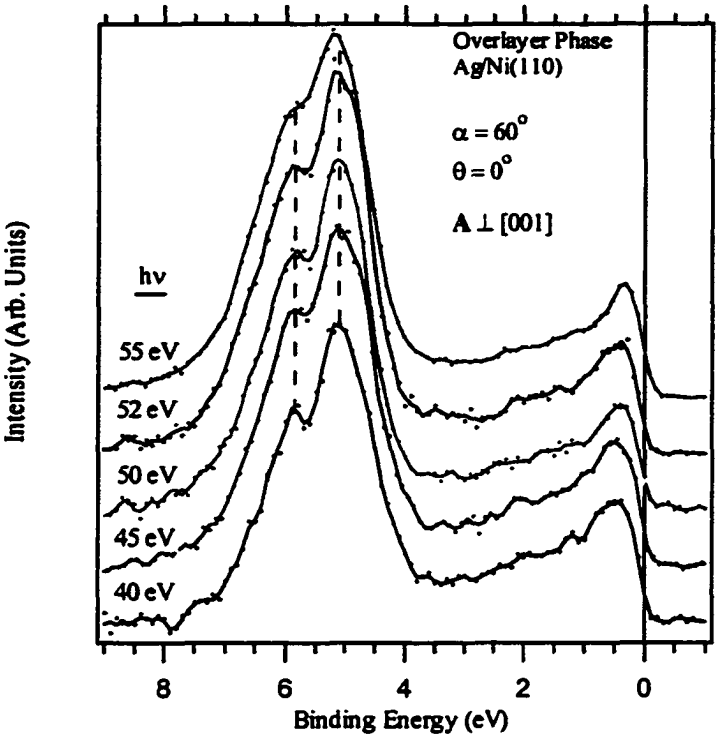

Figure 28. EDCs of 1.3 ML of Ag/Ni(110) collected at normal emission for various photon energies.

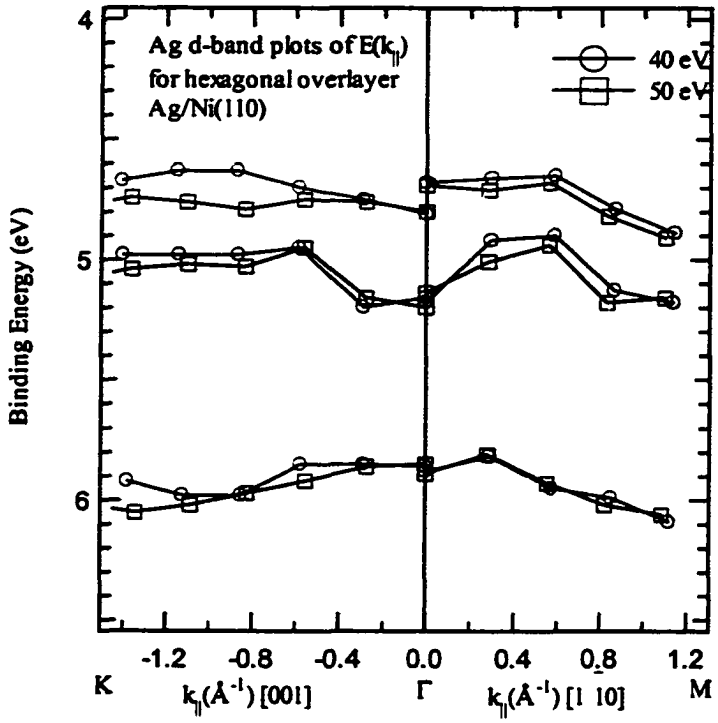

Figure 29. Band map of the Ag *d*-bands of the hexagonal overlayer of Ag/Ni(110) along the high symmetry directions in the surface Brillouin zone.

be inferred that the Ag *d*-bands are not playing an active role in the bonding mechanism between the overlayer and the substrate. This implies that Ag *sp*-states must have an active role in the interfacial bonding. This is a reasonable conjecture due to the de-localized nature of the *sp*-band.

In the case of the surface alloy, it was shown that 1) the Ag *d*-bands have a quasi-three-dimensional electronic structure and 2) Ni *d*-bands undergo energetic shifts in the interfacial region. The overlayer phase exhibits a characteristic two-dimensional structure, while the Ni *d*-bands are essentially equivalent to the unmodified bands of the substrate apart from reduced intensities due to the mean free path of those photoelectrons that originate from one layer beneath the Ag hexagonal overlayer. Unlike the Ni(100) and Ni(111) substrates, the surface alloy phase occurring on the Ni(110) provides for a contrasting case with which to compare the degree of interaction between adatoms and substrate for the two radically different surface morphologies.

Chapter Five

Ni/Ag(100)

5.1 Introduction/Background

In a discussion concerning the formation of bulk-immiscible surface-confined alloys, J. Tersoff used, as his generic example the Au/Ni(100) system. The model from which he explained his preferential alloying results was based solely on strain energies, where he used a pair-wise interaction between neighboring atoms given by

$$E = \alpha \sum_{ij} \left(r_{ij}^2 - b_i b_j \right)^2 , \qquad \text{(Eq. 16)}$$

where α is the bond stiffness, r_{ij} is the distance between atoms i and j, and b_i is the preferred bond length of atom i. The summation is restricted to nearest-neighbor pairs [44]. In passing, Tersoff mentioned that his calculations do not show a significantly different result when the complementary system is studied, (i.e. Ni/Au(100)). He goes on to point out that any asymmetry in growth by switching adlayer and substrate species, must be due to factors other than those solely dependent on strain. In this chapter, the results of atomic and electronic structure

studies are detailed for the Ni/Ag(100) system, the complement to the Ag/Ni(110) system discussed in the previous chapter.

In stark contrast to the Ag/Ni(110) system, the growth morphology of submonolayer coverages of Ni on Ag(100) exhibits a nano-clustered morphology of Ni precipitates. This growth mode is predicted by Young's equation (Chapter 1, eq. 1), where due to the relative surface free energies of the adatoms and the substrate, a three-dimensional growth mode is expected.

The Ni/Ag(100) system has been the subject of numerous theoretical and experimental studies. Originally, this system was used as a model system for studying the magnetic properties of ultrathin Ni layers. Thompson *et al.* found relatively small exchange splitting of the 3*d* band using ARPES [45]. Hong *et al.*, trying to justify the results of Thompson, suggested that the reduction in the magnetic moment of the Ni film might be due to subsurface growth of Ni [46]. Due to the fact that the surface free energy of Ni (γ_{Ni} = 1.9 J/m^2) is much larger than that of Ag (γ_{Ag} = 1.3 J/m^2) [47], the propensity for subsurface growth of Ni is predicted, assuming a small interfacial energy. Based on this, theoretical studies emerged which investigated the propensity of subsurface growth in the Ni/Ag(100) system [12-16]. Bolding and Carter, using Monte Carlo simulations, first discussed the clustering of the Ni overlayer at submonolayer coverages, and observed a propensity for the Ni/Ag system to form a Ag/Ni/Ag(100) sandwich structure. This sandwich structure was found to be thermodynamically favored over a tetragonal Ni(100) overlayer, a metastable structure due to an expansive intralayer strain inducing a compressive interlayer stress [12]. The team of Legrand and Tréglia, then,

investigated the subsurface "surfactant-like" growth of Ni on Ag(100) using a kinetic tight-binding Ising model [13-15]. Their results indicate that annealing the Ni film deposited on a Ag substrate should lead to a "floating" bi-layer staying above the buried Ni deposit. Based on LEED intensity versus voltage data, Lee *et al.* concluded that Ag atoms do migrate to the surface, covering the deposited Ni. Their conclusions though are different from earlier theoretical studies because they report that the subsurface growth of Ni does not occur as a layered structure, but rather in subsurface islands or clusters [48]. In a more recent work by Roussel *et al.*, they expect that a critical deposit size should give rise to clustering in the thin deposit case and then to planar interfaces in a thick deposit case [16].

Here evidence is given, based on STM data, that subsurface growth occurs and that Ni clusters form within the Ag(100) host, both at room temperature and, to a higher degree, upon annealing to 420 K. ARPES data are also presented for Ni/Ag(100) deposited at 130 K, wherein surface alloying is suppressed. After annealing to 420 K, the subsurface segregated phase is promoted. It will be shown that Ni nanoclusters form on the Ag(100) surface with some Ni segregating subsurface even at room temperature. Upon annealing, virtually all Ni segregates beneath the surface in the form of nanoclusters. The electronic structure of the unannealed Ni clusters behaves quasi one-dimensionally as a result of confinement and that of the annealed system behaves like a three-dimensional system as a result of the Ni *d* - Ag *sp* hybridization and increased coordination. These combined, atomic and electronic structure studies allow for a particularly nice insight into the interplay between growth morphology and electronic mixing of states in heteroepitaxy.

5.2 Surface Morphology of Ni/Ag(100)

The scanning tunneling microscopy experiments were conducted in the summer of 1999 at Oak Ridge National Laboratory. The STM used was an Omicron room temperature Scanning Probe Microscope (SPM II). The Ag(100) crystal was cleaned by repeated cycles of ion sputtering using Ne^+ and subsequent annealing to 775 K using an electron bombardment type heater filament positioned behind the sample. In these experiments, the Ni deposition was achieved by a small *e*-beam evaporator equipped with a flux monitor, H_2O cooling and a manual shutter. The typical deposition rate was estimated by the STM observations to be 0.003 ML/sec, with evaporator conditions of 700 V bias and 37 mA emission (2.1 A). The STM was operated in constant-current mode with typical tunneling conditions of 0.2-0.5 nA and sample bias of up to 1.0 V.

Typical STM images of the Ag(100) surface after deposition of ~ 0.5 ML Ni at room temperature and after annealing to 420 K are shown in Fig. 30 (a) and (b), respectively. Deposition at room temperature results in formation of Ni clusters randomly distributed throughout Ag(100) terraces. In addition, Ag monatomic steps are seen in the lower-left and upper-right of the 500×500 $Å^2$ STM image (Fig. 30(a)). The average measured lateral diameter of these clusters is 20 - 30 Å and their heights are ~ 2 - 5 Å. This result is consistent with a previously reported observation [49]. However, we also observe that a small fraction of Ni islands protrude from the surface with a height of only 0.5 - 1.5 Å, which is below a monatomic step height. Correspondingly, these islands have lateral extensions of only ~ 10 Å. As described in detail below, this implies that some of the Ni islands have been partially or totally

(a)

(b)

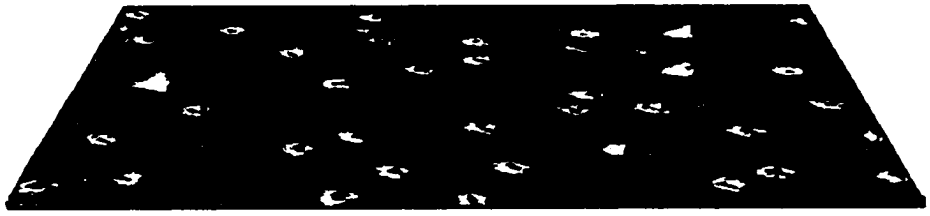

Figure 30. STM images of Ni/Ag(100) (a) as deposited at room temperature and (b) after annealing to 420 K. The Ni clusters in (a) have a lateral width of ~ 30 Å and heights between 2-5 Å. Fig. 27 (b) shows the subsurface morphology where the height of the islands are ~ 0.5 Å. Each image is 500 Å × 500 Å.

covered by Ag atoms even at room temperature. The fraction of the surface covered by these clusters is 0.35, which is in stark contrast to what is observed after annealing the sample.

As seen in Fig. 30 (b), the dramatic changes in surface morphology are observed after annealing the sample. The most obvious change is the radical reduction in the fraction of surface covered by apparent Ni clusters, from 0.35 to 0.10. Even though the lateral extension of these clusters is still ~30 Å, the heights of these islands are only 0.2 - 0.5 Å. Approximately 10% of the observed clusters retain the shape of the unannealed islands; however, they are not observed with the previous heights of 2 - 5 Å but are consistently ~ 1.5 Å. As seen in the STM image, the vast majority of islands have volcano-type topography, i.e. with a depression in the middle of the cluster. Because atomic resolution was not achieved, it is not known what local structure covers these embedded clusters; however, the observed sharp 1x1-Ag(100) LEED pattern indicates a non-reconstructed surface. Moreover, STM results also revealed that subsequent exposure to large amounts of oxygen (~100 L, 1L = 1 Langmuir = 10^{-6} Torr·sec) resulted in no apparent oxidation of the annealed surface. In other words, the Ni/Ag surface has become chemically dead to reactive chemisorbed species such as oxygen. This indicates that, due to the small sticking probability of oxygen on Ag (~10^{-4}) as compared to Ni (~ 1), the Ni clusters are buried beneath at least one layer of Ag.

At room temperature, STM reveals that the majority of Ni remains in clusters on top of the Ag(100) surface. However, upon annealing, the density of islands present is reduced by a factor of 3. This observation cannot be due to a 2-D Oswald ripening effect because the observed lateral size of these islands remains the same

while the average height decreases by tenfold. This reduction in the density of islands could be accounted for if a critical concentration of Ni is substitutionally alloyed into the Ag, above which Ni clustering results. Because atomic resolution was not attained with this STM, this argument is inconclusive. Another way to account for the dramatic decrease in island density upon annealing is subsurface Ni nanoclustering. Comparing the areal density of islands before and after annealing suggests that embedded Ni clusters have a perpendicular height above one monolayer. Tentatively, an approximate bi-layer Ni embedded subsurface cluster morphology is consistent with the STM data.

This type of "buried" growth morphology has been identified in other systems [50, 9-11]. The driving force for this mechanism arises from the competition of a number of factors including the surface free energies, the interfacial energy, and the segregation/mixing energy. In the present system, the large difference in the surface energy between Ag and Ni appears to dictate the overall growth morphology. That is, this difference is large enough to compensate the ensuing interfacial energy caused by the strain at the interface between Ag and the embedded Ni. Although the composite energy of the system is minimized by the formation of embedded nanoclusters, this is an activated process. Upon annealing the system, the exchange energy barrier to the subsequent segregation is thermally overcome.

5.3 Electronic Structure of Ni/Ag(100): Results and Discussion

The angle-resolved photoemission spectroscopy experiments were conducted in the summer of 1998 at CAMD. In addition to using the PGM beamline, data were

also collected using an un-polarized source of ultraviolet radiation from a He(I) discharge lamp. For this part of the study, the Ag(100) crystal was cleaned per the usual repeated cycles of ion sputtering and annealing, however the sample heating was facilitated by resistive means. The Ni was vapor deposited using two different methods. One method entailed passing a current through a Ta filament around which small rings of Ni wire were wound, while in the second method, current was simply passed directly through a Ni wire (∅ 0.5 mm). Both methods work equally well, but the second method described is substantially easier. In the ARPES experiment, Ni was deposited on the Ag(100) substrate at ~130 K, to suppress subsurface growth, which occurs near room temperature, and then subsequently annealed to 420 K. The photoemission geometry was such that *p*-polarized light was used with an angle of incidence of 45° and the vector potential perpendicular to the $[0\bar{1}1]$-direction of the Ag(100) crystal. For off-normal emission, the electron analyzer was rotated within the $(0\bar{1}1)$ plane. During these photoemission experiments, the growth was monitored using LEED. The LEED observations correspond to the random distribution of Ni nano-clusters by displaying a completely diffuse LEED pattern with no diffraction spots visible (Fig 31(a)). After annealing to 420 K, LEED observations show the re-emergence of a sharp 1 × 1 Ag(100) diffraction pattern (Fig. 31(b)).

The electronic structure for this system is now discussed in light of the morphological results. In general, the dependence of energy bands based on photon energy at normal emission gives $k_{\perp}$ information, and off angle emission spectra gives $k_{\parallel}$ information. From photoemission results, much is learned about the

(a)

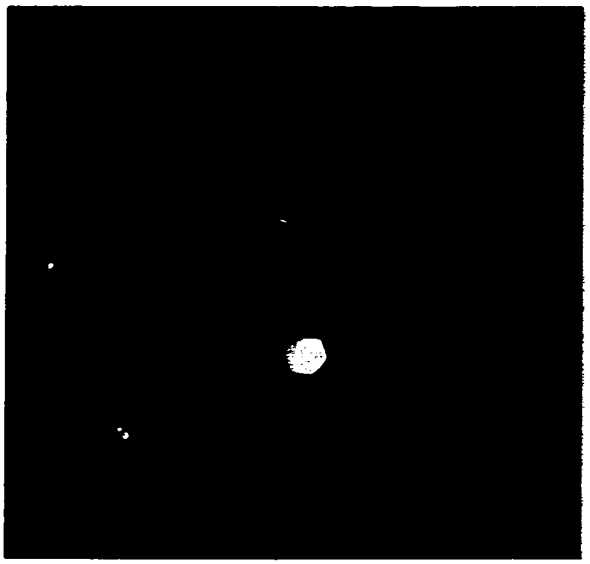

(b)

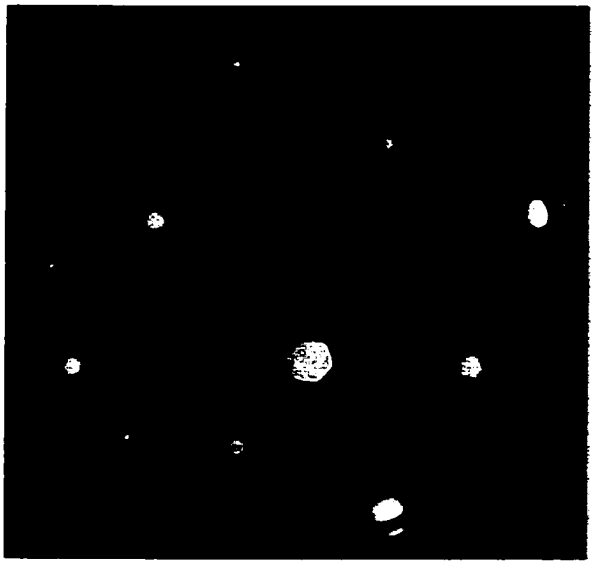

Figure 31. LEED patterns for two conditions of Ni/Ag(100). (a) Ni deposited at room temperature. (b) Ni/Ag(100) has been annealed to 420 K.

dimensionality of surface structure as well as insight into the nature of hybridization between the two different types of atoms. For example, Ni and Ag are two very different metals wherein the energetic overlap between the *d*-bands is negligible. The most obvious evidence from photoemission data that Ni segregates into the subsurface is based solely on intensity arguments of photoemission peaks before and after annealing. By considering EDCs in Figures 32 and 33, the dramatic reduction in intensity of the Ni *d*-bands (~0 - 2 eV), relative to Ag *d*-bands (~4 - 7 eV), is obvious upon annealing the sample. Moreover, evolution of the Ag *d*-bands, from clean Ag(100) to Ni deposited at ~ 130 K to the annealed Ni/Ag(100), shows almost a total recovery of the clean Ag electronic structure upon annealing (dotted curves in Fig. 32(a) and 33(a) are clean Ag(100) at $h\nu = 40$ eV). This corresponds very well with STM images of the annealed surface where large areas of clean Ag between embedded Ni clusters reemerge on the surface. Because annealing temperatures used here are well below the desorption temperature of Ni from the surface, the observed Ni-to-Ag *d*-band intensity ratio can be used to conclude that the preferred growth mode for this system is Ni subsurface clustering. As outlined above, this idea is in complete agreement with the STM data.

EDCs for the unannealed Ni/Ag(100) system as a function of photon energy at normal emission are shown in Fig.32(a). Dispersion of bands as a function of $k_\perp$(varying photon energy at normal emission ($k_\parallel = 0$)) usually implies a three dimensional electronic structure. However, as seen below, the electronic structure of the unannealed surface lacks dispersion in the plane (i.e. with $k_\parallel$). The dispersion of the Ni *d*-bands with $k_\perp$, as seen in Fig. 32(a), appears to be very subtle, implying a

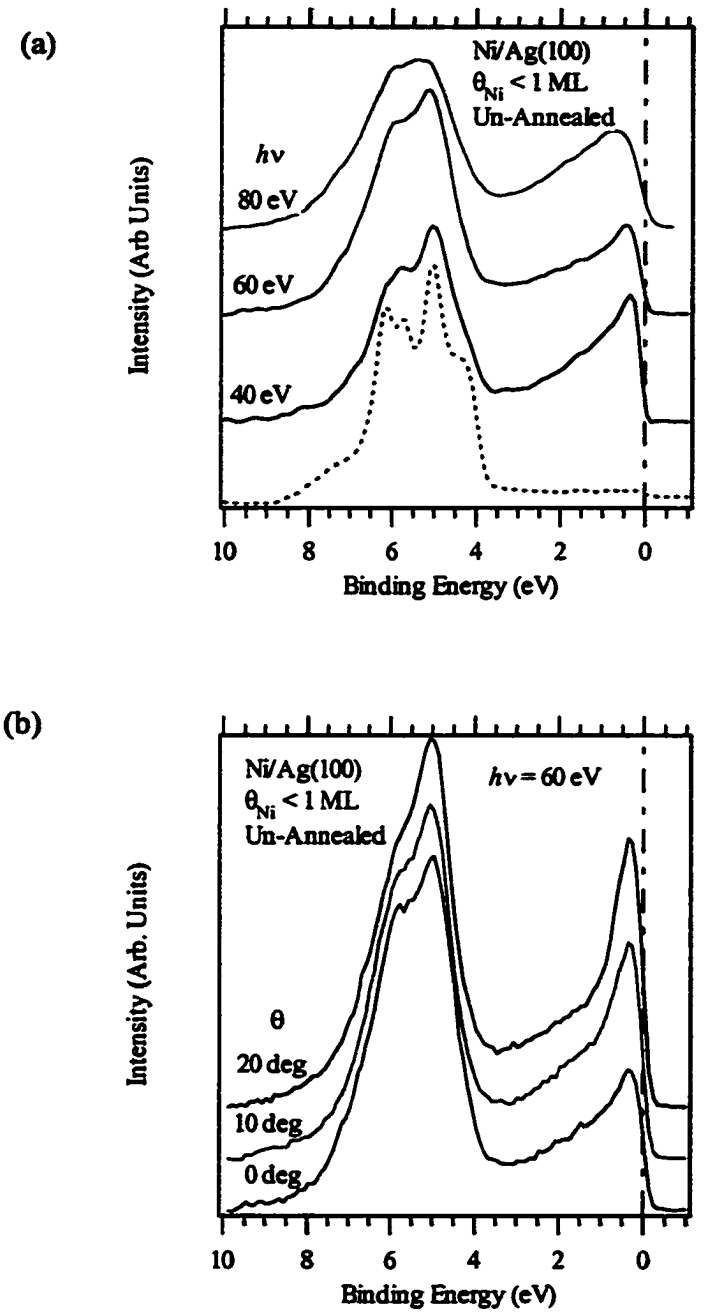

Figure 32. EDCs for the unannealed Ni/Ag(100) surface. (a) Dispersion with photon energy indicates energy dependence on $k_{\perp}$. (b) Lack of dispersion of Ni bands in the plane indicate a quasi-one-dimensional electronic structure

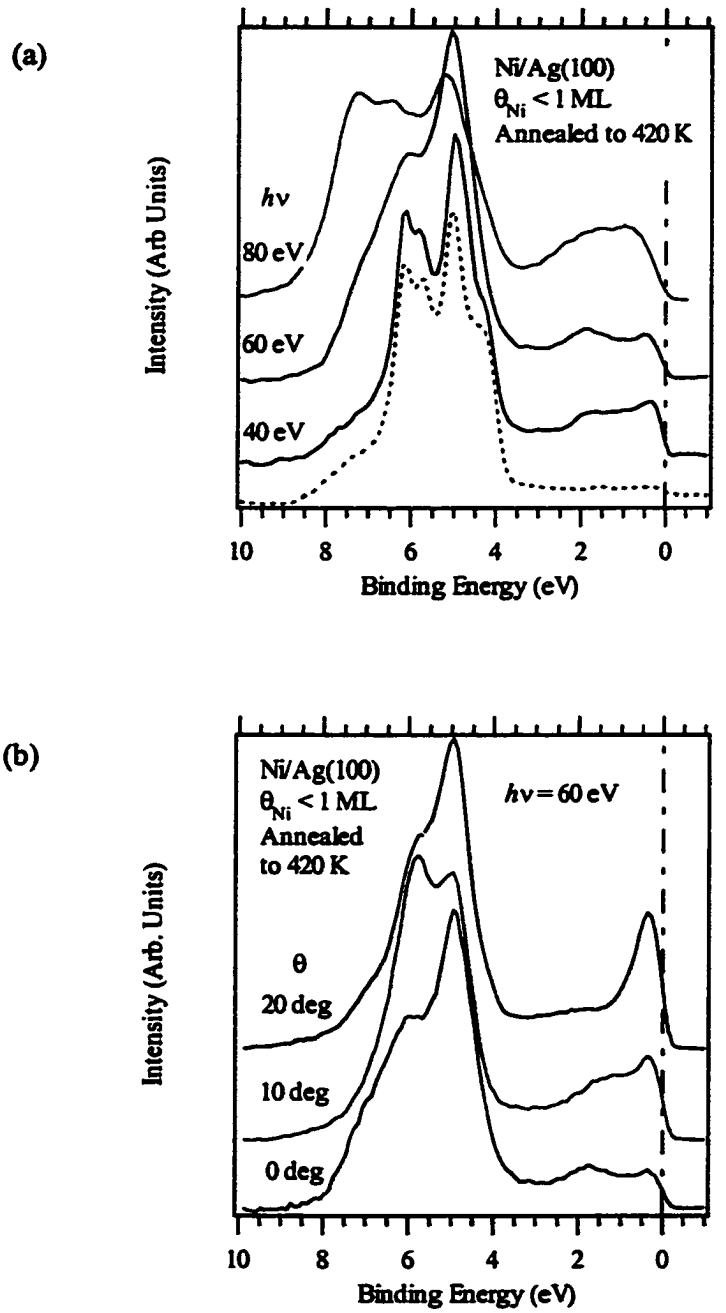

Figure 33. EDCs for the annealed Ni/Ag(100) surface. Dispersion with photon energy (a) as well as in the plane (b) indicate a three-dimensional electronic structure in the Ni *d*-bands.

weak bonding with the substrate. In order to confirm that the Ni *d*-bands do indeed disperse with $k_\perp$, EDCs at different photon energies with the same $k_\parallel$ away from the zone center have been compared. As seen in Fig. 34, there is a striking difference between the pairs of spectra taken at the same $k_\parallel$ but different $k_\perp$ points. This type of behavior can occur for a multi-layered cluster of Ni atoms on the surface; however, at coverages < 1 ML, it is thought that this 1-D electronic dispersion is due to the perpendicular bonding mechanism between these surface clusters and the substrate. It should also be noted that these changes in line shape could possibly be due to variations in photoemission cross section as a function of photon energy. The lack of resolution hinders the deconvolution of the individual Ni *d*-bands.

When dispersion of the Ni *d*-bands as a function of $k_\parallel$ for the unannealed surface (Fig 32(b)) is considered, it is found that the states are virtually dispersionless. This is a consequence of the fact that the lateral extent of Ni clusters is not great enough to establish the long-range periodicity required to form Bloch waves in the plane of the surface. This could also be explained if the Ni clusters are not well ordered. This latter suggestion is consistent with the observed diffuse and dim (1×1) LEED pattern of the unannealed surface.

EDCs for the annealed surface show a radically changed electronic structure. Figure 33 (a) shows the dispersion of Ni *d*-bands as a function of photon energy in normal emission geometry, and Fig. 33 (b) shows dispersion of these bands as a function of $k_\parallel$. From these EDCs it is concluded that in the case of the annealed surface, the electronic structure of the Ni nanoclusters behaves three-dimensionally because the bands disperse with $k_\parallel$ as well as with $k_\perp$. This conclusion corresponds

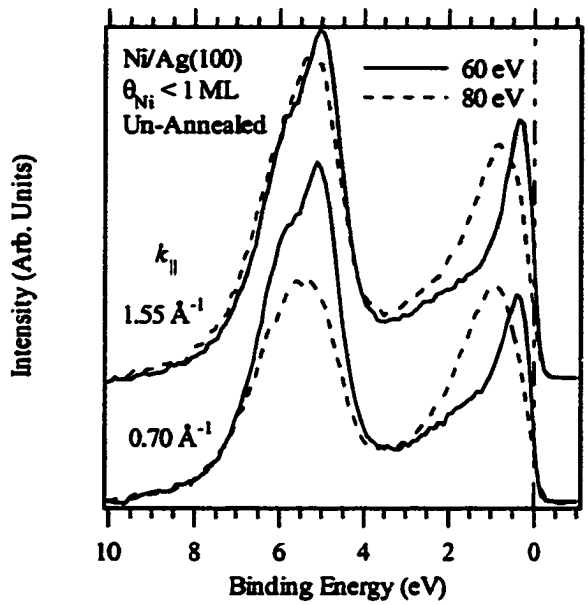

Figure 34. EDCs along $\overline{\Gamma}\overline{X}$ of Ni/Ag(100) for the unannealed surface. Each set of EDCs consists of two curves, which have different photon energies, but the same $k_{\parallel}$. This figure shows the dispersion of the Ni *d*-bands as a function of $k_{\perp}$ alone.

very well with the morphology of the annealed system as seen by STM. Since the Ni clusters are now buried subsurface within the substrate, not only are the states coupled to the bulk in the perpendicular direction, but also they are now allowed to match wavefunctions with the substrate in the lateral direction via hybridization mechanisms. This then establishes the lateral long-range periodicity with which to form Bloch waves parallel to the surface. This type of hybridization resulting in a three-dimensional electronic structure has been reported previously for the Ni/Cu(100) system [51], however the morphology is substantially different. The question naturally arises: What is the mechanism responsible for the coupling between the Ni and the Ag states?

Previous experimental reports of magnetically "dead" layers of ferromagnetic transition-metal surfaces [52] brought about numerous theoretical and experimental studies of surface magnetism over the years (e.g. Ref. 53-56, 46). Much of the original work focused on Ni layers on Cu surfaces. In the studies conducted by Wang *et al.*, it was concluded that these layers were not dead, and that the magnetic moment was reduced by 40 % compared to bulk Ni [54]. Tersoff and Falicov arrived at approximately the same result [53]. This was latter confirmed by Thompson and Erskine, with a measure of the exchange splitting using high resolution ARPES [55]. Thompson then reported a much smaller exchange splitting for Ni/Ag(100) [45]. This prompted Hong *et al.* to perform calculations that confirmed the small exchange splitting seen by Thompson; however, it was arrived at by assuming that the Ni segregated subsurface [46]. The main conclusion of this latter study was that the reduction in the magnetic moment of these Ni films is due to Ni *d* and Ag *s* hybridization, even though it is very weak. These are, by and large,

the same conclusions arrived at by Tersoff and Falicov. They stated that the suppression of Ni magnetization is due to increased *sp-d* hybridization when Ni atoms are adjacent to noble atoms, and enhancement of Ni magnetization is due to *d*-band narrowing and *sp-d* dehybridization at sites of low coordination [53].

Based on arguments by Tersoff and Falicov, on the morphology of surfaces as seen by STM, and on photoemission data, the following can be concluded about the electronic structure of Ni/Ag(100). For the case in which Ni is deposited at 130 K, alloy formation is believe negligible and Ni clusters form on the surface. Due to reduced coordination of these clusters, narrowing of Ni *d*-bands is observed as in Figs. 32(a) and 32(b). Hence there is a reduction in hybridization between Ni *d* and Ag *sp* bands. This may constitute a higher surface magnetism; however, the exchange splitting cannot be resolved for this case. In the case of the annealed surface, where Ni clusters have segregated subsurface and have a much higher coordination, the width of the *d*-bands is seen to be much larger (Figs 33(a) and 30(b)). This implies stronger *sp-d* hybridization between Ni and Ag bands. In this case, the surface magnetism should be considerably less. In conclusion, based on theoretical calculations and trends in our photoemission data, the primary mechanism for coupling between Ni and Ag states is Ni *d* - Ag *sp* hybridization.

In summary, STM results confirm that at room temperature Ni grows on Ag(100) in clusters that have a typical lateral extent of ~ 30 Å. The heights of these clusters are primarily 2-5 Å; however, some clusters are observed with a height of only ~ 1 Å. This implies subsurface segregation occurs even at room temperature. Upon annealing this system, the areal density of these clusters is reduced by a factor of 3 and the average height is reduced by tenfold to ~ 0.2 - 0.5 Å. In addition,

exposure of this surface to oxygen does not show evidence for NiO formation. This implies that Ni has segregated subsurface forming phase separated Ni nanoclusters covered by a Ag overlayer. That is, it has been unambiguously shown that the morphology of the subsurface system is that of embedded nanoclusters.

Concerning the electronic structure of the unannealed surface where Ni is deposited at 130 K, the data supports Ni *d*-bands showing a quasi one-dimensional structure arising from coupling between Ni and Ag in the perpendicular direction. The lack of dispersion in the plane is a result of the lack of lateral long-range periodicity. In the annealed surface, Ni *d*-bands behave three-dimensionally, which is a consequence of the hybridization between Ni *d* - Ag *sp* states accompanied by its increased coordination.

Chapter Six

Be/Si(111)

6.1 Introduction/Background

In this chapter, the gears are shifted substantially to focus on the reactive growth of metal on a semiconductors substrate. Specifically, this subject concerns the deposition of the alkaline earth metal, beryllium, on the Si(111)-(7 × 7) reconstructed surface. For this reason, the format of this chapter differs slightly from the previous organization of the metal on metal chapters.

Recently, theoretical predictions and experimental realizations of critically-stable, atomically-flat metal layers grown on semiconductor substrates has stimulated new research in the field of metal on semiconductor heteroepitaxy [57, 58]. The novel growth technique of low temperature deposition followed by subsequent annealing to room temperature has proved to demonstrate the collective phenomenon of this interesting growth process, known as electronic growth [58-60]. In fact, beryllium is predicted to exhibit magically stable films around 3 ML in addition to a critical thickness at 9 ML [57]. Motivated by this, the growth of

beryllium on the Si(111)-(7 × 7) surface has been studied over a wide coverage range and under various conditions of deposition temperature and annealing. Surprisingly these results indicate that a spontaneous chemical reaction occurs between beryllium and silicon at the surface, which results in the displacement of silicon atoms from the surface layer of the substrate. At low coverages, this results in the formation of an amorphous, clustered silicide, occurring at temperatures as low as 120 K.

Transition metal silicides have been studied extensively due to their technological importance in the metallization of silicon, for example in VLSI applications [61, 62]. From a surface science perspective, these transition metal silicides are typically grown using the technique of reactive epitaxy, where metal atoms are vapor-deposited on the silicon substrate held at elevated temperatures in order to facilitate the reaction. As mentioned above and in contrast to transition metals, the reaction of beryllium with silicon occurs at substantially low temperatures due to the highly reactive nature of the beryllium atoms and the unsaturated dangling bonds of the silicon at the surface. Although the formation of beryllium silicide has never been reported, neither in the bulk nor at the surface, other alkaline earth metal silicides are very well studied. For example the formation of Mg_2Si at the surface is well documented due to interest in the formation of low work function Schottky barriers [63, 64]. Despite its nonexistence, Be_2Si has been theoretically studied in the anti-fluorite crystal structure, common to other IIA-IV compounds, where various structural and electronic properties have been reported [65].

In this study, the techniques of variable-temperature scanning tunneling microscopy (STM) and synchrotron-based angle-resolved photoelectron

spectroscopy (ARPES) were used to elucidate this reactive deposition of beryllium on the Si(111)-(7 × 7) reconstructed surface. First the resultant morphology of the initial stages of the reaction will be described for the room temperature case and then structural and electronic evidence of this silicide formation is shown to occur at substantially reduced temperatures. A description of the structural results of beryllium deposition on silicon at elevated temperatures, and increased coverages is then given. Finally, the formation of beryllium silicide ring clusters is discussed, a universal structure seen in other metal/silicon systems, obtained by annealing the samples to substantially high temperatures (~1150 K).

6.2 Experimental Details

In this study, small 5 × 5 mm^2 Si(111) samples were cut from larger Ø75 mm boron-doped Si(111) wafers with typical resistivities of 3.0 – 6.0 Ω-cm and average miscut angles of ± 0.5° (Virginia Semiconductor). The samples were then etched in 4% hydrofluoric acid for 40 seconds to remove the native oxide layers and rinsed in distilled water to arrest the acid etch. Samples were mounted on Ta sample platens and loaded into the experimental chamber through a load-lock system, allowing for new silicon samples to be transferred after each deposition and characterization. The Si(111)-(7 × 7) reconstruction was achieved by flash annealing the samples to 1400 K after degassing at 900 K using an electron-bombardment type sample heater. Sample temperatures were monitored using an optical pyrometer and a thermocouple mounted on the Ta platen. The (7 × 7) reconstructed surface provides for a highly ordered well-studied surface, which aids in the study of the initial stages of metal growth on semiconductor surfaces.

Beryllium deposition was facilitated by the use of an effusion cell with a pyrolytic boron nitride furnace liner and a W-3%Re/W-25%Re thermocouple mounted in the graphite crucible. One advantage of this type of deposition source is its ability to reproducibly deposit electrically neutral material over a large thickness range. The Be evaporation was carried out in a side-mounted deposition chamber equipped with a liquid nitrogen cooled baffle to inhibit contamination of the main chamber and the sample holder. The effusion cell temperature was maintained at 1400 K during deposition, corresponding to a rate of 0.01 ML/sec. The evaporation temperature was cross-referenced using the optical pyrometer as well as with the known coolant temperature, and the deposition rate was estimated from vapor pressure curves of beryllium as well as STM observations. In this study, deposition of Be was carried out at various substrate temperatures, specifically 120, 300, 600, and 800 K. Data were collected either at 120 K or at 300 K. All STM images presented here were collected in constant current mode with typical tunneling currents in the range of 0.5 – 2.75 nA and sample biases of 1.5 – 2.0 V.

6.3 Structural and Electronic Properties of Be/Si(111): Results and Discussion

Cleanliness of the Si(111) substrates was determined by STM before each deposition of beryllium. Typically, clean silicon surfaces were characterized by large terraces (~500 Å) of the (7 × 7) reconstruction with very few defects or adsorbed atoms observed (Fig. 35). Deposition of beryllium results in an atom-displacing chemicai reaction, therefore it is imperative to determine the cleanliness and order of the substrate before deposition. Moreover, as detailed below, high

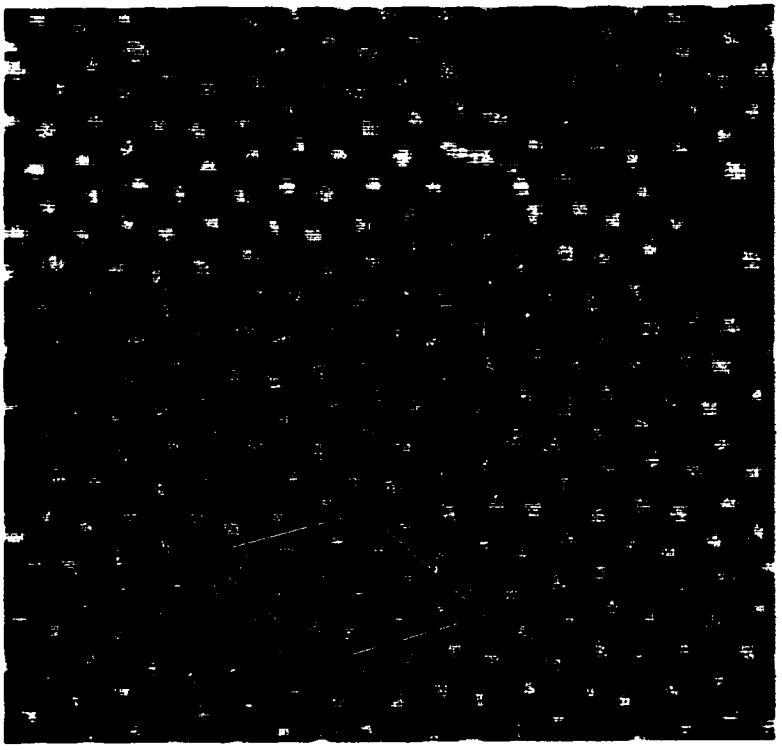

Figure 35. STM image of clean Si(111)-(7 × 7). This 100 Å × 100 Å image shows some, but relatively few defect sites in the upper-right corner. One (7 × 7) unit cell is outlined.

temperature annealing of the Be/Si interface results in a common ring cluster silicide which is occasionally observed on Si wafers inadvertently contaminated with common transition metals, e.g. Nickel [66]. For these reasons, it is essential to determine the cleanliness of the substrate.

A typical STM image of 0.1 ML of Be deposited at 300 K on the Si(111) – (7 × 7) surface is shown in Fig. 36. At this low coverage and deposition temperature the residual (7 × 7) superstructure can be seen, where four adjacent unit cells have been outlined. Two other obvious features are seen in the image: vacancies in superstructure of the substrate and small clusters of undetermined structure. In a similar study of the initial stages of silicide formation in Co/Si(111), it was determined that an interstitial precursor to silicide formation occurs [67], whereby Co atoms preferentially enter interstitial sites in the asymmetric unit cell of the superstructure. This interstitial formation is revealed as silicon atoms in the surface layer imaged substantially lower in height from the clean surface. In this case of Be deposited at room temperature, the vacancies, depicted in Fig. 36 as dark voids, are true vacancies, not simply apparent reductions in the height of the Si atoms. In fact, by adjusting the color scale appropriately, atoms from the second layer in the substrate become visible.

The clusters imaged on the surface range from 5 to 15 Å in diameter. The smallest of cluster are reasonably presumed to be composed of two to three atoms, whereas the larger clusters probably contain 15 to 20 atoms. The clusters have heights no more than a monatomic step height, however, due to the presumed reduced charge corrugation and general roughness of the nano-clustered

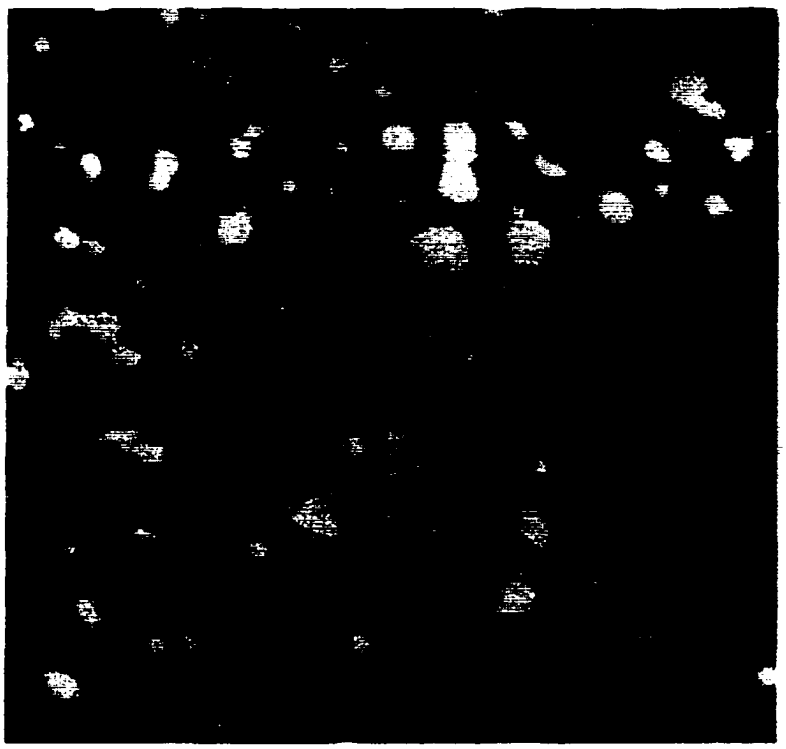

Figure 36. STM image of 0.1 ML of Be/Si(111) deposited at room temperature. (200 Å × 200 Å).

morphology, atomic resolution was not obtained. Based on the areal density, however, the number of vacancies is accounted for in assuming that the silicon atoms have been incorporated in the clusters through a silicide forming reaction.

In an attempt to inhibit the reaction of Be with the silicon atoms at the surface, samples were prepared and imaged at low temperature. The STM image shown in Fig. 37 is representative of the surfaces obtained when 0.1 ML of Be is deposited and consequently scanned at 120 K. Although the Si vacancies are substantially less than those observed in the room temperature case, the atom-displacing silicide reaction proceeds even at low temperatures. Cluster sizes resulting from this low temperature deposition typically range in diameter from 5 to 10 Å, substantially smaller and less numerous than in the case of room temperature deposition. In fact, under these conditions, not only are many silicon vacancies present, but there is also evidence for the previously mentioned interstitial incorporation of beryllium atoms beneath the upper most layer in the reconstructed surface. Unlike the case of interstitial Co in the Co/Si(111) system, however, there is no discernable preference for incorporation in either half of the asymmetric unit cell. Neither Si vacancies nor atoms with reduced height due to bonding with subsurface ad-atoms can be correlated with either the faulted or unfaulted halves of the (7 × 7) unit cell.

In order to reconcile these morphological observations with the formation of a silicide compound, low temperature core level photoemission spectroscopy was performed by S. –J. Tang, for various coverages of beryllium on Si(111) – (7 × 7). ARPES spectra are shown in Fig. 38, corresponding to a photon energy of 130 eV

Figure 37. STM image of 0.1 ML of Be/Si(111) deposited and scanned at 120 K. (200 Å × 200 Å).

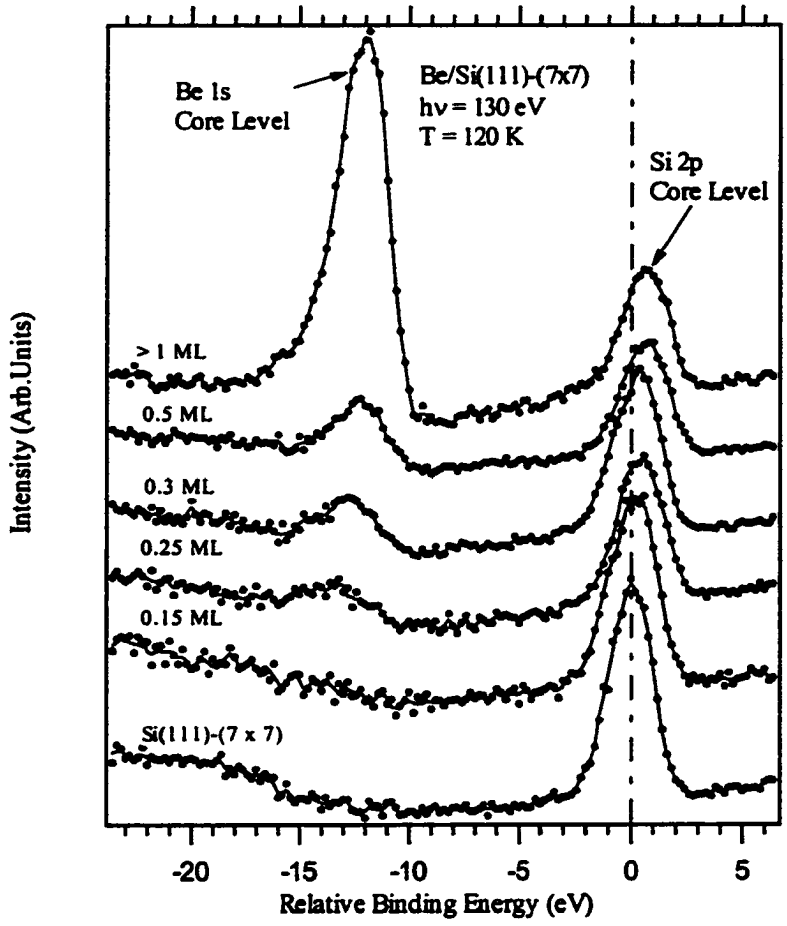

Figure 38. Core level photoemission spectra shown as a function of Be coverage on Si(111). Core level shifts are presumably due to band bending at a Schottky barrier formed between the Be_xSi_y/Si interface.

with the sample held at a temperature of 120 K. The abscissas in Fig. 38 are shifted to measure energies with respect to the centroid of the silicon $2p$ core level peak. The binding energy of this peak is ~ 99.5 eV relative to the valance band maximum. It is acknowledged that this Si $2p$ core level peak in the spectra is composed of the splitting into $2p_{1/2}$ and $2p_{3/2}$ with contributions from the bulk as well as the surface, however due to the limited resolution of the spectrometer used, these contributions are unresolved. Despite this lack of resolution in these measurements, a 1 eV shift in the Si $2p$ core level as well as in the Be $1s$ core level is observed. These results are consistent with band bending due to the formation of a Schottky barrier formed at the interface. A chemical shift in the Si core level due to the bonding in the silicide formation could also explain these results. Moreover, based on the morphological changes seen in the STM images, it seems that we can rule out the core level shifts as resulting from band bending due to the Schottky barrier formed form the Be/Si interface, but rather from a Be_xSi_y/Si interface where by the Be_xSi_y is presumed to be metallic. In fact, although valence band photoemission spectra and scanning tunneling spectra do not indicate a complete collapse in the semiconductor band gap, there is evidence for a small density of states near the Fermi level for this interface, indicating a semi-metallic nature.

Truly, the low coverage/low temperature data tell the entire story. By using low temperatures this atom-displacing reaction has been arrested as far as possible with the equipment available in this study. By studying the low coverage regime, the highly ordered surface of the (7 × 7) reconstruction was used to observe the gradual "etching" of silicon atoms upon deposition of beryllium. Of course, increased coverages result in even more silicon displacement and increased clustering to the

point where the (7 × 7) is completely unrecognizable. Due to the intrinsic roughness of this resultant morphology, very little structural information can be obtained. As is reasonable, clusters increase in size and density.

As mentioned in the introductory paragraphs, low temperature deposition followed by annealing to room temperature could ideally result in atomically flat layer growth. In fact STM measurements were made under these conditions in the coverage ranges as predicted by Zhang *et al.* [57]. Basically, this was done to confirm the assumptions that this growth mode would not occur due to the apparent reactivity of this system observed at the lower coverages. Indeed under these conditions the morphological characteristics are extremely rough with typical cluster sizes on the order of 20 Å in diameter and heights of 3 – 7 Å (Fig. 39). In conclusion, silicon is not the appropriate substrate on which to grow atomically flat films of beryllium.

In the formation of transition metal silicides by means of reactive epitaxy, it is often the case that silicide superstructures result. For example, a common reconstruction comprised of silicon adatoms back-bonded at threefold sites arranged in a 2 × 2 pattern occurs for $FeSi_2$, $CoSi_2$ and $NiSi_2$ [68]. When Be is deposited at 120 K or 300 K, STM results only indicate disordered clustering on the surface. Figure 40 shows an STM image of 0.5 ML of Be deposited on the Si(111)-(7×7) surface held at 750 K. Although individual atoms are resolved in the image, no superstructure resulted from these conditions of growth. The clusters in Fig. 40 are on average 10 – 12 Å in diameter and ~ 2.5 Å in height. Consistent with an Arrhenius dependence of reaction rate on temperature, elevated substrate

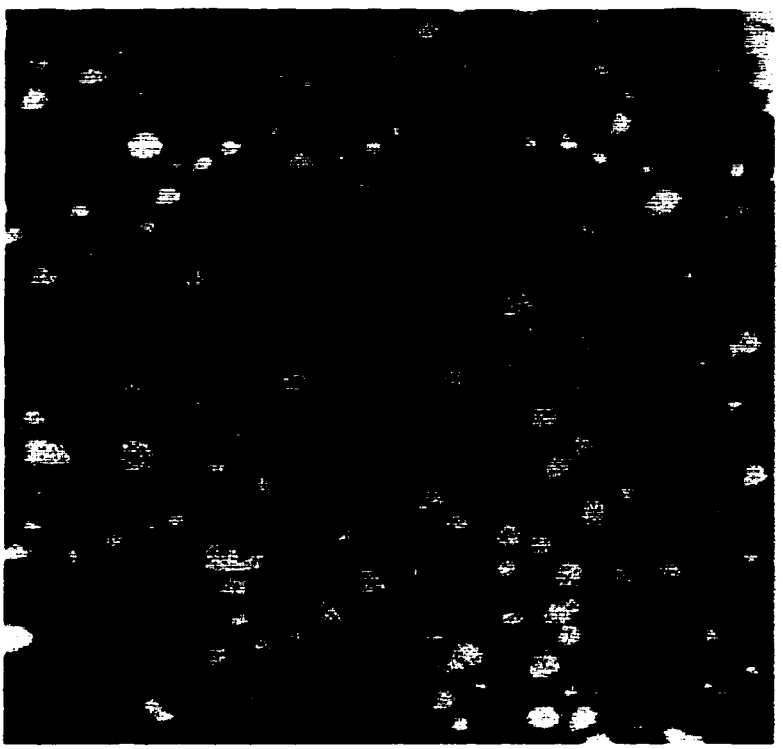

Figure 39. STM image of 9 ML of Be deposited on Si(111) at 120 K and annealed to room temperature. (500 Å × 500 Å).

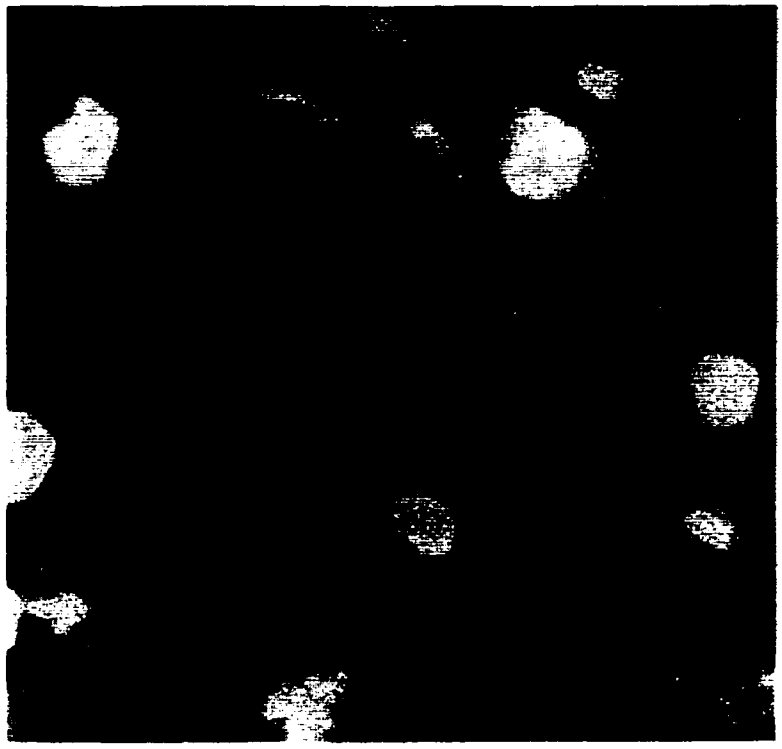

Figure 40. STM image of 0.5 ML of Be deposited on Si(111) at 750 K. (100 Å × 100 Å).

temperatures result in complete destruction of the (7 × 7) even for coverages as low as 0.2 ML.

Finally, a discussion is given concerning the observation of silicide ring clusters occurring as a result of annealing Be/Si(111) surfaces to 1175 K (Fig 41). Ring clusters formed in transition metal (TM) silicide systems are well documented [69]. In their studies, Parikh *et al.* investigated the formation of ring clusters for numerous transition metals. A distinction was made between near-refractory TM and near-noble TM, where most near noble TMs form the ring cluster structure and none of the near-refractory TMs do. Finally, Parikh *et al.* determined that the common characteristic was the TM – silicon bond length, where elements forming a minimum TM – silicon bond length less than 2.5 Å form the ring cluster. Silicide ring clusters are characterized by a single metal atom in a substitutional site in the top layer of Si(111) surrounded by six Si adatoms, of which three are bridge bonded with the metal atom and fully coordinated (Fig. 42). Evidence of this substututional process is apparent in Fig. 41 where the formation of the (7 × 7) reconstruction along the step edge is a result of Si condensation. As the beryllium atoms are substituted into the surface layer, the expelled Si atoms wander the terrace, finally condensing at the step edge.

The fact that only metals with a silicon bond length less than 2.5 Å form ring clusters is an intriguing phenomenon. This gives insight into the characteristics of the Be-Si bond, especially since atomic resolution was not obtained for the silicide clusters resulting from deposition of Be on Si(111). According to the calculation of bulk Be_2Si performed by Corkill *et al.*, the equilibrium Be-Si bond length is 2.24 Å,

suggesting that ring clusters can be formed for this system [65]. This bond length is based on the covalently bonded, tetrahedral anti-fluorite crystal structure, and agrees well with the simple sum of Pauling's tetrahedral covalent radii equal to 2.23 Å [70]. The fact that Be_2Si has never been experimentally realized in the bulk and that this STM study failed to reveal the structural details of the silicide clusters leaves many questions unanswered. On the other hand, the observations of the ring clusters and the theoretical prediction of bond lengths ~ 2.24 Å suggests that bulk beryllium silicide may one day be realized. Moreover, because ring clusters occur for a wide range of metals, this implies that they may play an important role in silicide reactions in ultra-thin films.

In summary it has been shown that a spontaneous solid phase chemical reaction occurs as a result of deposition of beryllium on Si(111)-(7 × 7) at temperatures as low as 120 K. Under various conditions of coverage and substrate temperature, this growth generally results in a very rough, highly clustered morphology. At coverages as low as 0.1 ML, low temperature and room temperature Be deposition results in an atom-displacing reaction where the (7 × 7) superstructure of the substrate becomes etched away and incorporated into silicide nano-clusters. Evidence of an interstitial precursor at low temperatures has been observed to be similar to the Co/Si(111) system, but with no preference for either the faulted or unfaulted half of the unit cell. At elevated temperatures, the reaction proceeds at a higher rate, and never forms an ordered superstructure under any of the conditions studied in this experiment. Annealing of the Be/Si surface to 1175 K results in the universal ring cluster structure common to metal systems for which the metal–silicon

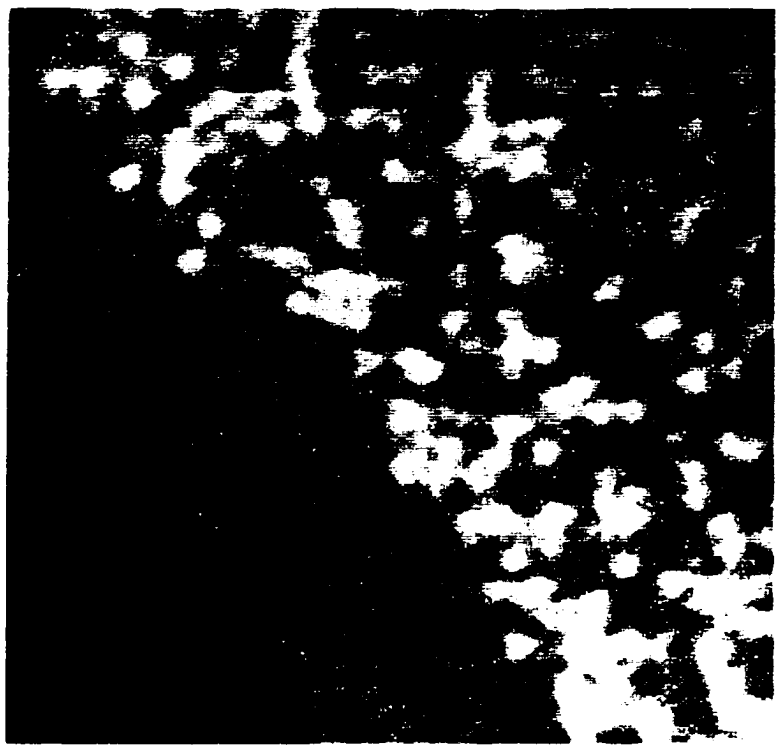

Figure 41. STM image of 1 ML of Be/Si(111) annealed to 1175 K showing the formation of the universal ring clusters. (200 Å × 200 Å).

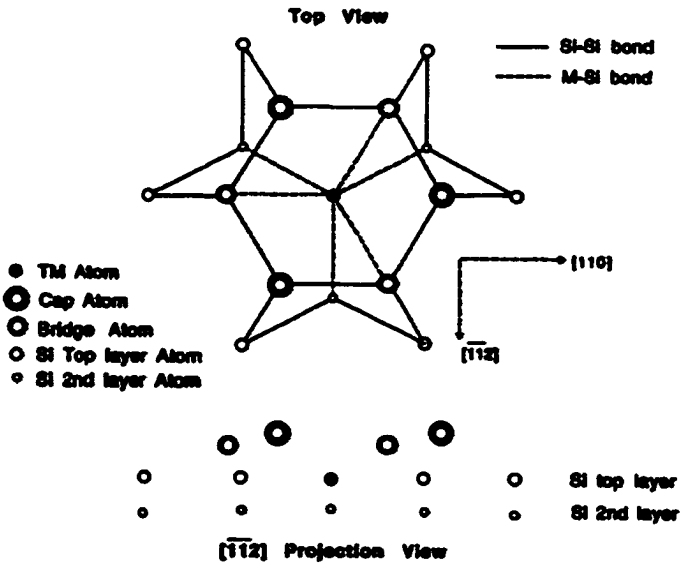

Figure 42. Ball and stick model of the ring cluster structure proposed by Parikh *et al.* (from Ref. [69]).

bond length is characteristically less than 2.5 Å. Finally it is hoped that these preliminary studies of the reactive epitaxy of Be/Si(111) prompt additional theoretical and experimental studies of this intriguing compound.

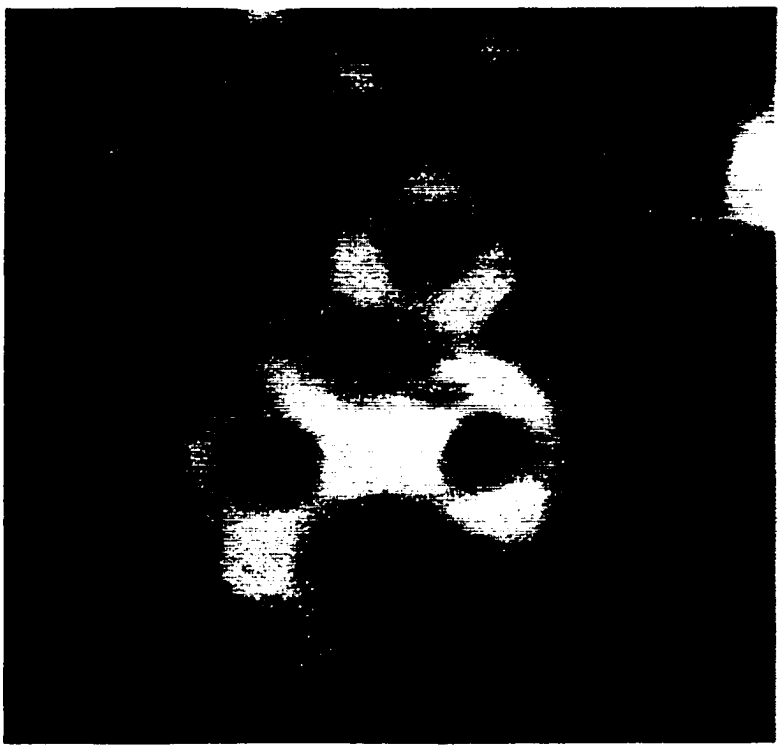

Figure 43. STM image of beryllium silicide ring clusters. (50 Å × 50 Å). The three lobes seen in the ring clusters are due to the different bonding sites in the structure (see Fig. 42).

Chapter Seven

Summary

In this work, the general focus has been place on the heteroepitaxy of ultra-thin metal films. Particular attention has been given to the initial stages of growth for systems that exhibit deviations from the traditional growth modes. For the metal on metal systems investigated, these deviations in growth tend to be driven by excess strain energies due to their characteristically large lattice mismatch. This lattice mismatch is the origin for their bulk immiscibility, yet it also drives these systems to form intermixed phases at the surface. This shows the fundamentally different nature of the surface as compared to the bulk. The deposition of Be on Si results in a completely different growth mode, where a spontaneous solid-phase chemical reaction occurs at the surface. This has been shown to occur at substantially reduced temperatures, elucidated the highly reactive nature of beryllium at the silicon surface.

The metal on metal systems characterized in this study, namely Ag/Cu(110), Ag/Ni(110) and Ni/Ag(100), each differ from one another in terms of the details in growth morphology, however, electronic hybridization between states of different atomic species is a common trend throughout. With the negligible degree of *d*-band

overlap in each case, this hybridization is manifested through the interatomic mixing of *sp* and *d* states. As a result of this electronic mixing of states, the dimensionality in these systems is extremely interesting. As a general trend, the *d*-bands of the adatoms have revealed quasi-three-dimensional electronic structures. This is a consequence of increased coordination with accompanying coupling to the Bloch waves of the substrate.

In summary, the Ag/Cu(110) and Ag/Ni(110) systems display extremely similar results, both morphologically and electronically. In both systems there is a strong propensity for the alignment of Ag atoms along the [001]-direction of the substrate surface. This is due to the anisotropic nature of the (110) surface and the large lattice mismatch between the adatoms and the substrate. Both systems form substitutional surface alloys in the low coverage regime, however morphological differences emerge as the coverage is increased.

The Ag/Cu(110) system is driven to a de-alloyed phase for coverages between 0.4 to 0.9 ML. In this case, the symmetry of the surface has been reduced due to the incommensurate structure of the de-alloyed Ag atoms and the fact that numerous Cu vacancies exist beneath the Ag chain structure. This reduction in symmetry is observed in the photoemission data as Cu bands become observable in photoemission geometries that would otherwise forbid their detection base on dipole selection rules. Moreover, the Cu states existing in the interfacial region exhibit modified dispersion due to the altered crystal potential and hybridization between the Ag *sp*-band and the Cu *d*-bands.

In contrast, Ag remains alloyed in the Ni(110) surface for substantially high coverage (< 1 ML) where the Ag atoms, despite the buckled morphology, remain in pseudomorphic registry with the underlying substrate. Similar to the Ag/Cu(110) system, where the substrate *d*-bands are observed to disperse anomalously, the Ni *d*-bands show energetic shifts due to hybridization with the adatoms. However, based on dipole selection rules, the symmetry for this Ag/Ni(110) system is retained, due to the conformity of pseudomorphic registry within the substrate surface.

The dimensionality of the Ag *d*-bands is an interesting property of both surfaces. On the Cu(110) surface, in the coalesced zig-zag chain structure, the Ag *d*-bands exhibit a highly anisotropic nature, where the Ag *d*-bands behave one-dimensionally along the chains and show a two-dimensional electronic structure perpendicular to the chains. Along the chains, the dominant interaction is Ag-Ag, whereas perpendicular to the chains the Ag states are hybridized with the nearby Cu atoms. In contrast, the Ag *d*-bands behave quasi-three-dimensionally in the Ag/Ni(110) system, being alloyed and hybridized strongly within the Ni(110) surface. As the Ag atoms are de-alloyed from the Ni(110) surface at ~ 1 ML, the Ag *d*-bands display a characteristic two-dimensional electronic structure. Because the Ag/Ni(110) system displays these two radically different surface morphologies, the drastic changes in electronic dimensionality allow for a particularly nice way to examine these systems through a correlative study between morphology and electronic structure.

The complementary system, Ni/Ag(100), shows a completely different surface morphology from the above mentioned systems. This system displays a three-dimensional, nano-clustered growth morphology, which, upon annealing,

results in buried Ni nano-clusters capped off by at least one layer of Ag. Again, the trend of *sp-d* hybridization results, but only to a large degree when the system is annealed, and the Ni clusters have substantially increased coordination. Interestingly, the Ni *d*-bands exhibit a one-dimensional-like electronic structure when deposited at low temperature. This is a result of the highly confined nature of the nano-clusters randomly distributed throughout the Ag terraces. The Ni *d*-bands behave three-dimensionally as the clusters are allowed to couple to the Bloch waves of the substrate upon annealing when the clusters are buried into the surface.

In general, these metal on metal systems are quite similar, despite differences in the details. These systems are characterized by the metallic bond, which is manifested through mixing of states in the valence bands of the alloyed material. In stark contrast, are the strongly, perhaps covalently, bonded systems of metal-semiconductor compounds formed through reactive epitaxy or other means of solid-phase chemical reactions. The reactive epitaxy of Be on Si(111)-(7 × 7) is the subject of Chapter Six and is summarized below.

Deposition of Be on the highly ordered Si(111)-(7 × 7) reconstructed surface results in an atom-displacing chemical reaction where clusters of a silicide compound are formed on the surface. In general, Be deposition essentially etches the Si surface, whereby increased Be coverages eventually destroy the highly ordered (7 × 7) superstructure. This occurs for deposition temperatures as low as 120 K.

The resultant clusters appear to be amorphous, and under various conditions of coverage and deposition temperature, no superstructure results on the surface, as determined by STM and LEED. The only slightly ordered structure that resulted for

the Be/Si(111) system was the appearance of ring clusters that come about from annealing the Be/Si system to temperatures as high as 1175 K. This ring cluster structure is common to other metal/silicon systems, where it has been determined that this universal ring cluster occurs for systems with a metal-silicon bond length less that 2.5 Å. This implies that the Be-Si bond length must be less that 2.5 Å, which is in agreement with a calculated bond length for Be_2Si in the anti-fluorite structure. Even though beryllium silicide has never been realized in the bulk, it has been shown here that the silicide can be formed at the surface, although the exact stoichiometry remains unknown.

Finally, these studies have shed light on the correlation between the atomic and electronic structures of a diverse group of heteroepitaxial systems, which exhibit unique growth morphologies and consequential electronic structures. More importantly, through studies of these types of model systems, an intuitive understanding of surfaces of increasing complexity has been formed, which will aid in the tailoring of materials having advantageous chemical or magnetic properties.

References

1. E. Bauer, *Z. Krist.* **110**, 372 (1958), and *Appl. of Surf. Sci.* **11/12**, 479 (1982).

2. T. Young, *Philos. Trans.* **95**, 65 (1805).

3. F. C. Frank and J. H. van der Merwe, *Proc. Roy. Soc. (London)*, **A200**, 125 (1950), and *ibid.* **A198**, 205 (1949).

4. M. Volmer and A. Weber, *Z. Phys. Chem.*, **119**, 277 (1926).

5. J. N. Stranski and L. Krastanov, *Ber. Akad. Wiss. (Wien)* **146**, 797 (1938).

6. J. W. Cahn, *Acta Metall.* **9**, 795 (1961).

7. M.Ø. Pedersen, S. Helveg, A. Ruban, I. Stensgaard, E. Lægsgaard, J.K. Nørskov and F. Besenbacher, *Surf. Sci.* **426**, 395 (1999).

8. K. W. Jacobsen, P. Stoltze, and J. K. Nørskov, *Surf. Sci.* **366**, 394 (1996).

9. S. -L. Chang, J. -M. Wen, P. A. Thiel, S. Günther, J. A. Meyer, and R. J. Behm, *Phys. Rev. B* **53**, 13747 (1996), and T. J. Raeker, D. E. Sanders, and A. E. DePristo, *J. Vac. Sci. Technol. A* **8**, 3531 (1990).

10. C. Nagl, E. Platzgummer, M. Schmid, P. Varga, S. Speller and W. Heiland, *Phys. Rev. Lett.* **75**, 2976 (1995).

11. W. F. Egelhoff, Jr., *J. Vac. Sci. Technol. A* **7**, 2060 (1989).

12. B. C. Bolding and E. A. Carter, *Surf. Sci.* **268**, 142 (1992).

13. B. Aufray, H. Giordano, B. Legrand, and G. Tréglia, *Surf. Sci.* **307**, 531 (1994).

14. J. M. Roussel, A. Saúl, G. Tréglia and B. Legrand, *Surf. Sci.* **352**, 562 (1996).

15. J. M. Roussel, A. Saúl, and G. Trélia, *Phys. Rev. B* **55**, 10931 (1997).

16. J. M. Roussel, A. Saúl, G. Tréglia, and B. Legrand, *Phys. Rev. B* **60**, 13890 (1999).

17. J. Bardeen, *Phys. Rev. Lett.* **6**, 57 (1961).

18. F. Besenbacher, *Rep. Prog. Phys.* **59**,1737 (1996).

19. J. Tersoff and D. R. Hamann *Phys. Rev. Lett.* **50**, 1998 (1983).

20. C. M. Berglund and W. E. Spicer, *Phys. Rev.* **136** A1030 (1964), and *ibid.* **136**, A1044 (1964).

21. S. Hüfner, Photoelectron Spectroscopy, (Springer-Verlag, Berlin, 1995).

22. J. Hermanson, *Solid State Commun.* **22**, 9 (1977).

23. W. Eberhardt and F. J. Himpsel, *Phys. Rev. B* **21**, 5572 (1980).

24. G. Borstel, W. Braun, M. Neumann and G. Seitz, *Phys. Status Solidi B* **95**, 453 (1979), and G. Borstel, M. Neumann and G. Wöhlecke, *Phys. Rev B* **23**, 3121 (1981).

25. L. P. Bouckaert, R. Smoluchowski, and E. P. Wigner, *Phys. Rev.* **50**, 58 (1936).

26. M. Tinkham, Group Theory and Quantum Mechanics, (McGraw-Hill Inc., New York, 1964), p. 325.

27. C. L. Allyn, T. Gustafsson, and E. W. Plummer, *Rev. Sci. Instrum.* **49**, 1197 (1973).

28. E. Morikawa, J. D. Scott, E. D. Poliakoff, R. L. Stockbauer, and V. Saile, *Rev. Sci. Instrum.* **63**, 1300 (1992).

29. F. Besenbacher, L. Pleth Nielsen, and P.T. Sprunger, in The Chemical Physics of Solid Surfaces, edited by D. A. King and D. P. Woodruff (Elsevier Science B. V., Amsterdam, The Netherlands, 1997), Vol. 8, Chap. 6, pp. 207 – 257.

30. T. N. Taylor, R. E. Muenchausen, and M. A. Hoffbauer, *Surf. Sci.* **243**, 65 (1991), and T. N. Taylor, R. E. Muenchausen, M. A. Hoffbauer, A. W. Dinier van der Gon and J. F. van der Veen, *J. Vac. Sci. Technol. A* **8**, 2732 (1990).

31. P. W. Palmberg and T. N. Rhodin, *J. Appl. Phys.* **39**, 2425 (1968).

32. P. W. Palmberg and T. N. Rhodin, *J. Chem. Phys.* **49**, 134 (1968), and *ibid.* **49**, 147 (1968).

33. J. G. Tobin, S. W. Robey, L. E. Klebanoff, and D. A. Shirley, *Phys Rev B* **28**, 6169 (1983), and *ibid.* **33**, 2270 (1986), and *ibid.* **35**, 9056 (1987).

34. A. P. Shapiro, A. L. Wachs and T. -C. Chiang, *Solid State Commun.* **58**, 121 (1986).

35. L. Pleth Nielsen, F. Besenbacher, I. Stensgaard, E. Lægsgaard, C. Engdahl, P. Stoltze and J. K. Nørskov, *Phys. Rev. Lett.* **74**, 1159 (1995).

36. P. Thiry, D. Chandesris, J. Le Cante, C. Guillot, P. Pinchaux and Y. Petroff, *Phys. Rev. Lett.* **43**, 82 (1979).

37. G. A. Burdick, *Phys. Rev.* **129**, 138 (1963).

38. N. E. Christensen, *Phys. Status Solidi B* **54**, 551 (1972).

39. A. P. Shapiro, A. L. Wachs, T. Miller, and T. -C. Chiang, *Solid State Commun.* **55**, 1101 (1985).

40. A. P. Shapiro, T. C. Hsieh, A. L. Wachs, T. Miller, and T. -C. Chiang, *Phys Rev. B* **38**, 7394 (1988).

41. A. P. Shappiro, A. L. Wachs, T. C. Hsieh, T. Miller, P. John, and T. -C. Chiang, *Phys. Rev. B* **34**, 7425 (1986).

42. P. T. Sprunger (private communication).

43. H. Wern, R. Courths, *Surf. Sci.* **162**, 29 (1985).

44. J. Tersoff, *Phys. Rev. Lett.* **74**, 434 (1995).

45. M. A. Thompson, M. Onelion and J. L. Erskine, *Bull. Am. Phys. Soc.* **31**, 675 (1986).

46. S.C. Hong, A. J. Freeman and C. L. Fu, *Phys. Rev B* **39**, 5719 (1989).

47. V.K. Kimikov and K. B. Khokonov, *J. Appl. Phys.* **54** 1346 (1983).

48. K. S. Lee, S. H. Kim, H. G. Min, J. Seo, and J-S Kim, *Surf. Sci.* **377**, 918 (1997).

49. Th. Bertrams and H. Neddermeyer, *J. Vac. Sci. Technol. B*, **14**, 1141 (1996).

50. A. Christensen *et al.*, *Phys. Rev. B* **56**, 5822 (1997).

51. G. J. Mankey, K. Subramanian, R. L. Stockbauer, and R. L. Kurtz, *Phys. Rev. Lett.* **78**, 1146 (1997).

52. L. Liebermann, J. Clinton, D. M. Edwards, and J. Mathon, *Phys. Rev. Lett.* **25**, 323 (1970).

53. J. Tersoff and L. M. Falicov, *Phys. Rev. B* **26**, 6186 (1982).

54. D. -S. Wang, A. J. Freeman, H. Krakauer, *Phys. Rev. B* **24**, 1126 (1981).

55. M. A. Thompson and J. L. Erskine, *Phys. Rev. B* **31**, 6832 (1985).

56. H. Huang, X. -Y. Zhu, and J. Hermanson, *Phys. Rev. B* **29**, 2270 (1984).

57. Z. Zhang, Q. Niu and C. -K. Shih, *Phys. Rev. Lett.* **80**, 5381 (1998).

58. A. R. Smith, K. -J. Chao, Q. Niu, C. -K. Shih, *Science* **273**, 226 (1996).

59. K. Budde, E. Abram, V. Yeh, M. C. Tringides, *Phys Rev. B* **61**, 10602 (2000), and V. Yeh, L. Berbil-Bautista, C. Z. Wang, K. M. Ho, and M. C. Tringides, *Phys. Rev. Lett.* **85**, 5158 (2000).

60. I. Matsuda, H. W. Yeom, T. Tanikawa, K. Tono, T. Nagao, S. Hasegawa, and T. Ohta, *Phys. Rev. B* **63**, 5325 (2001).

61. M. -A. Nicolet and S. S. Lau, in *VLSI Microstructure Science*, edited by N. G. Einspruch and G. B. Larrabee (Academic, New York, 1983), p. 130.

62. A. H. Reader, A. H. Ommen, P. J. W. Weijs, R. A. M. Wolters, and D. J. Oostra, *Rep. Prog. Phys.* **56**, 1397 (1992).

63. C. Wigren, J. N. Andersen, R. Nyholm and U. O. Karlsson, *Surf. Sci.* **289**, 290 (1993).

64. M. R. J. van Buuren, C. L. Griffiths, H. van Kempen, *Surf. Sci.* **314**, 172 (1994).

65. J. L. Corkill and M. L. Cohen, *Phys. Rev. B* **48**, 17138 (1993).

66. P. A. Bennett, M. Copel, D. Cahill, J. Falta, and R. M. Tromp, *Phys Rev. Lett.* **69**, 1224 (1992).

67. P. A. Bennett, D. G. Cahill, M. Copel, *Phys. Rev. Lett.* **73**, 452 (1994).

68. P. A. Bennett and H. von Känel, *J. Phys. D.* **32**, R71 (1999).

69. S. A. Parikh, M. Y. Lee and P. A. Bennett, *J. Vac. Sci. Technol. A* **13**, 1589 (1995).

70. L. Pauling, *The Nature of the Chemical Bond*, 3rd ed. (Cornell University Press, Ithaca, NY, 1960).

Appendix

Experimental Design and Schematic Drawings

The intention of this appendix is to provide detailed drawings, schematics and tables of experimental apparatus so that similar designs and existing equipment may be reproduced and easily used. Broadly, this appendix is comprised of three areas: details concerning the UHV STM chamber design and its modification, the electronics schematics for the Auger Electron Spectroscopy unit and finally details of the Aarhus STM concerning the inchworm piezo re-polarization and tip etching.

The UHV STM chamber has been briefly described in Chapter Two, section 2.3.1. This chamber is comprised of a 12-inch diameter ultra-high vacuum chamber, fabricated by Thermionics Vacuum Products, whose overall length is 18.18 inches. It was made from 3/16-inch type 304 stainless steel and has 25 Conflat® flanged ports. Although the chamber itself is short, the *z*-translation stage has a 30-inch stroke, which facilitates sample transfer through the STM chamber as well as into the center of the CAMD ARUPS chamber or the Scienta endstation chamber. Many of the ports were fabricated using oversize tubes sometimes required for use with complex, yet compact instrumentation. Because the STM itself was fabricated in

Europe, the flange for the STM port was welded with the boltholes inline instead of straddling a vertical line as is customary with the American Vacuum Society's practices. The STM Vacuum Chamber port specifications are given in Table 4 with focal points given in Table 5.

The pumping cross, shown in Fig. 44, mounts to the main pumping port of the chamber via a 107° elbow. The 107° elbow (Fig. 45) facilitates perpendicular mounting of the pumping cross through two independent rotation angles, one angle, θ, of 205° characterizing the pumping port on the chamber and a second angle, γ′ of 46° out of the plane to pull the pumping cross away from the chamber in the direction of the manipulator (see Fig. 46). The 107° angle was found using the general trigonometric relation,

$$\cos\gamma = \cos\theta\cos\theta' + \sin\theta\sin\theta'\cos(\phi - \phi'), \qquad \text{(Eq. 17)}$$

where $\theta = 205°$,

$\theta' = 0°$,

$\phi = 90°$,

$\phi' = 46°$,

so that $\gamma = 107°$.

The pumping cross is equipped with flanges to support use of one 300 l/s ion pump, a 150 l/s turbomolecular pump, a titanium sublimation pump with a liquid nitrogen cold trap and a flange on which to mount a series of parallel mounted precision leak valves to act as a gas manifold.

Table 4. UHV STM Vacuum Chamber Port Specification.

No.	Flange Type	Tube (O.D.)	Focal Point	Port Length	beta	gamma	Port Use
1	6" CF	4.0" I.D.	B	9.090"	180	0	XYZ Manip.
2	6" CF	4.0 I.D.	B	9.090"	0	0	To ARUPS
3	2 ¾" CF	1.75"	E	5.5"	17	90	View Port 1
4	1.33" CF	0.75"	F	7.00"	90	0	Light
5	1.33" CF	0.75"	F	7.00"	90	180	Push-Pull for Stability
6	2 ¾" CF	1.75"	A	8.5"	90	355	Sputter Gun
7	2 ¾" CF	1.75"	A	8.5"	90	330	View Port 2
8	8.0" CF	6.5"	A	9.0"	90	270	LEED
9	8.0" CF	6.0"	A	9.0"	90	205	Pumping Port
10	6.0" CF	4.0"	A	10.0"	90	150	CMA
11	6.0" CF	4.0"	A	8.0"	90	90	View Port 3
12	6.0" CF	4.0"	A	8.0"	90	30	View Port 4
13	2 ¾" CF	1.75"	B	9.0"	90	337.5	Thin Film Monitor

(Table 4 continued)

14	2 ¾" CF	1.75"	B	9.0"	90	247.5	Evap 1
15	2 ¾" CF	1.75"	B	8.5"	90	175	Mass Spec
16	2 ¾" CF	1.75"	B	9.0"	90	67.5	Evap 2
17	4.5" CF	2.5"	B	8.0"	90	0	View Port 5
18	2 ¾" CF	1.75"	C	8.5"	90	350	Ion Gauge
19	6.0" CF	4.0"	C	8.0"	90	315	View Port 6
20	2 ¾" CF tapped	2.75"	C	8.0"	90	270	Wobble Stick
21	2 ¾" CF	1.75"	C	8.0"	90	225	Magnetic Transfer Rod
22	2 ¾" CF	1.75"	C	8.0"	90	180	Sample Storage
23	2 ¾" CF	1.75"	D	6.70"	90	180	View Port 7
24	8.0" CF in-line bolt holes	6.5"	C	9.0"	90	90	STM
25	4 5/8" CF	3.0"	E	7.5"	90	0	View Port 8

Table 5. Focal points for UHV STM Vacuum Chamber

FP	X	Y	Z
A	0	0	5.215
B	0	0	9.090
C	0	0	12.965
D	0	4.0	12.965
E	0	3.10	12.965
F	0	0	15.750

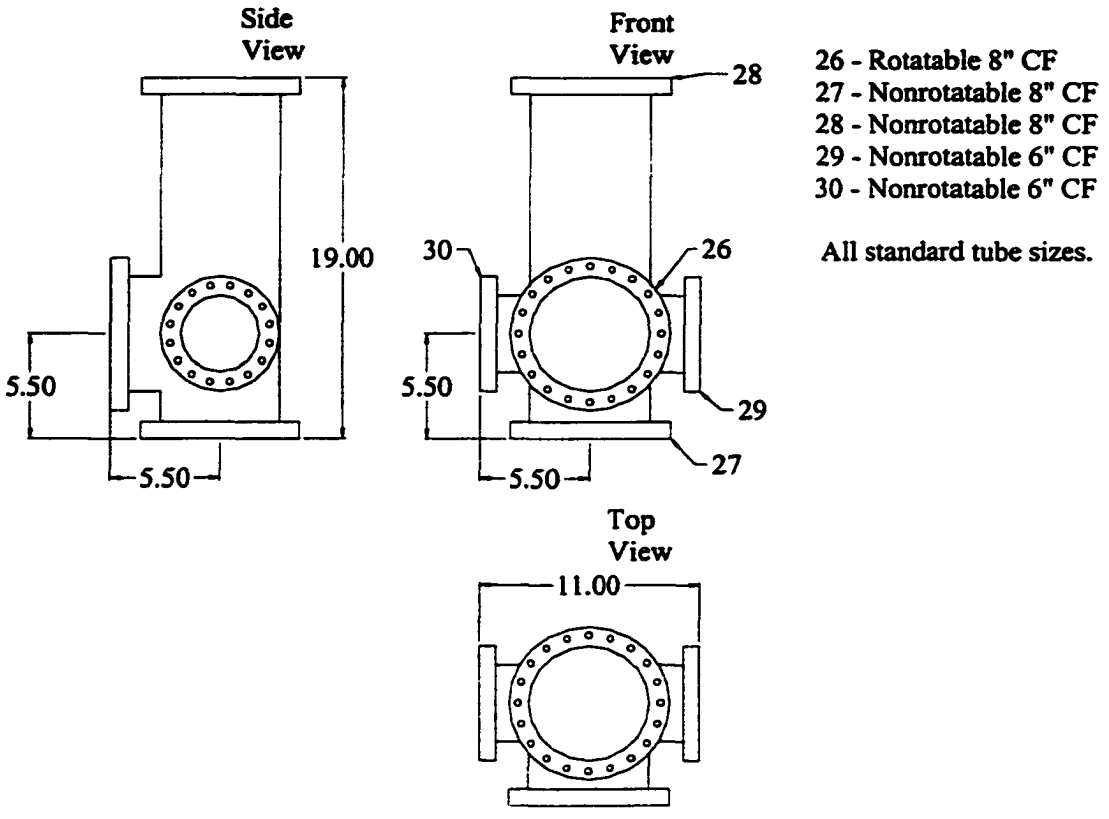

Figure 44. Design drawings for the pumping cross of the UHV STM Vacuum Chamber.

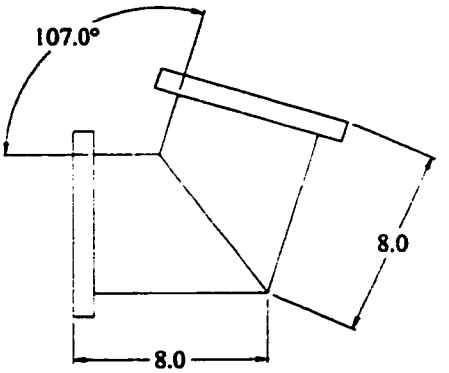

Figure 45. Design drawing for the 107° elbow. This elbow is used to couple the pumping cross to the pumping port on the STM Chamber.

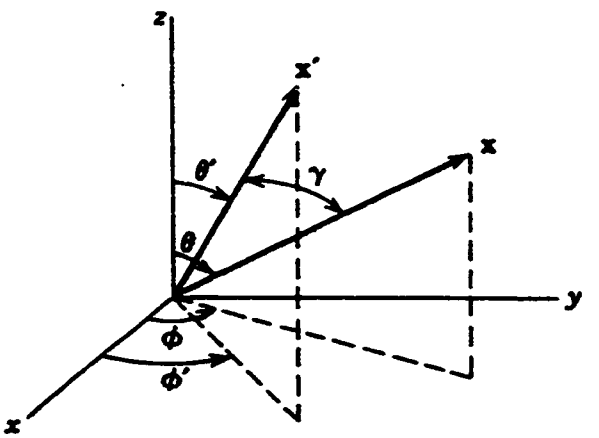

Figure 46. Geometric representation of angles used in Equation 17.

The STM stand was constructed of 4×4 in^2 rectangular tubing made of low-grade carbon steel. A number of orthogonal angled cross members were used for damping vibrations and oscillations that can hinder the data collection during the operation of the scanning tunneling microscope. The stand is equipped with three 1"-13 kinematic adjustment screws allowing for alignment and leveling of the chamber. Not only is the kinematic mounting important for alignment and adjustment when mounting onto an auxiliary chamber, but, since the STM hangs from damping springs, proper leveling of the chamber is required in order to keep the microscope electrically and vibrationally isolated during operation. The design drawings for this stand are shown in Figs. 47-50.

The sample manipulator is an off-the-shelf XYZΘ manipulator, designed and fabricated by McAllister Technical Services, however the sample holder mounted on the end of the McAllister support tube was of a completely customized design, (Figs. 51-56) fabricated by the LSU Physics machine shop. The coupling plate between the support tube and sample platen was designed to be as free from magnetic fields as possible. For this reason, the closest magnetic material to the sample is the stainless steel side of the liquid nitrogen dewar used to cool the sample. Because photoemission spectroscopy may be performed using this sample holder, the sample needs to be in a field free region. The liquid nitrogen dewar made by Thermionics Vacuum Products is electrically isolated from the earth ground of the chamber and is allowed to slide on a mounting plate (Fig. 53) to compensate for contraction and expansion during cycles of cooling and warming. The sample holder (Fig. 57) is

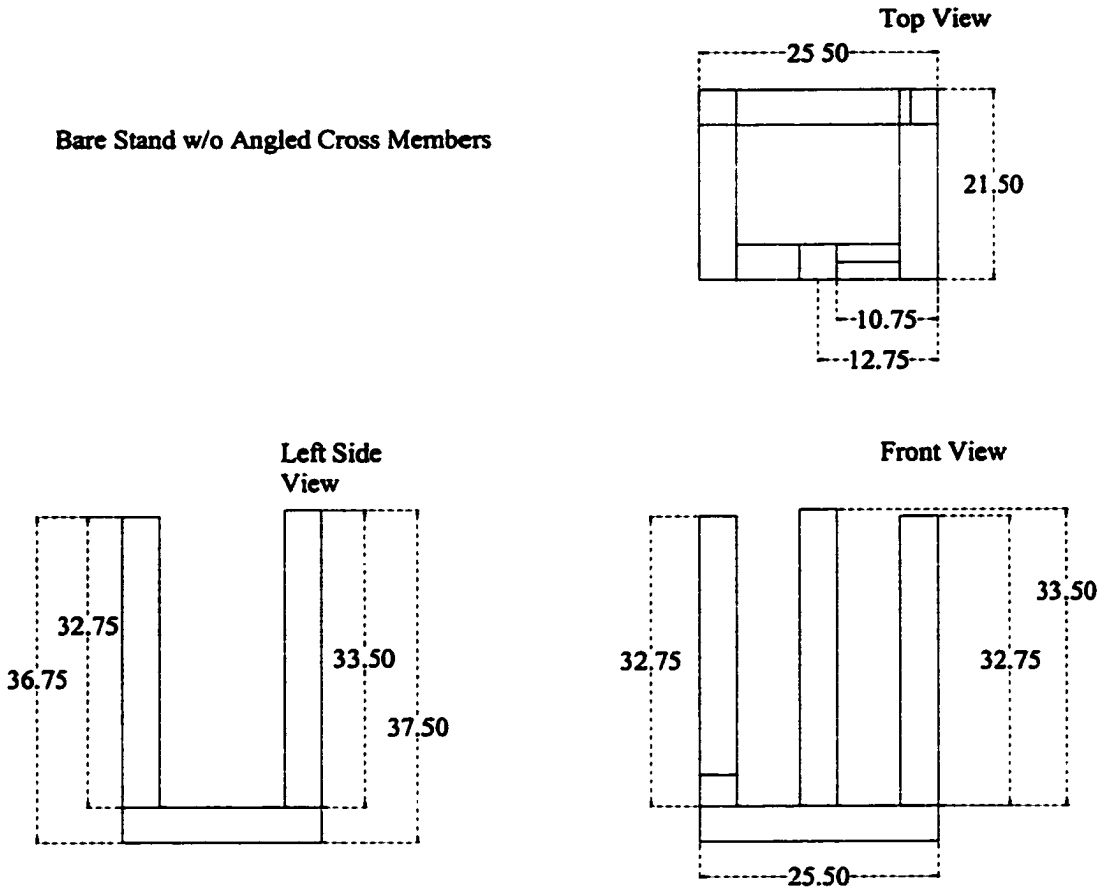

Figure 47. Design drawings for the STM Vacuum Chamber Stand depicting 4 × 4 inch tubes only.

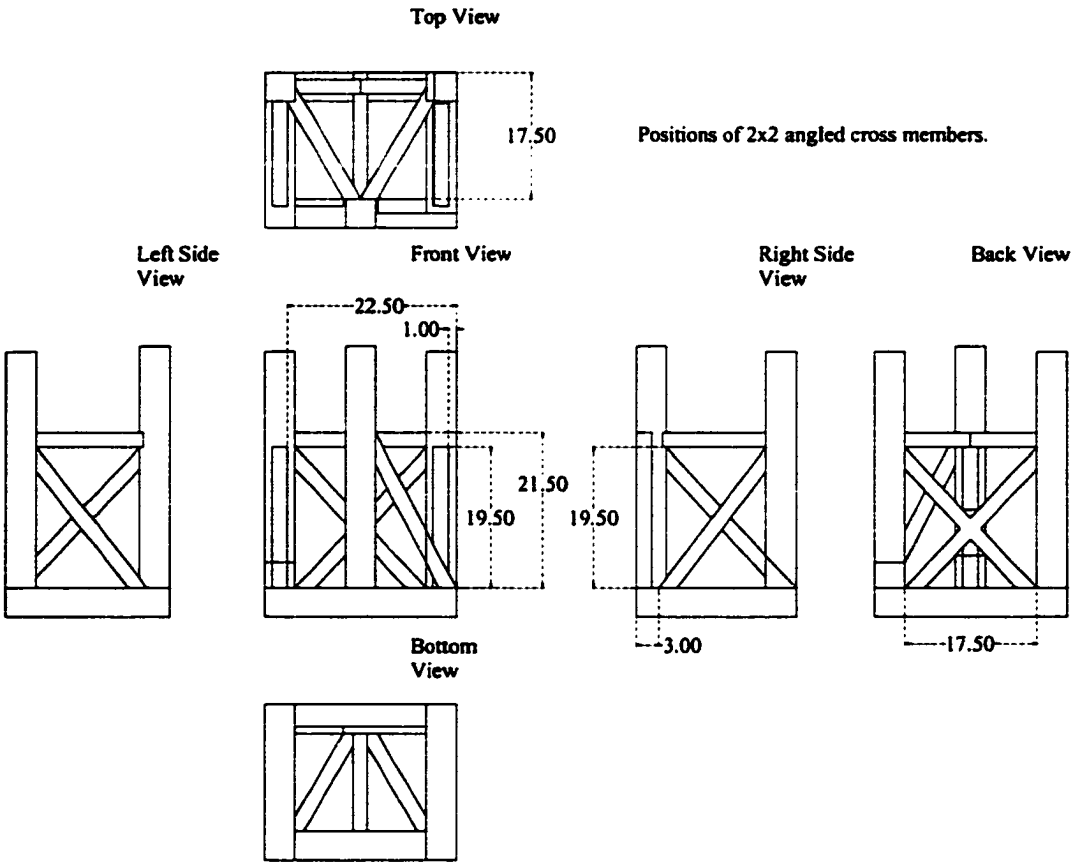

Figure 48. Design drawings for the STM Vacuum Chamber Stand depicting positions of 2 × 2 inch tubes.

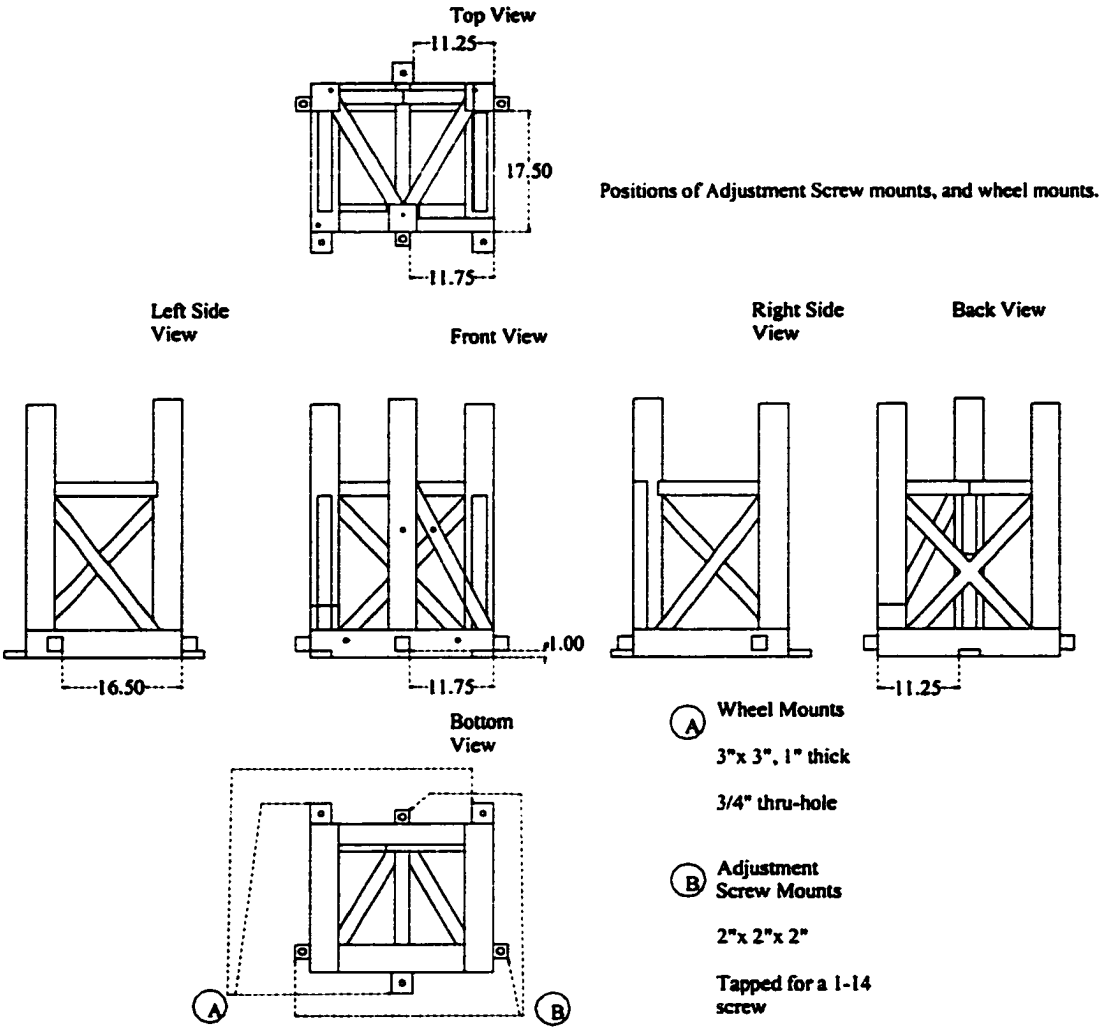

Figure 49. Design drawings for the STM Vacuum Chamber Stand depicting positions of adjustment screw mounts and wheel mounts.

Top View

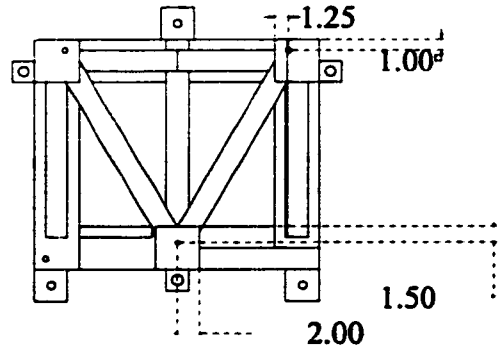

Positions and Dimensions of tapped and thru holes.

Front View

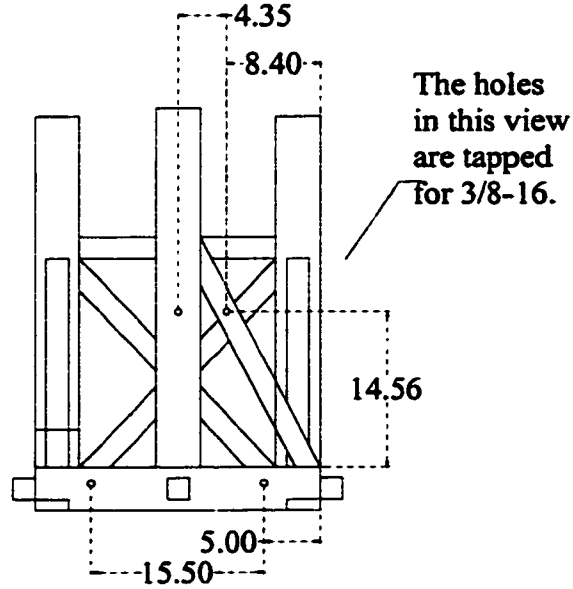

Figure 50. Design drawings for the STM Vacuum Chamber Stand depicting positions of tapped and through holes.

made from oxygen-free high conductivity Cu and is also electrically isolated from the earth ground of the chamber by way of four Macor® spacers (Fig. 56). The sample holder incorporated Mo springs with which to hold the sample platen, an electron bombardment-type sample heater made from commercially available Halogen lamps, thermocouples to measure the temperature to the sample as well as the Cu holder, and a wire to facilitate a sample bias or read induced sample currents. The sample holder is attached to the support tube via a 1/8-inch Ti plate (Fig. 52).

The sample platen is made of a 1 mm thick Ta plate onto which the sample crystals are directly mounted (Fig. 58). This platen has a slot to allow the tooth of the wobble stick pinschers to fit and Macor® isolated Alumel-Chromel thermocouple pins to plug into the sample temperature receptacle in the sample holder.

Three other customized designs were implemented in this STM chamber that will be briefly described here for possible future reference. The first of these is the design of the sample storage garage, the design drawings of which are shown in Figs. 59-62. This small, in-vacuum multiple sample storage facility was constructed from stock Al 6061 and is mounted onto a push-pull type motion feedthrough. This sample garage can hold up to eight of the 1-mm thick sample platens with a slot cut from the rear plate which allows for visible inspection as well as allowing for the thermocouple pins to fit through without the platen sliding all the way out. Each sample slot is numbered for cataloging and tracking multiple samples, which often look very similar. Each slot is also equipped with two vented #2-56 tapped holes in order to mount two retaining springs simply made from stainless steel shim stock.

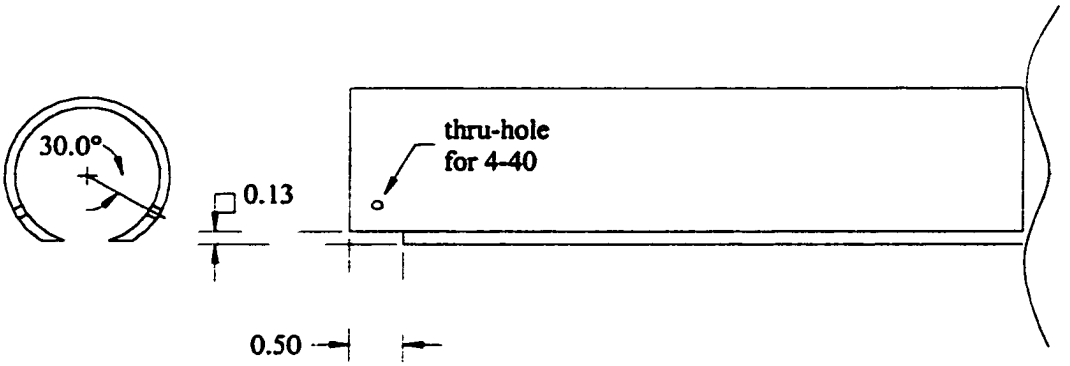

Figure 51. Design drawing for the sample holder end of the manipulator support tube.

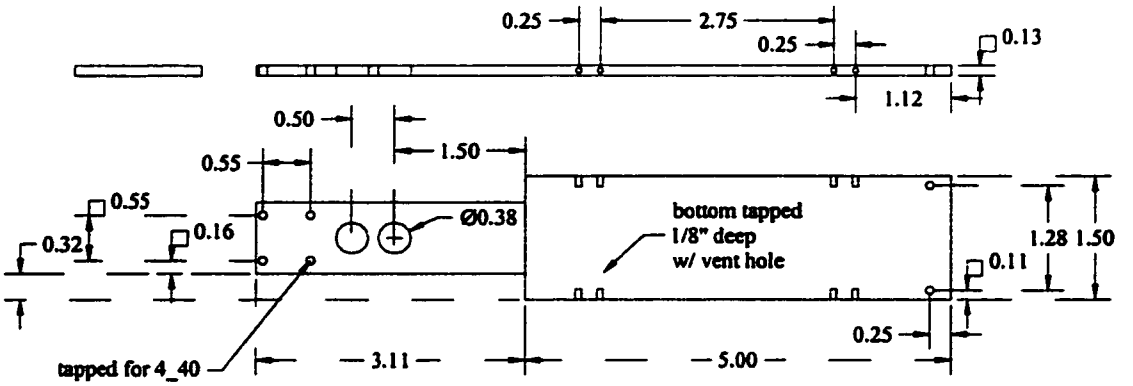

Figure 52. Design drawing for the sample holder titanium plate.

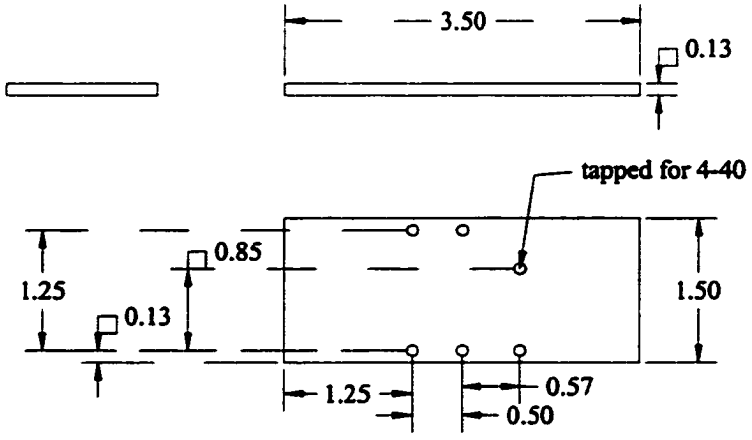

Figure 53. Design drawing for the sample holder/liquid nitrogen dewar mount sliding plate.

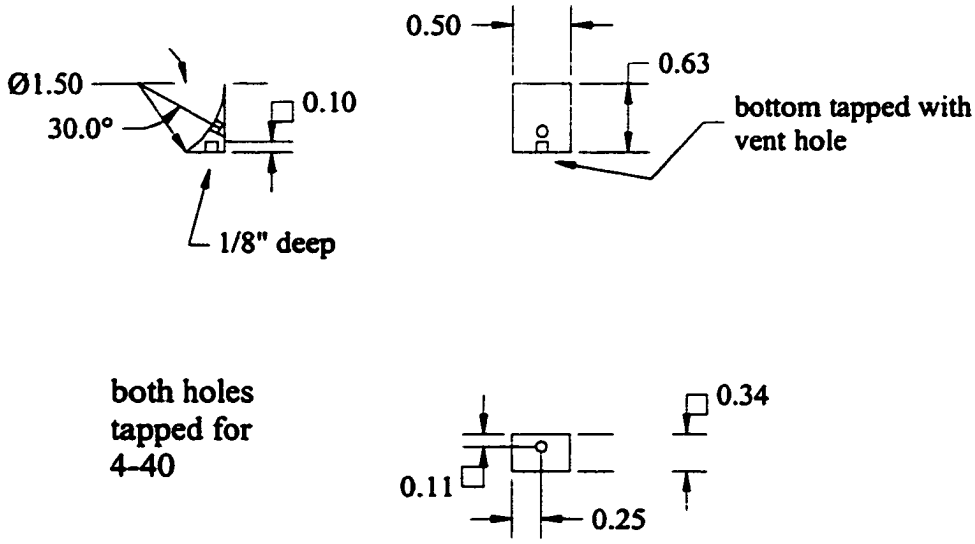

Figure 54. Design drawing for the support tube/Ti plate angle brackets.

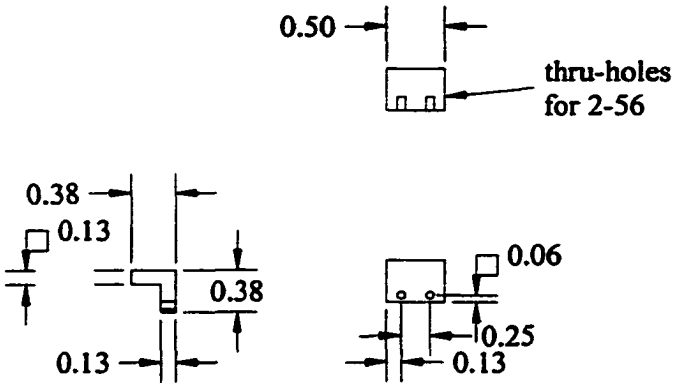

Figure 55. Design drawing for the sliding plate angle brackets.

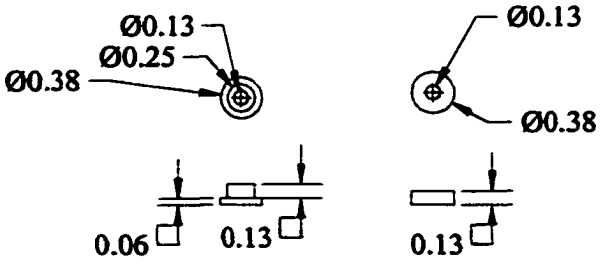

Figure 56. Design drawing for the Macor top hats and washers.

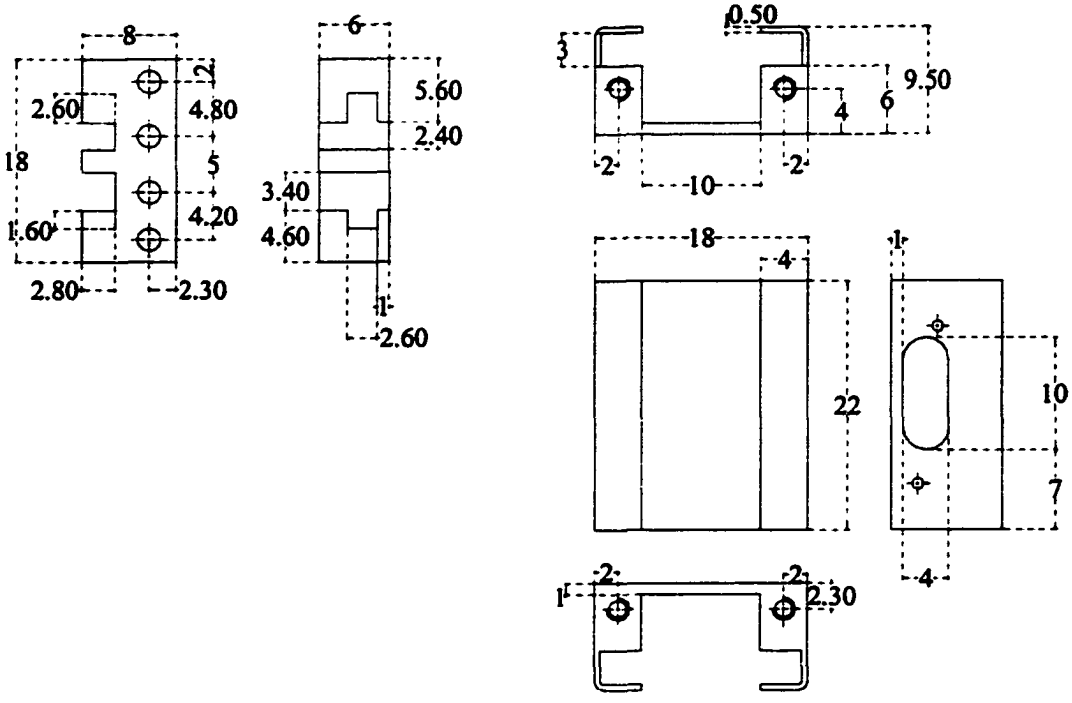

Figure 57. Design drawing for the OFHC copper sample holder. Dimensions are in millimeters.

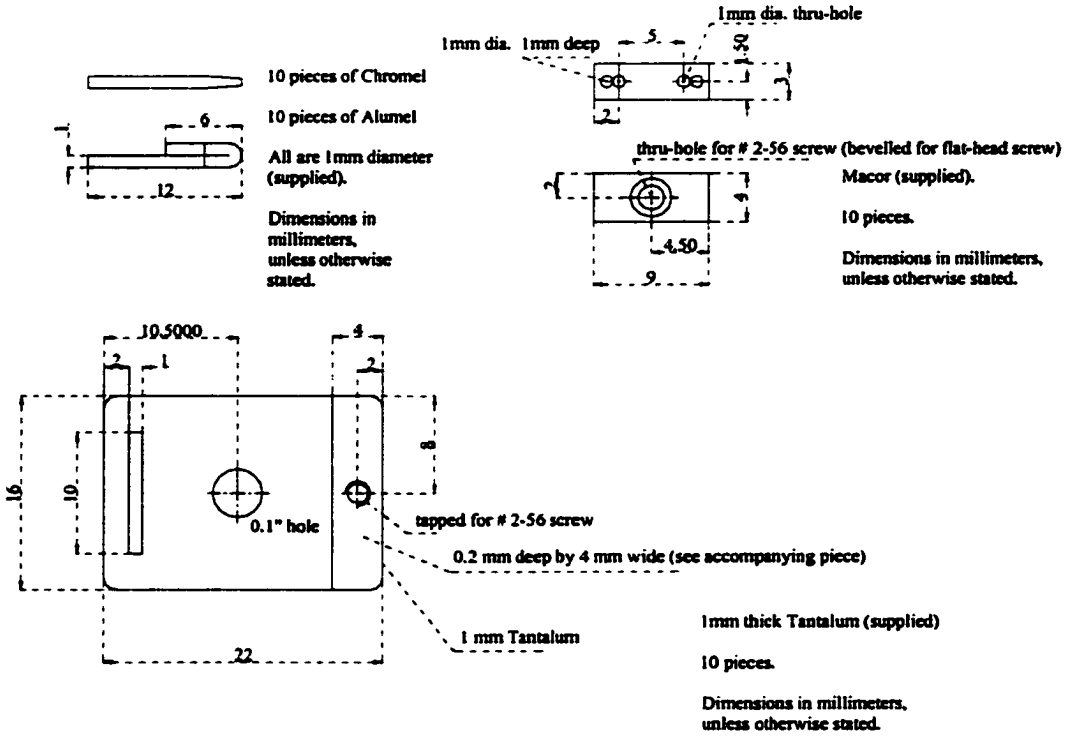

Figure 58. Design drawing for the tantalum sample platen and Macor thermocouple pin holder and pins. Dimensions are in millimeters.

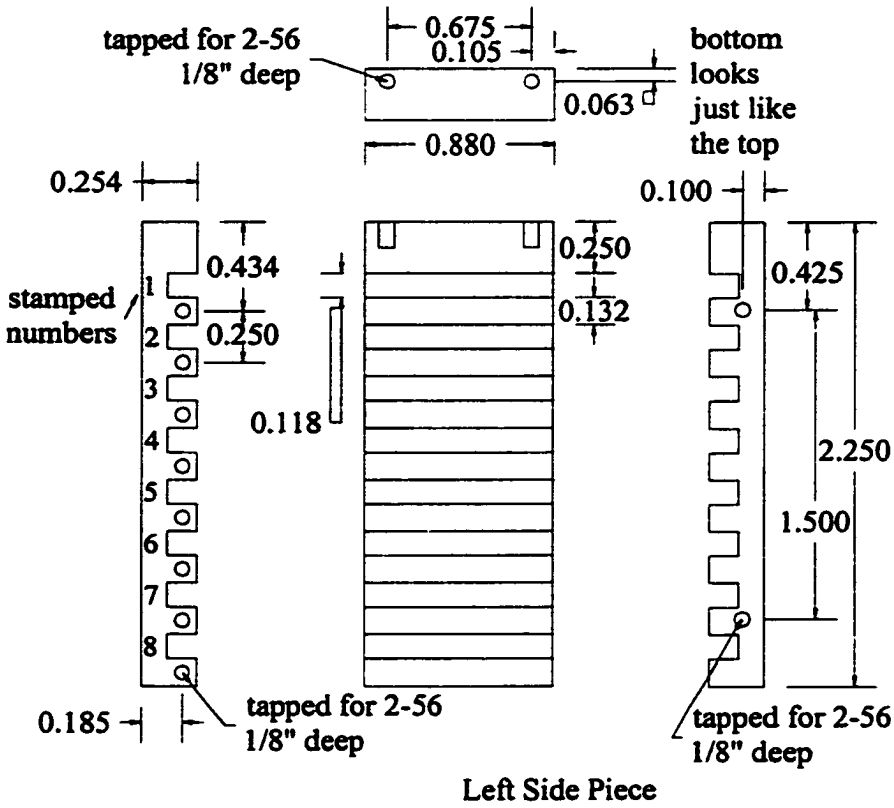

Figure 59. Design drawing for the side plates of the aluminum sample storage garage.

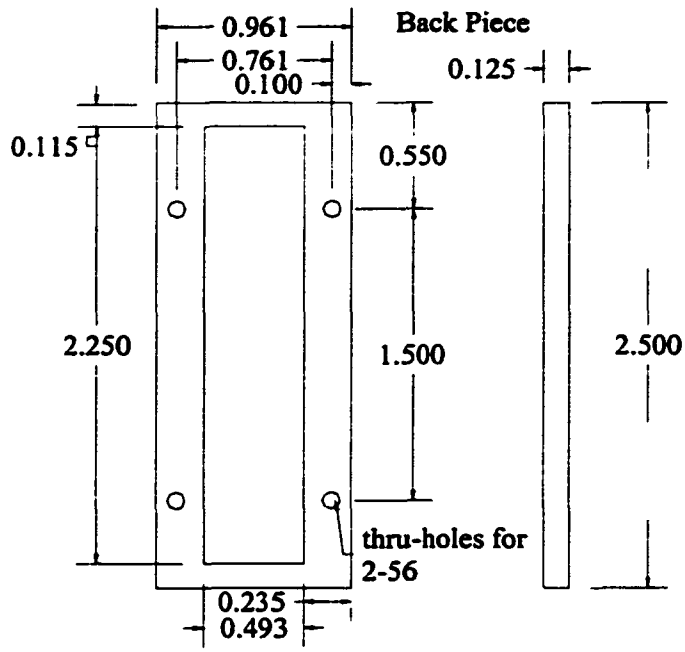

Figure 60. Design drawing for the back plate of the aluminum sample storage garage.

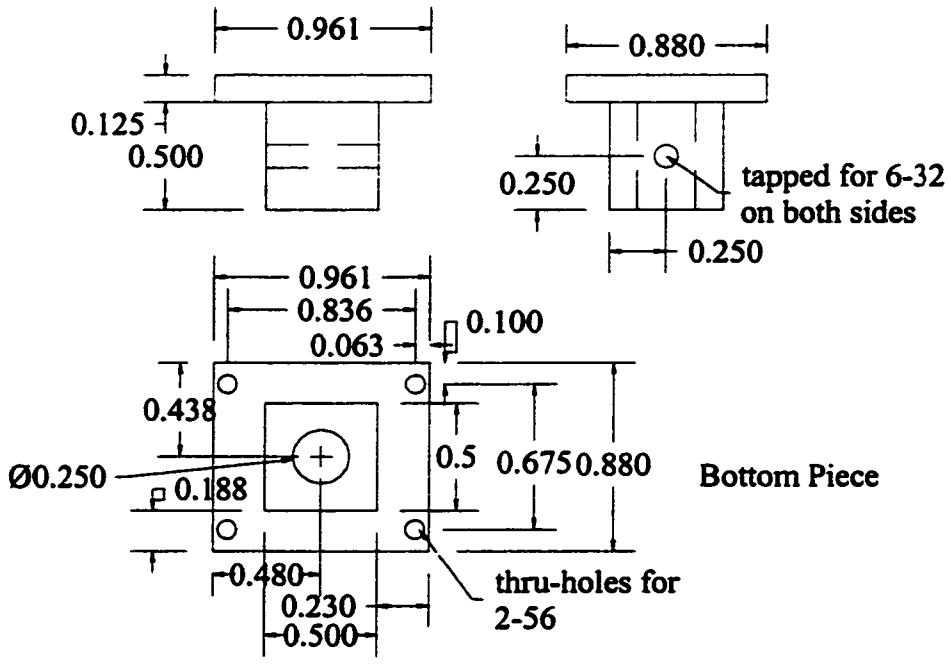

Figure 61. Design drawing for the bottom plate of the aluminum sample storage garage.

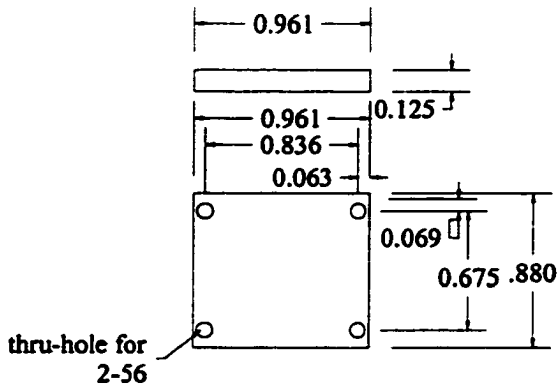

Figure 62. Design drawing for the top plate of the aluminum sample storage garage.

The retaining springs are essential to prohibit samples from leaving the garage when removing other samples. The top portion of this sample garage may be retrofitted to implement the use of a resistive-type sample heater, however this idea has not yet come to fruition.

Another custom design was a retrofitting of the pinscher mechanism by which sample manipulation outside of the sample holder was used. Originally, the pinscher set on the wobble stick was of the DME style available as a purchasing option on the Thermionics off-the-shelf wobble sticks. There were two reasons to modify this pinscher mechanism. One reason was that the pinschers were not wide enough to stably hold the sample platen. The other crucial reason was that the original Thermionics design was too thick in order to slide the sample platen entirely into the STM. For this reason the Thermionics design was completely unacceptable. The new retrofitted design incorporated two designs fit together, made from type 304 stainless steel (Fig. 63, 64). The coupling end, fitting into the cable/lever mechanism of the wobble stick was identical to the DME/Thermionics design, using two stationary spring clips, and a small cable-mounted axial rotation pin for the lever. Other than a needed Viton® O-ring spring to help to close the pinschers, this design works very well for the STM samples. Because CAMD owns two other unaltered wobble sticks for similar implementation, this retrofitting will be required again. For this reason, the design and description is included in this dissertation.

The last of the customized designs to be discussed in this appendix is that of the sample-translation holder for the sample load-lock system. This load-lock system is completely integrated into the vacuum system of the chamber, and truly enhances the capability to analyze many samples from various origins. In addition,

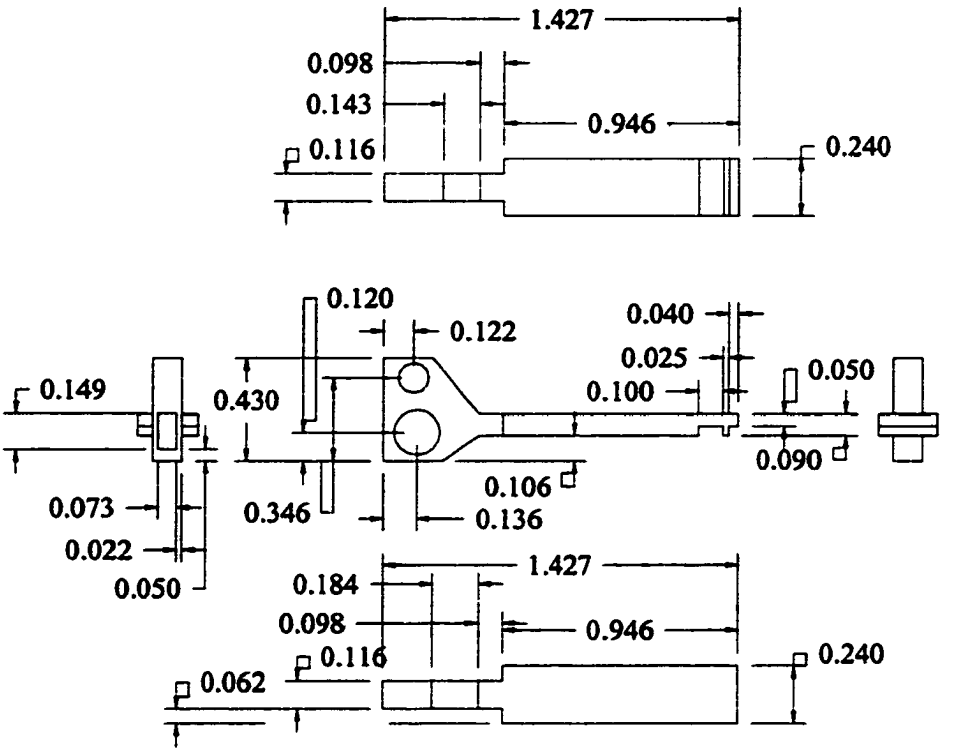

Figure 63. Design drawing for the top pinscher of the stainless steel wobble stick pinscher mechanism.

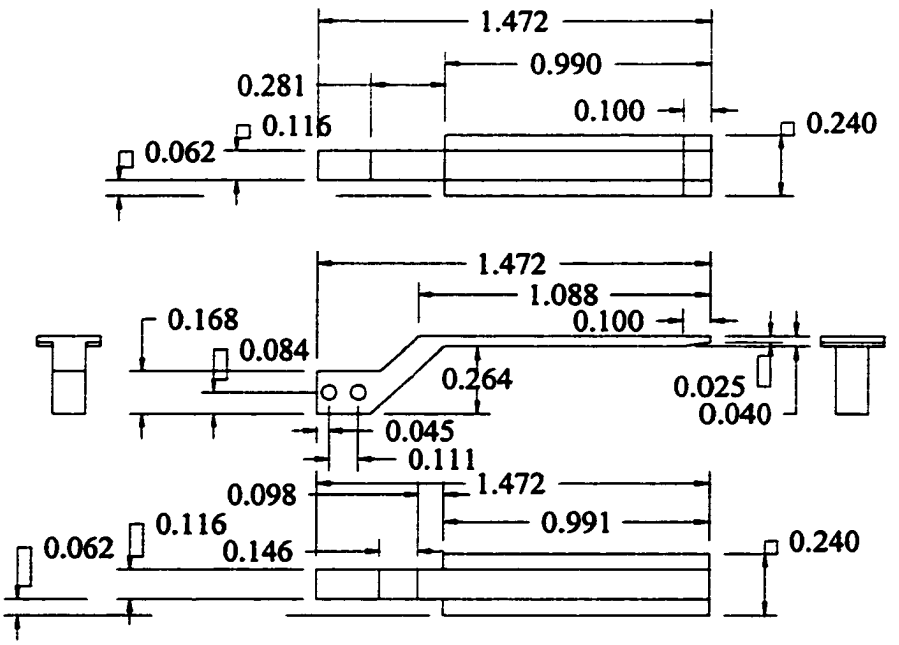

Figure 64. Design drawing for the lower pinscher of the stainless steel wobble stick pinscher mechanism.

when new substrates must be loaded into the chamber after each characterization (e.g. epitaxy on Si substrates), this load-lock mechanism is essential. The load-lock sample holder, shown in Fig. 65, is constructed of 6061 Al stock and is mounted onto the ¼-inch rod of a 14-inch stroke magnetically-coupled linear motion feedthrough. The chamber port onto which the feedthrough is mounted (Port # 21) is at a 45° angle with respect to the wobble stick, hence the angular design shown in Fig. 65. The angular aluminum block is fixed to the ¼-inch rod with a #4-40 set screw and the top is milled out to facilitate the Ta sample platens including a 3-mm thick sample. Two stainless steel retaining springs are mounted on the top to hold the platen in place and the dimensions are designed to fit through a standard 1.5-inch vacuum tube.

The AES system required a small degree of customization as well. Original procurement included the single-pass CMA, with built-in electron gun, the electron gun power supply module, and the preamplifier/voltage-to-frequency converter electronics module. The complete working system then required a computer-controlled sweeping voltage supply, two high voltage supplies for the front and rear end of the channeltron, frequency counter, a general purpose interface bus (GPIB), and software designed for user implementation, display and data storage. A schematic layout of the AES system is shown in Fig. 66. The sweeping voltage and channeltron high voltage power supplies used were SRS Model PS350 0-5000 V power supplies where the sweeping supply incorporated a 1:4 voltage divider shown with values in Fig. 67. The frequency counter used was an Ortec Timer/Counter with GPIB interface using a Keithley IEEE-488 controller card. The software was

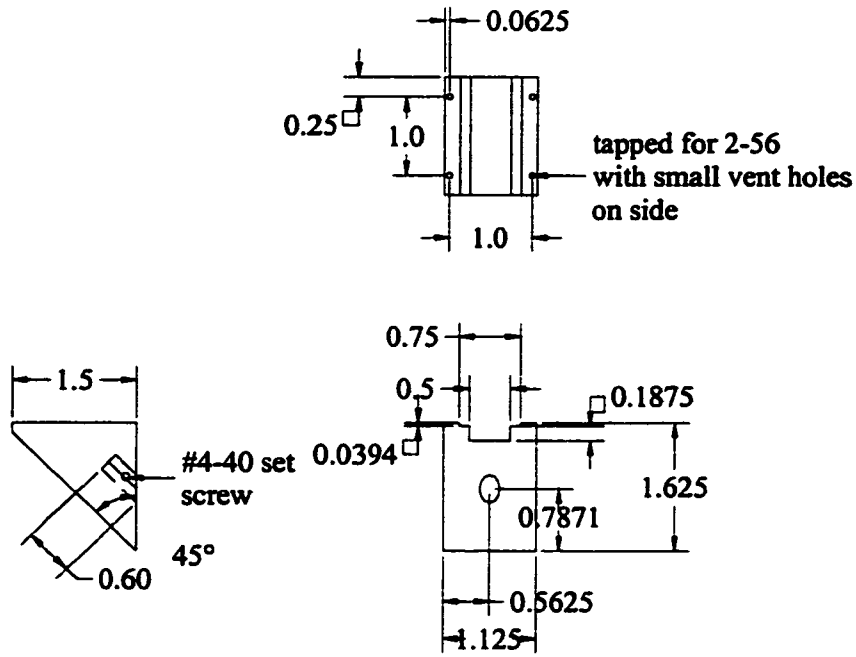

Figure 65. Design drawing for the aluminum load-load sample holder.

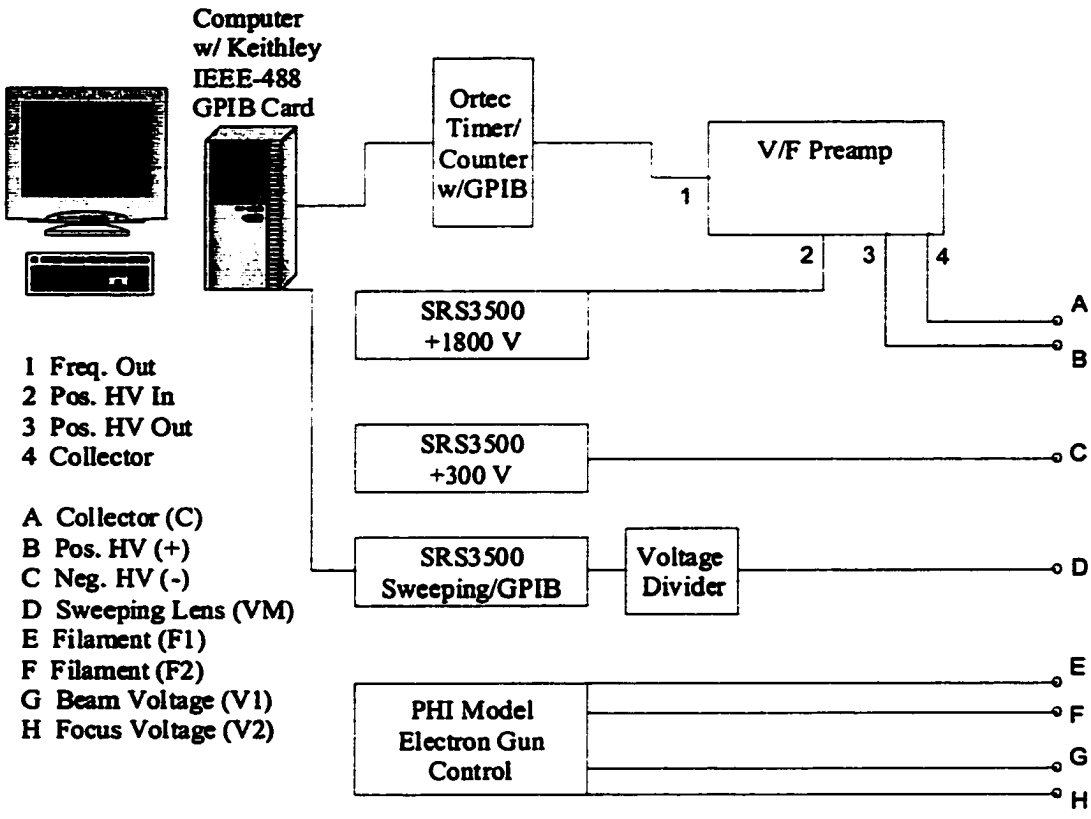

Figure 66. Schematic diagram of the electrical circuitry for the Auger Electron Spectroscopy unit.

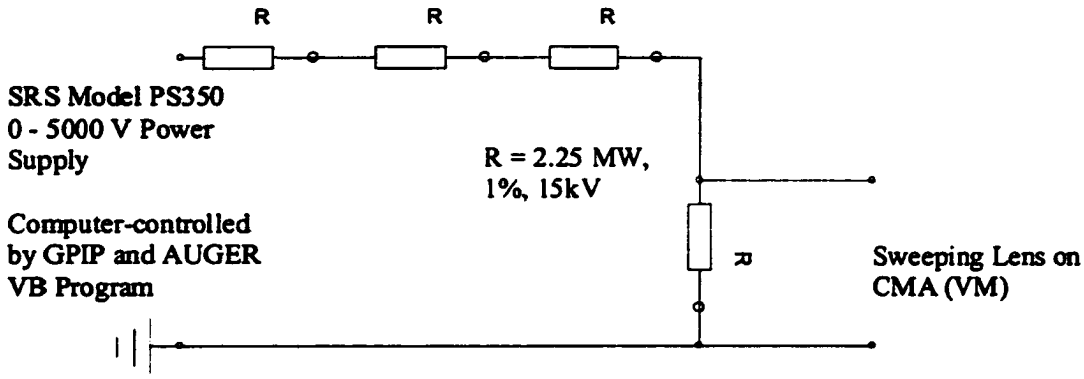

Figure 67. Schematic diagram of the 1:4 voltage divider used in the Auger Electron Spectroscopy unit.

written by Pavel Dotsenko and J. Mike Schoonmaker of CAMD called AUGER using the visual BASIC programming language.

Because the Preamplifier/V-F converter require +5 and +15 volts, usually supplied by the (unacquired) PHI AES power supply, it was also necessary to construct a simple power supply module using the voltage supplied by a NIM power transformer and two voltage regulators. The customized NIM module contains a DB-9 power receptacle (pin configuration shown in Table 6), where the following voltages may be obtained, +5, +15, ±6, ±12 and ±24 V. Since the NIM itself supplies ±6, ±12 and ±24 V, these voltages were made available for other applications. The final system works well for the desired application where a typical spectrum is shown in Fig. 68.

Numerous problems were encountered over the years of commissioning the Aarhus STM, the solutions to which will be enumerated here. The main and most difficult problem to troubleshoot was the sticking inchworm problem. This problem would typically manifest itself after baking the vacuum system, the symptoms of which was/is a computerized course approach of the tip never reaching the sample. Often the scanner tube was completely immobilized and other times it simply had a limited range. Numerous attempts to solve this problem mainly included additional lubrication of the tube with MoS_2, however this never seemed to help. It was hypothesized that moisture driven out in the bakeout process tended to reduce the lubrication effect, however this is contrary to the well-established properties of MoS_2 that reduced moisture enhances the lubrication properties. All assurances were made that the correct voltages were being applied, and in attempts to re-polarize the piezo

Table 6. Pin out for DB9 connector on NIM voltage supply module.

DB9 Pin #	Voltage (V)
1	+ 24
2	-24
3	+12
4	-12
5	+6
6	-6
7	+15
8	+5
9	Ground

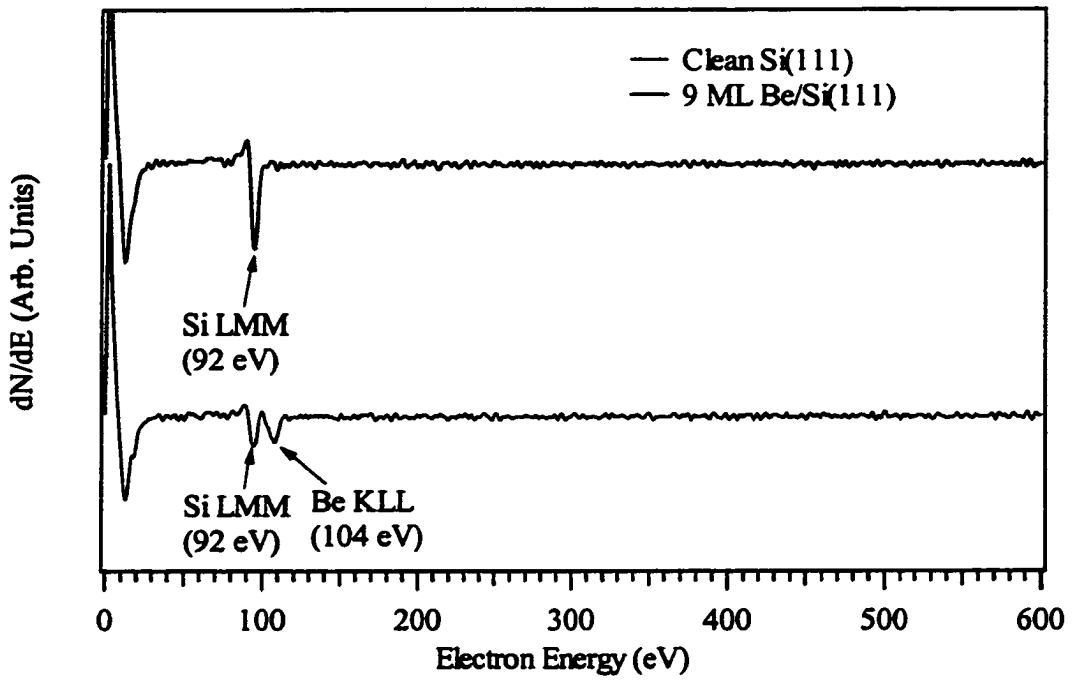

Figure 68. Typical Auger Electron Spectroscopy spectrum for clean Si(111) and Be/Si(111).

electrodes it was determined that a short existed on the bottom electrode of the inchworm. It was believed that this short pulled too much current from the ± 200 V power supply and therefore the power supply did not have enough power to run the inchworm properly. An inline diagnostic multi-plug was made to measure the voltages with the apparent load, however it was determined that this short was of no consequence to the power supply. Because re-polarization of the piezo electrodes may be necessary in the future, a brief description of this process is outlined here.

A 1000 VDC power supply is connected in a circuit with the electrode to be re-polarized as shown schematically in Fig. 69. A battery operated high impedance voltage meter is used to monitor the voltages. The positive lead from the supply goes to the input of the meter. The other wire from the meter goes to the electrode to be polarized and the negative lead from the supply goes to the reference electrode. As the voltage applied to the electrode is slowly increased to 1000 V, the voltage measured across the meter will rise up slightly, then drop as a result of charging and subsequent stabilization of the voltage. The piezoelectric is allowed to re-polarize at 1000 V for 10 – 15 minutes and then the process is complete. It is important to measure the capacitance of the piezo before and after the process. If the tube polarizes, the capacitances will increase. Typical capacitances are given in Table 7.

At one point in time, unable to satisfactorily solve the problem of the sticking inchworm, a longer tip was fabricated due to the limited range of the inchworm. Therefore the process of tip etching is thus described. Tungsten wires of 99.9+% purity and 0.38 mm diameter, purchased from Goodfellow Cooperation were first vacuum-annealed to ~ 850 °C. This process causes polycrystalline microstructure and sharp domain boundaries, which aid in prohibiting uneven etching and

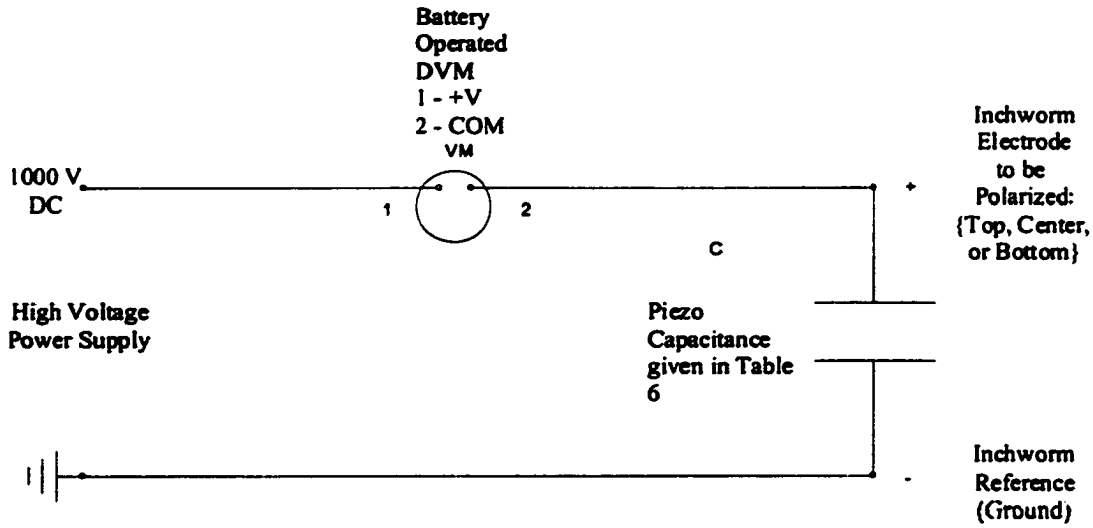

Figure 69. Schematic diagram of the circuit used in re-polarizing the piezo electrodes on the STM inchworm. The piezo capacitance should be measured before and after re-polarization.

Table 7. Typical values for the capacitance of the various piezoelectric transducers in the Aarhus STM.

Piezo Electrode	Capacitance (pF)
X +	280
X -	280
Y +	280
Y -	280
Top	560
Center	1100
Bottom	560

undesirable splintering at the tip end. Short (~ 4 mm) wires were then spot-welded to a thin stainless steel plate (2 × 2 mm^2 × 0.2 mm thick), the whole of which eventually entered the vacuum chamber. This was then mounted onto one of the electrodes of the tip etching unit, depicted in Fig. 70. The other electrode had a platinum hoop which encircled the W wire while submerged ~ 1 mm in a solution of ~ 2 – 4 Normal NaOH. With a voltage of ~ 10 V applied, the tip began to be electrochemically etched with an initial current of approximately 12 mA. Once the wire is etched to below a given diameter, the weight of the excess wire submerged in the solution causes the wire to break forming a sharp tip. As this occurs, the voltage is immediately turned off in order to arrest any additional etching by vapors, which tend to make the tip blunt. Typically once tips are made they are rinsed in de-ionized water and characterized using the JEOL JSM-T300 Scanning Electron Microscope (SEM). Tips are usually deemed to be good if the apex of the tip cannot be resolved by the SEM.

Although making a longer tip was a temporary fix to the problem of the sticking inchworm, eventually the inchworm would have a range even smaller than that required with an extremely long tip. In the end, it was determined that the sticking inchworm was a result of friction caused by uneven expansion and contraction of the scanner tube upon heating and cooling from bakeout. Although this problem will undoubtedly occur many times in the future, the most reproducible way to unstick the inchworm is by cooling, using the liquid nitrogen feedthrough of the cradle, and then upon subsequent warming, cycling the inchworm with increasing range. This cooling causes the tube to contract enough to become unstuck and then as the inchworm is warmed to room temperature, the range increases until finally it

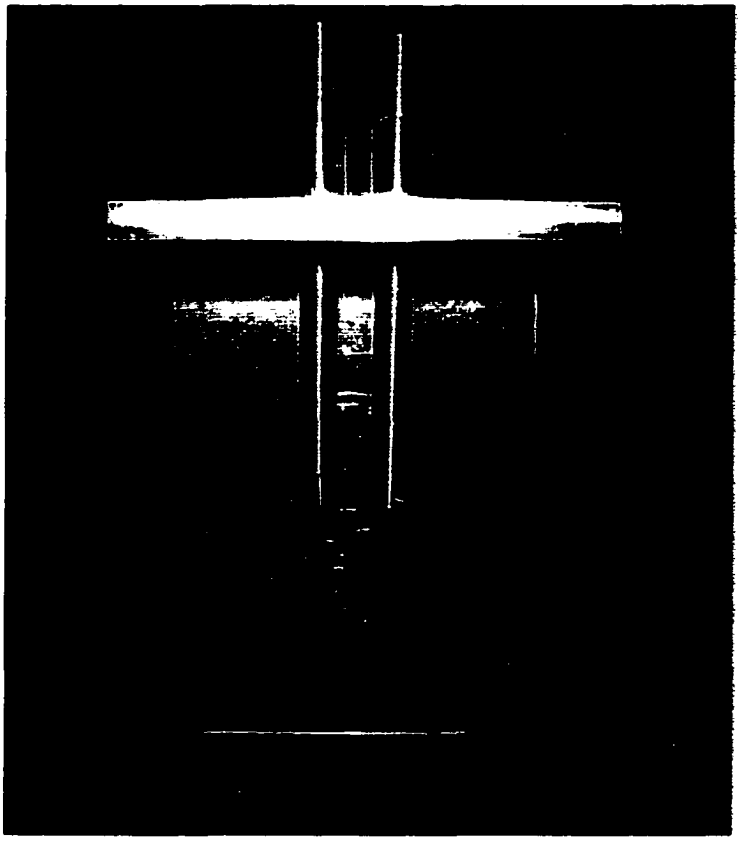

Figure 70. Photograph of the tungsten tip etcher made by O. Kizilkaya. The two vertical bars are the electrodes, one which holds the W tip wire and the other holds the Pt hoop.

has its full range. Other problems encountered in getting the STM working did not require such creative solutions. One problem was too much internal noise in the preamplifier, which was simply replaced with a new one. Another problem involved faulty wiring of the Amphenol connectors to the STM electrical feedthroughs. These connectors were completely and carefully re-made. The last recurring problem is the leaking cradle lock/liquid nitrogen feedthrough. This problem can be helped by pumping on the atmosphere side, but will not be corrected until replaced. Although numerous problems were encountered with this STM, it did not stop the collection of thousands of images some of which are shown in this dissertation.

Vita

Dustin Alexander Hite was born in Lafayette, Louisiana, on September 24, 1969. After moving to Baton Rouge in 1971, he attended the Louisiana State University Laboratory School, and subsequently graduated high school from University High School in 1987. Dustin attended Louisiana State University from 1988 to 1993, at which time he earned a bachelor of science degree in physics. Employed as an Environmental Radiation Specialist II at the Louisiana Department of Environmental Quality, Dustin worked in the Emergency Planning and Response section of the Radiation Protection Division from 1994 to 1995, planning for and participating in radiological emergency exercises involving the three nuclear power plants affecting the state of Louisiana. In 1995 Dustin began working as a Research Associate III at the J. Bennett Johnston, Sr., Center for Advanced Microstructures and Devices. In this position, he began to learn the tools of experimental surface science. In 1997 Dustin was offered and accepted a Board of Regents Graduate Fellowship to pursue a doctorate degree in the Department of Physics and Astronomy. During his graduate studies at Louisiana State University, he earned the degree of Master of Science in 2000. Dustin is married to Anabel Bowen Hite, and they have a beautiful daughter whose name is Juniper Ann Hite.

DOCTORAL EXAMINATION AND DISSERTATION REPORT

Candidate: Dustin Hite

Major Field: Physics

Title of Dissertation: Atomic and Electronic Structure of Ultra-Thin Metal Epitaxy on Metal and Semiconductor Surfaces

Approved:

Major Professor and Chairman

Dean of the Graduate School

EXAMINING COMMITTEE:

Date of Examination:

June 20, 2001